STUDIES ON ELECTRON-POSITRON PAIR PRODUCTION VIA SCHWINGER MECHANISM BY ULTRA-SHORT AND ULTRA-INTENSE LASER PULSES

By

CHITRADIP BANERJEE

PHYS03201204012

Raja Ramanna Centre for Advanced Technology, Indore

A thesis submitted to the

Board of Studies in Physical Sciences

In partial fulfilment of requirements

for the Degree of

DOCTOR OF PHILOSOPHY

of

HOMI BHABHA NATIONAL INSTITUTE

August, 2018

Homi Bhabha National Institute[1]

Recommendations of the Viva Voce Committee

As members of the Viva Voce Committee, we certify that we have read the dissertation prepared by Chitradip Banerjee entitled "Studies on electron-positron pair production via Schwinger mechanism by ultra-short and ultra-intense laser pulses" and recommend that it may be accepted as fulfilling the thesis requirement for the award of Degree of Doctor of Philosophy.

Chairman – Dr. Arup Banerjee	Arup Banerjee	**Date:**	16.1.19
Guide / Convener – Dr. Manoranjan P. Singh	M.	**Date:**	16.1.19
External Member Dr. S. Krishnagopal	K.	**Date:**	16.1.19
Examiner – Prof. V. K. Tripathi	V.K. Tripathi	**Date:**	16.1.19
Member 1- Dr. Aparna Chakrabarti	Aparna Chakrabarti	**Date:**	16.1.19
Member 2- Dr. Haranath Ghosh	Haranath Ghosh	**Date:**	16.1.19
Member 3- Dr. Vinit Kumar	Vinit Kumar	**Date:**	16/1/2019
Member 4- Prof. S. Bulusu	B.S.S.	**Date:**	16.1.19

Final approval and acceptance of this thesis is contingent upon the candidate's submission of the final copies of the thesis to HBNI.

I/We hereby certify that I/we have read this thesis prepared under my/our direction and recommend that it may be accepted as fulfilling the thesis requirement.

Date: 16/01/2019

Place: RRCAT, Indore

Guide: Dr. Manoranjan P. Singh

[1] This page is to be included only for final submission after successful completion of viva voce.

STATEMENT BY AUTHOR

This dissertation has been submitted in partial fulfilment of requirements for an advanced degree at Homi Bhabha National Institute (HBNI) and is deposited in the Library to be made available to borrowers under rules of the HBNI.

Brief quotations from this dissertation are allowable without special permission, provided that accurate acknowledgement of source is made. Requests for permission for extended quotation from or reproduction of this manuscript in whole or in part may be granted by the Competent Authority of HBNI when in his or her judgement the proposed use of the material is in the interests of scholarship. In all other instances, however, permission must be obtained from the author.

Chitradip Banerjee

Chitradip Banerjee

DECLARATION

I, hereby declare that the investigation presented in the thesis has been carried out by me. The work is original and has not been submitted earlier as a whole or in part for a degree/diploma at this or any other Institution/University.

Chitradip Banerjee

Chitradip Banerjee

List of Publications Arising from the Thesis

Journal

1. “Effect of polarization on the structure of electromagnetic field and spatiotemporal distribution of electron-positron pairs generated by colliding laser pulses” **Chitradip Banerjee** and Manoranjan P. Singh, J. Exp. Theor. Phys. Vol. 125, No. 1, pp. 12-21 (2017).

2. “Electron–positron pair creation by counterpropagating laser pulses: Role of carrier envelope phase,” **Chitradip Banerjee** and Manoranjan P. Singh, Eur.Phys. J. D **72**, 4 (2018).

3. “Phase control of Schwinger pair prodüction by colliding laser pulses” **Chitradip Banerjee** and Manoranjan P. Singh and Alexander M. Fedotov, Phys. Rev. A **98**, 032121 (2018).

4. “Imprint of temporal envelope of ultrashort laser pulses on momentum spectrum of $e^{+}e^{-}$ pairs” **Chitradip Banerjee** and Manoranjan P. Singh, arXiv:1807.06951v1 (*under review in Phys. Rev. D*)

5. “Transient and pre-transient stages in field induced phase transition of vacuum state” **Chitradip Banerjee** and Manoranjan P. Singh,arXiv:1809.06901v1 (*under review in Phys. Rev. D*)

6. “Entropy growth in pair production by Sauter field ”**Chitradip Banerjee** and Manoranjan P. Singh (*In preparation*)

Conferences

1. “The structure of electromagnetic field of circularly polarized counterpropagating intense laser pulses” **Chitradip Banerjee** and Manoranjan P. Singh, 23th DAE BRNS National

Laser Symposium, December 3-6, **2014**, Tirupati, India.

2. "On pair production with focused ultrafast intense laser pulse: Role of polarization" **Chitradip Banerjee** and Manoranjan P. Singh, 29^{th} National Symposium on Plasma Science and Technology and International Conference on Plasma Science and Technology (PLASMA 2014), December 8-11, **2014**, Mahatma Gandhi University, Kottayam, Kerala, India.

3. "Pair production by intense counterpropagating laser beams:circular polarization versus linear polarization" **Chitradip Banerjee** and Manoranjan P. Singh, 5^{th} PSSI-Plasma Scholar Colloquium (PSC-2016), August 27-28, **2016**, Cuttack, India.

4. "Role of Carrier envelope phase on the temporal distribution of electron-positron pairs produced by linearly polarized counterpropagating laser pulses" **Chitradip Banerjee** and Manoranjan P. Singh, 25^{th} DAE-BRNS National Laser Symposium , December 20-23, **2016**, Bhubaneswar, India.

5. "Pair Production By Linearly Polarized Counterpropagating Laser Pulses: e-Waves versus h-Waves" **Chitradip Banerjee** and Manoranjan P. Singh, 31^{st} National Symposium on Plasma Science and Technology and International Conference on Plasma Science and Technology (PLASMA 2016), **2016**, Coimbatore, India.

5. "Field induced phase transition of vacuum oscillation and creation of electron positron plasma state in time dependent multi-sheeted Sauter pulse: Effect of higher order frequency chirping" **Chitradip Banerjee** and Manoranjan P. Singh, Probing strong-field QED in electron-photon interactions, 21-23 August, 2018, DESY, Hamburg, Germany.

Chitradip Banerjee

Chitradip Banerjee

DEDICATION

This thesis is dedicated to my family

ACKNOWLEDGEMENTS

The completion of the present thesis could not have been possible without the constant support and guidance of many people. First of all, I would like to thank my supervisor Prof. Manoranjan P. Singh for his valuable guidance, support and encouragement throughout the tenure of my Ph.D. His clear, elegant and simple approach of illustrating scientific ideas has helped me to understand several aspects of theoretical physics. Apart from that, I have also learnt from him about presenting scientific work in an elegant way. I acknowledge him humbly for all his support.

I would like to express my sincere gratitude to Prof. Dr. P. A. Naik, Director RRCAT for his constant attention, guidance and encouragement during the progress of my work. I thank him especially for many useful comments and constructive suggestions which helped me to complete the thesis.

I extend my gratitude to Prof. Arup Banerjee, dean academic of HBNI and the chairman of the doctoral committee for his all time support, encouragement, and critical reviews of my work. I also thank him for his support as an head of the division, HRDS. I am thankful to all the members of my doctoral committee for evaluating the progress of my research work during my Ph. D. tenure. I thank Dr. Aparna Chakrabarti, Dr. S. Krishnagopal, Dr. Haranath Ghosh and Dr. Vinit Kumar for their support.

I am grateful to the anonymous referees of my journal publications for their suggestions and comments which helped me to improve the quality of the work presented in this thesis. I sincerely acknowledge the generous help received from Prof. Alexander M. Fedotov in several times for critically reviewing my work and make collaboration with me. I thank Dr. G. Sarri and Dr. L. Labun for critically reviewing my work and their fruitful suggestions.

I would like to thank my batchmates Sudheer, Arijit Chakraborty, Debashish Mondal, Aditya N. Pandey for their never ending help. Arijit Chakraborty, Dr. Pratik Varshney, and Deepraj Phadte are acknowledged for their help in making MATLAB and MATHEMATICA programming which was essential for my work in this thesis. I am thankful to my seniors Dr. Shyam Sundar, Dr. Yasvir Kalkal, Dr. Smritijit Sen for their indispensable support in my Ph. D. days. I am also thankful to my juniors Rijul, Nitish, Rajeev, Partha, Ramjan, Soumyadeep and all for their help and support. I thank to Dr. Himanshu Singhal and Mr. Mukund Kumar for the several discussions on ultrashort laser pulse propagation and the effect of carrier envelope phase on the temporal profile.

Finally, I express a deep sense of gratitude to my family for their love, support and encouragement.

Contents

Synopsis

The e^+e^- pair production from vacuum by strong electromagnetic (EM) field is a fundamental prediction of quantum electrodynamics (QED) [1]. Although the process was foreseen theoretically several decades ago [2–6], its experimental verification is still missing because of the unavailability of an electric field strength comparable to the Schwinger limit $E_S = 1.32\times10^{18}$ V/m. Since the probability of pair production from vacuum by a strong electric field of strength E_{peak} is proportional to $\exp(-\pi E_S/E_{peak})$, the process is exponentially suppressed for $E_{peak} \ll E_S$. The available electric field strength for the present-day laser systems is of the order of $E_{peak} \sim 10^{13} - 10^{14}$ V/m [7], considerably below the critical field limit E_S. However, recent advances in laser technology, specially the use of chirp pulse amplification method, have made it possible to generate ultrashort laser pulses in deeply relativistic regime [8]. The European Extreme Light Infrastructure for Nuclear Physics (ELI-NP) is planing to build a 10 PW pulsed laser to achieve intensities $I \sim 10^{23}$ W/cm^2 for the first time for investigating new physical phenomena at the interfaces of plasma, nuclear and particle physics [9, 10]. The electric field at the laser focus will have a maximum value of 10^{15} V/m at such intensities. In the ELI-NP experimental area E6, it is proposed to study radiation reactions, strong field QED effects and the resulting production of ultrabright gamma rays which could be used for nuclear activation. The construction of X-ray free electron laser (XFEL) is under way at DESY, Hamburg using self amplified spontaneous emission (SASE) principle [11]. In a landmark experiment E144 at Stanford Linac Acceleration centre (SLAC) in 1997 it was possible to observe non-linear QED processes like non-linear Compton scattering and stimulated pair production in the collision of a 46.6 GeV electron beam with terawatt laser pulses of 1053 nm and 527 nm with intensity $I = 10^{22}$ W/cm^2 [12, 13]. Although these multi-photon processes pertain to the perturbative regime of QED, the successful experimental realizations thereof raise the hope for the experimental verification of the Schwinger mechanism in coming decades.

The aforesaid developments renewed interest in theoretical studies of pair production by intense optical lasers. Using the realistic focused field models, e.g. a weakly focused field in paraxial approximation [14], tightly focused field models [15, 16], and the optimally focused field model of e-dipole pulses [17], it was demonstrated that pair production can take place even at intensities substantially lower than the critical intensity $I_S = \frac{c}{4\pi}E_S^2$ (here c denotes the light velocity in vacuum). Superposition of laser pulses in a counterpropagating configuration has been shown to lower the threshold value of the required field strength considerably [18]. Such beam configurations were extensively used to study various aspects of pair production, including the dynamics of post production.

Studying pair production for a realistic space and time dependent field of the ultra short and intense laser pulses offers new challenges. This has resulted in the development of numerous theoretical approaches. While the proper time propagator method was used by Schwinger to derive the pair production rate for an electric field constant in time and space [1], its extension to the space/time varying fields was done using the WKB method [19] and the worldline instanton method [20]. Recognising the equivalence of the pair production process to the over-the-barrier scattering problem in quantum mechanics, the structure of the turning points in the complex time plane [21] was used to calculate the longitudinal momentum spectrum of the created particle at the asymptotic time for a spatially uniform time dependent electric field. A full fledged dynamical description of pair creation process for time varying fields is possible within the framework of the quantum kinetic approach using the quasi-particle [22] representation (for spatially homogeneous fields) and the Wigner representation [23] (for spatially inhomogeneous fields).

The study of pair production has also provided yet another setting to test and substantiate the concept of t-non invariant vacuum state proposed in the area of quantum chromodynamics (QCD) for the pre-equilibrium evolution of quark-gluon plasma in heavy ion collision and the possible connection thereof to the phase transition [24]. The long standing issue of the origin of irreversibility and its effect on the entropy production have received attention in the recent times [25].

In this thesis, we have studied pair production from vacuum in the focal region of two ultrashort and ultraintense counterpropagating laser pulses using Narozhny-Fofanov (N-F) field model [14]. To begin with, we have taken the general focused EM field which is a combination of e- and h- polarised waves to study the dependence of the spatiotemporal distribution of created pairs on the relative content of e- and h- polarizations in the resultant field in the focal region. We have also studied the effect of carrier envelope phase (CEP) and the relative phase difference of two linearly/circularly e-polarised colliding pulses on the invariant electric and magnetic fields structures and hence the spatiotemporal distribution of the created pairs. We have observed the generation of ultrashort particle bunches with FWHM of 200 atto-second [26, 27]. Later, we have studied the dynamical aspects of created pairs using quantum kinetic theory. Here we study the effect of the temporal pulse envelope on the longitudinal momentum spectrum of the created particles. The pair production process may be viewed as a field induced phase transition (FIPT) of the vacuum state [25]. The evolution of the order parameter of the phase transition is studied for multi-sheeted Sauter pulse with higher order frequency chirp parameter. Pair production in strong EM field allows to analyse the inter-relation between the entropy production and irreversibility in systems which show reversibility at microscopic level [28]. In this thesis, the evolution of the von Neumann entropy function for a few cycle Sauter pulses is studied. The non-monotonic entropy growth has been observed with oscillatory structures. This thesis is organized in seven chapters a brief description of which is as follows.

We begin with a basic introduction of the particle production mechanism via Schwinger mechanism in the presence of ultrashort and ultraintense laser pulses in **Chapter 1**. We also present a review of different pair production mechanisms (multi-photon pair production process and tunneling pair production mechanism) [6, 29]. In order to have the gauge and Lorentz invariant description of pair production via Schwinger mechanism we introduce the concept of invariant electric and magnetic fields in a Lorentz transformed frame in which electric and magnetic fields are parallel to each other[1, 18, 30]. We discuss different configurations of the focused colliding laser pulses [26, 27]. The quantum kinetic formalism which allows us to study the longitudinal momentum spectrum of created pairs, evolution of the order parameter of FIPT and the non-monotonic increase of entropy is also discussed.

In **Chapter 2** we study pair creation for different state of beam polarization of the EM field of two counterpropagating laser pulses. The characteristic parameter for the beam polarization is given by the parameter of asymmetry μ [31] between e-and h-waves in the field expression where e (h)-wave refers to the EM field in which only electric (magnetic) field is purely transverse with respect to the propagation direction [14]. The main aim of revisiting this topic is to know how the pairs are distributed in spatiotemporal coordinates for different values of μ. It is found that the beams made up of entirely e-and h-waves ($\mu = \mp 1$) are the most effective for pair production whereas the beam having equal mixture of e-and h-waves ($\mu = 0$) is the worst for pair production [18]. In this chapter, we explain these observations by the structure of underlying fields. Though $\mu = 0$ case is not suitable for efficient pair production, it is found to be appropriate for generating shorter bunches of electrons and positrons [26].

Ultrashort laser pulses are characterized by CEP which is inherent to the process of their generation [32]. The effect of CEP on the spatiotemporal distribution of electron-positron pairs created by ultra-intense counterpropagating femtosecond laser pulses is studied in **Chapter 3**. When the laser pulses are linearly e-polarized, the temporal distribution of the pairs is found to be sensitive to CEP. Same analysis is extended for the circularly e-polarized laser pulses. It is seen that when the counterpropagating laser pulses are both right and left circularly polarized, the effect of CEP is insignificant. On the other hand when the superimposed fields are in the combination of right and left circular polarizations, the CEP dependence shows up in the invariant electric and magnetic fields structure and hence it reflects in the particle-antiparticle temporal distribution. However, the total number of pairs is not greatly influenced by CEP for both the polarizations [27].

In **Chapter 4** we have studied the pair production mechanism by a strong EM field of two colliding e-polarized laser pulses with a relative phase shift Ψ. The spatio-temporal distribution of created pairs is very sensitive to this phase shift and to polarization of the pulses. We have analysed this dependence in detail and demonstrate how it can be explained in terms of the underlying invariant electric field structure of the counterpropagating focused pulses which is spiky. We find that the total pair production is larger when one of the spikes is located near the centre of the spatiotemporal envelope (and the distribution of created pairs looks approximately unimodal), and smaller when the neighboring spikes are off-centered but located symmetrically. The particular phase shift required for each case depends on the polarization of the pulses. Among the considered cases, for the parameters adopted in this study the global maximum for the total number of pairs is achieved with the circularly e-polarized counterpropagating pulses having the same sense of rotation with no relative phase difference as considered in Ref. [18]. Possibility of phase control of Schwinger pair production may be useful, e.g., to increase the attainable intensity of tightly focused colliding laser pulses by reducing pair production and hence preventing field depletion at their crossing, or, conversely, to measure the typically unknown field structure and phase relations of extremely strong laser pulses [33].

Effect of temporal pulse shape of intense few cycle ultrashort laser pulses on the momentum distribution of e^+e^- pairs is studied using quantum kinetic equation in **Chapter 5**. Single and multi-sheeted Gaussian and Sauter pulses, are considered to this end. For multi-sheeted pulses having a few cycle of oscillations the temporal profile of the pulse is revealed in the interference pattern in the momentum spectrum at asymptotic times. The onset of the oscillation due to the quantum interference between the neighbouring turning point structures takes place for fewer subcycle oscillations for the Gaussian pulse than that for the Sauter pulse. Furthermore, the oscillation amplitude for the same number of subcycle oscillations within the pulse duration is larger for the Gaussian pulse. The presence of the carrier offset phase and the frequency chirping is found to magnify these differences. These observations are explained in terms of the turning point structure in complex t-plane and invoking the concept of over the barrier scattering. The momentum spectrum of the created particle-antiparticle pairs being very sensitive to the shape of temporal envelope may provide a way to measure it for the ultrashort laser pulses.

Pair production in the presence of a time dependent electric field may be viewed as a FIPT [24, 25]. In **Chapter 6**, we have studied the evolution of the order parameter associated with FIPT of the vacuum state for the time dependent multi-sheeted Sauter pulse. In particular, the effect of the time dependent frequency of the electric field due to the higher order frequency chirping is investigated. We limit our study up to the quadratic frequency chirping for the different evolution stages of the order parameter e.g., the quasi electron positron plasma stage, the transient stage and the residual electron-positron plasma stage. In the presence of the quadratic frequency chirping, the formation of pre-transient region is observed at earlier times before the electric field attains its maximum value. The t non-invariant particle distribution function results in the non-monotonic increase in von Neumann entropy [28, 34]. We study the effect of sub-cycle pulse oscillations on the evolution of the entropy and the particle density for different values of subcycle oscillations.

In **Chapter 7**, we summarize the major outcomes of our studies on electron-positron pair production via Schwinger mechanism by ultrastrong and ultrashort laser EM fields and discuss the future outlook.

References for synopsis

[1] J. Schwinger, Phys. Rev. 82 (1951) 664.

[2] F. Sauter, Z. Phys. 69 (1931) 742.

[3] W. Heisenberg and H. Euler, Z. Phys. 98 (1936) 714.

[4] D. Volkov, Z. Phys. 94 (1935) 250.

[5] A. Nikishov, Nucl. Phys. B 21 (1970) 346 .

[6] E. Brezin and C. Itzykson, Phys. Rev. D 2 (1970) 1191.

[7] G.A. Mourou, T. Tajima and S.V. Bulanov, Rev. Mod. Phys. 78 (2006) 309.

[8] T. Tajima and G. Mourou, Phys. Rev. ST Accel. Beams 5 (2002) 031301.

[9] T. Heinzl and A. Ilderton, Eur. Phys. J. D 55 (2009) 359.

[10] G.V. Dunne, Eur. Phys. J. D 55 (2009) 327.

[11] J. Andruszkow et al., Phys. Rev. Lett. 85 (2000) 3825.

[12] C. Bula et al., Phys. Rev. Lett. 76 (1996) 3116.

[13] D.L. Burke et al., Phys. Rev. Lett. 79 (1997) 1626.

[14] N. Narozhny and M. Fofanov, JETP 90 (2000) 753.

[15] A. Fedotov, Laser Phys. 19 (2009) 214.

[16] Y.I. Salamin, G.R. Mocken and C.H. Keitel, Phys. Rev. ST Accel. Beams 5 (2002) 101301.

[17] W. Su et al., Phys. Rev. A 86 (2012) 013422.

[18] S. Bulanov et al., JETP 102 (2006) 9.

[19] H. Kleinert, R. Ruffini and S.S. Xue, Phys. Rev. D 78 (2008) 025011.

[20] G.V. Dunne and C. Schubert, Phys. Rev. D 72 (2005) 105004.

[21] C.K. Dumlu, Phys. Rev. D 82 (2010) 045007.

[22] S. Schmidt et al., Phys. Rev. D 59 (1999) 094005.

[23] H.T. Elze and U. Heinz, Phys. Rep. 183 (1989) 81 .

[24] S.A. Smolyansky et al., P-Adic Numbers, Ultrametric Analysis, and Applications 4 (2012) 319.

[25] S.A. Smolyansky et al., Russ. Phys. J. 59 (2017) 1731.

[26] C. Banerjee and M.P. Singh, JETP 125 (2017) 1.

[27] C. Banerjee and M.P. Singh, Eur. Phys. J. D 72 (2018) 4.

[28] Y. Kluger, E. Mottola and J.M. Eisenberg, Phys. Rev. D 58 (1998) 125015.

[29] A. Di Piazza et al., Rev. Mod. Phys. 84 (2012) 1177.

[30] A. Nikishov, Sov. Phys. JETP 30 (1970) 660.

[31] N. Narozhny, Laser Phys. 15 (2005) 1458.

[32] F. Mackenroth, A. Di Piazza and C.H. Keitel, Phys. Rev. Lett. 105 (2010) 063903.

[33] C. Banerjee, M.P. Singh and A.M. Fedotov, (2018), arXiv:1806.07088.

[34] J. Rau, Phys. Rev. D 50 (1994) 6911.

List of Figures

List of Tables

Chapter 1

Introduction

The e^+e^- pair production from vacuum by strong electromagnetic (EM) field is a fundamental prediction of quantum electrodynamics (QED) [1]. The basic process is coined from the relativistic wave equation where energy has positive and negative continua which are separated by the forbidden energy gap $2mc^2$. According to the Dirac theory [2], the vacuum state is defined as the states with negative energy are totally filled and positive energy states are empty. But due to the quantum fluctuation in the vacuum state there exist virtual particle-antiparticle pairs (here electron and positron) which does not satisfy the Einstein energy-momentum on-shell mass condition (a particle with rest mass m, momentum $\mathbf{p}$ and energy E should satisfy $E^2 - p^2c^2 = m^2c^4$ where c is speed of light in vacuum). So there is a spontaneous creation and annihilation of virtual particle-antiparticle pairs from the vacuum. The process is limited by the fundamental quantum mechanical uncertainty which basically sets the characteristic length and time scale of the process. In general, one can think the vacuum as a statistical ensemble of virtual electron-positron loops which are randomly oriented as shown in left side of Fig. 1.1. In the presence of an external field, these loops are oriented along the electric field and we get polarized vacuum as shown in right side of Fig. 1.1. If the external electric field is so strong that it would overcome the mutual Coulombic attraction force for the charged particle-antiparticle pairs we get real particle and anti-particles from the vacuum. The typical dimension of the loop is Compton length $\lambda_C = \hbar/mc$.

One can generally estimate the production rate of the created pairs which get tunnel out from the potential barrier by a constant electric field using the WKB method. We consider the constant electric field with field strength E_0, particle energy E and 3-momentum $\mathbf{p}(x)$. The

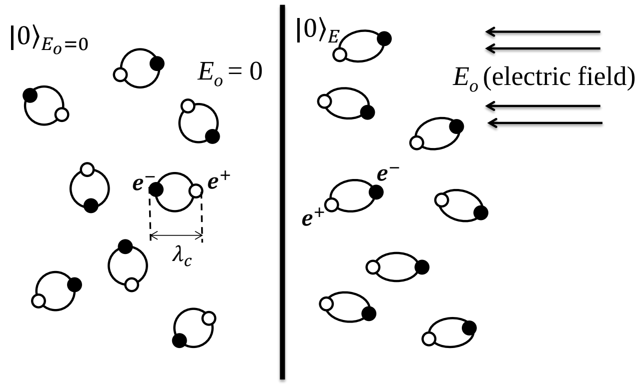

FIGURE 1.1: Pictorial representation of vacuum state without and with the external field. (Adapted from "Strong-Field QED Processes in Short Laser Pulses", Daniel Seipt, Ph. D. thesis, University of Dresden, 2012)

potential barrier gets modified and it varies linearly. We have the modified on-shell mass condition

$$(E - |e|E_0 x)^2 = c^2(m^2c^2 + \mathbf{p}(x)^2), \tag{1.1}$$

where $e(|e| < 0)$ is the charge of the particle. The classically forbidden regions are determined where the particle momentum becomes imaginary and we have non-zero quantum mechanical tunneling probability in this forbidden region. The classical turning points are determined by equating $p(x) = 0$ which will end up two turning points located at $x^+ = (E + mc^2)/|e|E_0$ and $x^- = (E - mc^2)/|e|E_0$. So apart from the pre-factor which is of the order of unity, the tunnelling probability is calculated by

$$W \sim \exp\{-\frac{2}{\hbar} i \int_{x^+}^{x^-} dx p(x)\} \tag{1.2}$$

where $p(x) = imc\sqrt{1 - (E - |e|E_0 x)^2/m^2c^4}$ in the classically forbidden region. Now changing the variable $\lambda = (E - |e|E_0 x)/mc^2$ and $d\lambda = -|e|E_0 dx/mc^2$. The limits of the integration become $\lambda^+ = -1$ and $\lambda^- = 1$. So we get

$$W \sim \exp\{-\frac{4m^2c^3}{\hbar|e|E_0} \int_0^1 d\lambda \sqrt{1 - \lambda^2}\} = \exp\{-\frac{\pi m^2 c^3}{\hbar|e|E_0}\}. \tag{1.3}$$

Here one define the critical field strength E_{cr} which accelerates the virtual electron positron pair

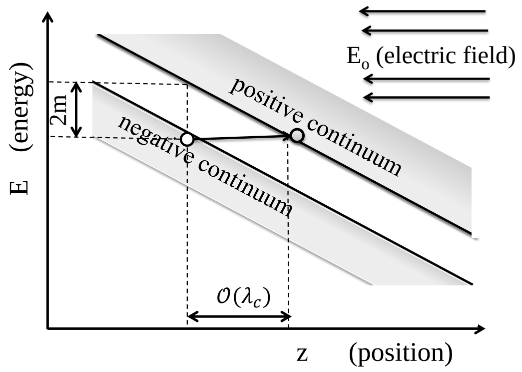

FIGURE 1.2: Plot of the potential barrier in the presence of the external electric field. (Adapted from "Strong-Field QED Processes in Short Laser Pulses", Daniel Seipt, Ph. D. thesis, University of Dresden, 2012)

upto a $\lambda_C = \hbar/mc$ to gain the kinetic energy of the order of the rest mass of the pair and we get $2|e|E_{cr}\lambda_C = 2mc^2$ which gives the value of $E_S = m^2c^3/|e|\hbar = 1.32 \times 10^{18}$ V/m. So the tunneling probability becomes

$$W \sim \exp\{-\frac{\pi E_{cr}}{E_0}\} \tag{1.4}$$

which is in good agreement with exact formula of the pair production rate per unit volume per unit time by Schwinger formula [1]

$$W = \frac{|e|^2 E_0^2}{4\pi^3\hbar^2 c} \exp\{-\frac{\pi E_{cr}}{E_0}\}. \tag{1.5}$$

The generalization of the Schwinger formula of pair production rates per unit volume and per unit time in the presence of the constant electric and magnetic fields with fields strength E_0 and H_0 was derived by Nikishov [3] and resulted in the final form

$$W = \frac{|e|^2 E_0 H_0}{4\pi^2\hbar^2 c} \coth(\frac{\pi H_0}{E_0}) \exp\{-\frac{\pi E_{cr}}{E_0}\}, \tag{1.6}$$

where E_0 and H_0 are the invariant electric and magnetic fields in the Lorentz transformed frame where both the fields are parallel. These invariant fields are defined by the Lorentz invariants for the electric and magnetic fields $\mathbf{E}$ and $\mathbf{H}$ as follows: the Lorentz scalar $\mathcal{F}$ and pseudoscalar $\mathcal{G}$ are $\mathcal{F} = (\mathbf{E}^2 - \mathbf{H}^2)/2$ and $\mathcal{G} = \mathbf{E} \cdot \mathbf{H}$. The normalized invariant electric and magnetic fields are defined as $\epsilon = E_0/E_S$ and $\eta = H_0/E_S$ where $(\mathcal{E}, \mathcal{H}) = \sqrt{(\mathcal{F}^2 + \mathcal{G}^2)^{1/2} \pm \mathcal{F}}$ in the centre of momentum frame of the field. For the plane wave in vacuum both the Lorentz invariants are zero and therefore pair production is not possible whatever may be the strength of the field. Here it is justified because for the plane wave, all the wave vectors are moving parallel and therefore there is no centre of momentum frame of the field with non zero invariant mass density of the field [4]. This process was foreseen theoretically several decades ago [5–9], its experimental verification is still missing because of the unavailability of an electric field strength comparable to the Schwinger limit E_S. Since the probability of pair production from vacuum by a strong electric field of strength E_{peak} is proportional to $\exp(-\pi E_S/E_{peak})$, the process is exponentially suppressed for $E_{peak} \ll E_S$. The pair production rate shows that it is a non-perturbative process with the electric charge e and needs to evaluate exactly.

A simple way to meet the criteria of non zero Lorentz invariants is to use focused ultra-short and ultra-intense laser beam(s). The focused laser beams can be described by the various field models such as Narozhny-Fofanov (N-F) field model for weakly focused pulse [10], tightly focused field model [11, 12] and optimally focused field model [13, 14]. Use of two or many counterpropagating laser beams have been shown to reduce the intensity threshold much below the critical intensity [15, 16]. In these field configurations, the magnetic field vanishes in the focus and thereby enhancing the pair production rate [17, 18]. Furthermore, because of the formation of the standing wave pattern in the focal plane the peak field strength of the electric field increases. Consequently, several theoretical studies have explored various aspects of pair production using the counterpropagating beam configuration of focused laser beams such as enhancement of the production rate [11, 15, 16], momentum distribution of the created particles [19, 20], dynamically assisted Schwinger mechanism [20–23], barrier control tunneling mechanism in e^+e^- photoproduction [24], and spin-polarization state of the created particles on the laser field polarization [25]. While, there is a quest to achieve ultraintense lasers to experimentally realize some of the strong field QED effects, Fedotov *et al.,* have analyzed an issue of fundamental importance, that is, if there are any limitations on the attainable intensity for high power lasers [26]. It has been shown that even a single e^+e^- pair created by a superstrong laser field in the vacuum would cause the development of an avalanche-like QED cascade which rapidly depletes the incoming laser pulse. In the light of this work, the configurations of laser beams which diminish pair production, also assume significance. For example, a perpendicular magnetic field has been shown to effectively control - even to the extent of completely halting the pair production by the supercritical static electric field [17, 18].

1.1 Different formalism of pair production processes

The simple realization of materialization process by pair production from high energetic gamma photon can be done if we consider two photons with four momenta k_1^μ and k_2^μ collide at an angle, such that the invariant parameter $\eta = \frac{k_1 k_2}{m^2} > 2$ [27] then the creation of electron and positron pair is kinematically allowed. The additional source is required to get kinematically allowed pair production for a single gamma photon. In general there are three possibilities of pair production known so far which are i) pair production by a high energy gamma photon propagating in a strong laser field (Breit-Wheeler pair production in a multiphoton regime), ii) pair production by a Coulomb field in the presence of a strong laser electromagnetic field, iii) vacuum pair production by the strong electric field of laser in tunnelling regime via Schwinger mechanism.

In this thesis, we mainly focus on the pair production process via Schwinger processes which is the non-perturbative signature of vacuum decay process in the presence of a constant background field. This process was studied in a more general field theoretic approach in the presence of a constant electric field background by Schwinger [1] using proper time propagator. Although for the characteristic length and time scales of the process is Compton length and time scale which are much smaller than the present day radiation field wavelength and the time period. Therefore one can use spatiotemporaly inhomogeneous field to calculate the pair production rates using a locally constant field approximation. This methodology has the advantage to use laser pulses because laser light is the potential source of such high electric field at the focus. For a real space and time-dependent field of the ultrashort and ultraintense laser pulses offers new challenges. This has resulted in the development of numerous theoretical approaches for the space/time varying fields which has been formulated using the WKB method [28] and the worldline instanton method [29]. Recognising the equivalence of the pair production process to the over-the-barrier scattering problem in quantum mechanics [30], the structure of the turning points in the complex time plane [31] was used to calculate the longitudinal momentum spectrum of the created particle at the asymptotic time for a spatially uniform time dependent electric field. A full fledged dynamical description of pair creation process for time varying fields is possible within the framework of the quantum kinetic approach using the quasi-particle [32] representation (for spatially homogeneous fields) and the Wigner representation [33] (for spatially inhomogeneous fields).

1.2 Schwinger mechanism realization by the ultrashort and ultraintense laser source

The available electric field strength for the present-day laser systems is of the order of $E_{peak} \sim 10^{13} - 10^{14}$ V/m [34], considerably below the critical field limit E_S. However, recent advances in laser technology, especially the use of chirp pulse amplification method, have made it possible to generate ultrashort laser pulses in deeply relativistic regime [35]. The European Extreme Light Infrastructure for Nuclear Physics (ELI-NP) is planning to build a 10 PW pulsed laser to achieve intensities $I \sim 10^{23}$ W/cm^2 for the first time for investigating new physical phenomena at the interfaces of plasma, nuclear and particle physics [36, 37]. The electric field at the laser focus will have a maximum value of 10^{15} V/m at such intensities. In the ELI-NP experimental area E6, it is proposed to study radiation reactions, strong field QED effects and the resulting production of ultrabright gamma rays which could be used for nuclear activation. The construction of X-ray free electron laser (XFEL) is underway at DESY, Hamburg using self-amplified spontaneous emission (SASE) principle [38]. In a landmark experiment E144 at Stanford Linac Acceleration centre (SLAC) in 1997 it was possible to observe non-linear QED processes like non-linear Compton scattering and stimulated pair production in the collision of a 46.6 GeV electron beam with counterpropagating laser pulses with photon energy 2.4eV and laser field intensity $I = 1.38 \times 10^{18} W/cm^2$ [39, 40]. Although these multi-photon processes pertain to the perturbative regime of QED, the successful experimental realizations thereof raise the hope for the experimental verification of the Schwinger mechanism in coming decades.

The aforesaid developments renewed interest in theoretical studies of pair production by intense optical lasers. Using the realistic focused field models, e.g. a weakly focused field in paraxial approximation [10], tightly focused field models [12, 41], and the optimally focused field model of e-dipole pulses [17], it was demonstrated that pair production can take place even at intensities substantially lower than the critical intensity $I_S = \frac{c}{4\pi} E_S^2$ (here c denotes the light velocity in vacuum). Superposition of laser pulses in a counterpropagating configuration has been shown to lower the threshold value of the required field strength considerably [15]. Such beam configurations were extensively used to study various aspects of pair production, including the dynamics of post-production.

1.3 Motivation of the present work

The validation of the Schwinger pair production process can be achieved by the use of ultrashort and ultraintense laser pulses at the focus which has non zero Lorentz invariants. Therefore it is essential to have the exact analytical expression of the electric and magnetic fields at the focus to get the desired Lorentz invariants and hence the invariant electric and magnetic fields. The focusing generates the longitudinal components at the focal region and the EM field is no more transverse. The relative contribution of the transverse and the longitudinal components of the electric field introduces the concept the beam polarization with a parameter of asymmetry [15]. So our first motive is to study how the spatiotemporal distribution of the EM fields at the focal region with different beam polarization will determine the spatiotemporal distribution of the invariant electric fields and hence the pair production rates.

Ultrashort laser pulse propagation has a significant dependence on the carrier-envelope phase (CEP) which is basically the phase difference between the carrier wave and the envelope of the pulse profile [42–44]. It has the significant bearing on the QED processes like pair production, Compton effects etc. In fact, the determination CEP can be taken place as reported in Ref. [42] where the angular distribution of photons emitted by an electron via multiphoton Compton scattering due to an intense laser pulse has been shown. It is shown that the reported study [42] has direct dependence on CEP of the laser pulse. How this parameter affects the spatiotemporal distribution of the invariant electric and magnetic fields and consequently the distribution of produced pairs is our second motive.

There is a possibility that the colliding pulses have relative phase difference. This may alter the spatiotemporal distribution of the EM fields at the focus. Apart from the geometrical optimization of the focus beams the relative phase of the two colliding pulses alter the desired peak position of electric field in the transformed frame. Hence the dependence of relative phase of the colliding pulses may offer us a good scheme of the generation of particle production rates in the focal volume.

The validity of Schwinger's formula to compute the spatio-temporal distribution of pairs created by time and space varying fields due of ultrashort and ultraintense laser pulses with the justification that the length and time scales of the variation are much larger than the characteristic Compton length and time. However, as the pulse duration is reduced further in the range of few hundreds of atto-second when it is no more much larger than the characteristic Compton time, use of Schwinger formula to describe the pair production rate is questionable. The later section of the thesis we use the quantum kinetic approach using quantum Vlasov equation (QVE) [19, 31, 45–60]. This methodology has a strong relevance in the context of the momentum distribution of the created pairs in semiclassical approximation where the asymptotic reflection coefficient gives the average particle numbers in a particular mode [61]. The theory was used to study the rich dynamical behaviour of the pair creation process for the time dependent but spatially homogeneous field configuration [19, 53, 62]. The ultrashort pulses Gaussian and Sauter are the two most commonly used (quite often interchangeably) temporal profiles. A simple Sauter pulse without any subcycle oscillation (also known as single sheeted Sauter pulse) offers analytical solutions for the momentum distribution [56] and the dynamics of produced pairs [49]. However, a Sauter pulse with subcycle oscillations (multi sheeted pulse) is no longer analytically tractable. On the other hand, for a multi sheeted Gaussian pulse it is possible to express the vector potential in an analytically closed form in terms of error function. These analytical conveniences have led researchers to use Sauter and Gaussian temporal profiles for the kinetic studies of the pairs created by the single sheeted and multi sheeted pulses, respectively [31]. This is possibly due to the perception that both the pulses should give very similar results because of their close resemblance. This, to the best of our knowledge, has not been verified so far. This is one of the motivations of this study. While the evolution of individual modes was studied in Ref. [59, 60], the evolution of the momentum distribution as a whole has not been reported so far. This is the second motivation of our study. We, therefore, use quantum kinetic equation to present a detailed comparative study of the evolution of longitudinal momentum distribution of the pairs created by these two pulses (Sauter and Gaussian) for a given pulse duration, number sub-cycle oscillations, CEP, and frequency chirp.

The quantum kinetic formalism has the potential to see the complete evolution process of the single particle distribution function. Here pair production process may be viewed as a field-induced phase transition (FIPT) of the vacuum state [59]. The evolution of the order parameter of the phase transition is studied for multi-sheeted Sauter pulse with higher order frequency chirp parameter. Pair production in strong EM field allows to analyse the inter-relation between the entropy production and irreversibility in systems which show reversibility at microscopic level [63]. In this thesis, the evolution of the von Neumann entropy function for a few cycle Sauter pulses is studied. The non-monotonic entropy growth has been observed with oscillatory structures. This thesis is organized into seven chapters a brief description of which is as follows.

1.4 Overview of the present work

In **Chapter 2** we study pair creation for different state of beam polarization of the EM field of two counterpropagating laser pulses. The characteristic parameter for the beam polarization is given by the parameter of asymmetry μ [64] between e-and h-waves in the field expression where e (h)-wave refers to the EM field in which only electric (magnetic) field is purely transverse with respect to the propagation direction [10]. The main aim of revisiting this topic is to know how the pairs are distributed in spatiotemporal coordinates for different values of μ. It is found that the beams made up of entirely e-and h-waves ($\mu = \mp 1$) are the most effective for pair production whereas the beam having equal mixture of e-and h-waves ($\mu = 0$) is the worst for pair production [15]. In this chapter, we explain these observations by the structure of underlying fields. Though $\mu = 0$ case is not suitable for efficient pair production, it is found to be appropriate for generating shorter bunches of electrons and positrons [65].

Ultrashort laser pulses are characterized by CEP which is inherent to the process of their generation [42]. The effect of CEP on the spatiotemporal distribution of electron-positron pairs created by ultra-intense counterpropagating femtosecond laser pulses is studied in **Chapter 3**. When the laser pulses are linearly e-polarized, the temporal distribution of the pairs is found to be sensitive to CEP. Same analysis is extended for the circularly e-polarized laser pulses. It is seen that when the counterpropagating laser pulses are both right and left circularly polarized, the effect of CEP is insignificant. On the other hand when the superimposed fields are in the combination of right and left circular polarizations, the CEP dependence shows up in the invariant electric and magnetic fields structure and hence it reflects in the particle-antiparticle temporal distribution. However, the total number of pairs is not greatly influenced by CEP for both the polarizations [66].

In **Chapter 4** we have studied the pair production mechanism by a strong EM field of two colliding e-polarized laser pulses with a relative phase shift Ψ. The spatio-temporal distribution of created pairs is very sensitive to this phase shift and to polarization of the pulses. We have analysed this dependence in detail and demonstrate how it can be explained in terms of the underlying invariant electric field structure of the counterpropagating focused pulses which is spiky. We find that the total pair production is larger when one of the spikes is located near the centre of the spatiotemporal envelope (and the distribution of created pairs looks approximately unimodal), and smaller when the neighboring spikes are off-centered but located symmetrically. The particular phase shift required for each case depends on the polarization of the pulses. Among the considered cases, for the parameters adopted in this study the global maximum for the total number of pairs is achieved with the circularly e-polarized counterpropagating pulses having the same sense of rotation with no relative phase difference as considered in Ref. [15]. Possibility of phase control of Schwinger pair production may be useful, e.g., to increase the attainable intensity of tightly focused colliding laser pulses by reducing pair production and hence preventing field depletion at their crossing, or, conversely, to measure the typically unknown field structure and phase relations of extremely strong laser pulses [67].

Effect of temporal pulse shape of intense few cycle ultrashort laser pulses on the momentum distribution of e^+e^- pairs is studied using quantum kinetic equation in **Chapter 5**. Single and multi-sheeted Gaussian and Sauter pulses, are considered to this end. For multi-sheeted pulses having a few cycle of oscillations the temporal profile of the pulse is revealed in the interference pattern in the momentum spectrum at asymptotic times. The onset of the oscillation due to the quantum interference between the neighbouring turning point structures takes place for fewer subcycle oscillations for the Gaussian pulse than that for the Sauter pulse. Furthermore, the oscillation amplitude for the same number of subcycle oscillations within the pulse duration is larger for the Gaussian pulse. The presence of the carrier offset phase and the frequency chirping is found to magnify these differences. These observations are explained in terms of the turning point structure in complex t-plane and invoking the concept of over the barrier scattering. The momentum spectrum of the created particle-antiparticle pairs being very sensitive to the shape of temporal envelope may provide a way to measure it for the ultrashort laser pulses.

Pair production in the presence of a time dependent electric field may be viewed as a FIPT [58, 59]. In **Chapter 6**, we have studied the evolution of the order parameter associated with FIPT of the vacuum state for the time dependent multi-sheeted Sauter pulse. In particular, the effect of the time dependent frequency of the electric field due to the higher order frequency chirping is investigated. We limit our study up to the quadratic frequency chirping for the different evolution stages of the order parameter e.g., the quasi electron positron plasma stage, the transient stage and the residual electron-positron plasma stage. In the presence of the quadratic frequency chirping, the formation of pre-transient region is observed at earlier times before the electric field attains its maximum value. The t non-invariant particle distribution function results in the non-monotonic increase in von Neumann entropy [57, 63]. We study the effect of sub-cycle pulse oscillations on the evolution of the entropy and the particle density for different values of subcycle oscillations.

In **Chapter 7**, we summarize the major outcomes of our studies on electron-positron pair production via Schwinger mechanism by ultrastrong and ultrashort laser EM fields and discuss the future outlook.

Chapter 2

Effect of polarization on the structure of electromagnetic field and spatiotemporal distribution of e^+e^- pairs generated by colliding laser pulses

In **Chapter** 1 we have discussed that to meet the criteria of non zero EM field invariant it is required to use focused laser pulses. But focusing introduces longitudinal field component and we can not define the exact polarization of the EM field. In vacuum, Maxwell equation is linear and one can use superposition principle to write the general EM field at any arbitrary space time position which is the linear superposition of transverse and longitudinal components. In this **Chapter** we study the pair creation mechanism for the different state of beam polarization of the EM field of two counterpropagating laser pulses. The characteristic parameter for the beam polarization is given by the parameter of asymmetry μ [64] between e-and h-waves in the field expression. The main aim of revisiting this topic is to know how the pairs are distributed spatially and temporally for different values of μ. It has been reported that the beams of entirely e-and h-waves ($\mu = \mp 1$) are effective for pair production whereas the beams with an equal mixture of e-and h-waves ($\mu = 0$) are the worst for pair production [15]. So here we analyse this observation from the structure of underlying fields. Though $\mu = 0$ case is not suitable for efficient pair production, it is found to be appropriate for generating shorter pulses of electrons and positrons.

This **Chapter** is organized as follow. In the Sec. 2.1 we discuss the basic understanding of the pair creation mechanism in the presence of EM field. The structure of EM fields, the field invariants and the invariant fields is analysed for different values of μ, with the reference to its possible role in pair production in this section. In Sec. 2.2 we discuss the spatiotemporal distribution of EM fields in both the frames. The polarization dependence of the spatiotemporal distribution of the pairs is also presented in this section. We conclude in Sec. 2.3. The technical details are given in **Appendix** A.

2.1 Theoretical background and field model

In the presence of a strong uniform electric field the vacuum depletion process gives rise to e^-e^+ pair production [1, 68]. The EM field associated with a typical ultrashort laser pulse having wavelength and pulse duration of the order of a micron and a few tens of femtosecond can be taken as uniform in space-time over the Compton length and time scales [1]. Then the average number of created pair is calculated by the [1, 16]

$$N_{e^-e^+} = \frac{e^2E_S^2}{4\pi^2\hbar^2 c}\int dV\int dt\epsilon\eta\coth(\frac{\pi\eta}{\epsilon})\exp(-\frac{\pi}{\epsilon}). \tag{2.1}$$

Here $\epsilon = \mathcal{E}/E_S$, $\eta = \mathcal{H}/E_S$, and $(\mathcal{E},\mathcal{H}) = \sqrt{(\mathcal{F}^2+\mathcal{G}^2)^{1/2}\pm\mathcal{F}}$ are the invariant electric and magnetic fields in the reference frame in which they are parallel to each other and $\mathcal{F} = (\mathbf{E}^2 - \mathbf{H}^2)/2$, $\mathcal{G} = \mathbf{E}\cdot\mathbf{H}$ are Lorentz invariants of the EM field. In order to have the non-zero Lorentz invariants focused EM fields are used. According to Narozhny-Fofanov (N-F) field model [10] the focused EM field does not possess any definite state of polarization. However it can always be represented as a superposition of e-and h-waves: $\mathbf{E} = (1-\mu)\mathbf{E}^e/2 + (1+\mu)\mathbf{E}^h/2$, and $\mathbf{H} = (1-\mu)\mathbf{H}^e/2 + (1+\mu)\mathbf{H}^h/2$. Here e(h)-wave is the totally transverse electric (magnetic) field with respect to the propagation direction [10]. In this chapter we consider two right circularly polarized laser beams propagating in the $+z$ (forward) and $-z$ (backward) directions both having their focal region at the origin. Using the N-F field model which is valid in the weak focusing limit (focusing parameter, $\Delta << 1$), the expression of the real part of the electric and the magnetic fields due to the superposition of forward and backwards propagating e-waves are given as

$$\mathbf{E}^e \approx 2E_0 g\frac{e^{-\frac{\xi^2}{1+4\chi^2}}}{(1+4\chi^2)}\Big[\sin\omega t\Big\{\cos\omega z/c - \frac{2\xi^2\sin\phi}{(1+4\chi^2)^{1/2}}\sin(\phi+\omega z/c)\Big\}\hat{\mathbf{e}}_x - \cos\omega t\Big\{\cos\omega z/c - \frac{2\xi^2\cos\phi}{(1+4\chi^2)^{1/2}}\cos(\phi+\omega z/c)\Big\}\hat{\mathbf{e}}_y\Big], \tag{2.2}$$

and

$$\mathbf{H}^e \approx 2E_0 g \frac{e^{-\frac{\xi^2}{1+4\chi^2}}}{(1+4\chi^2)}\Bigg[\sin\omega t\Big\{\sin\omega z/c - \frac{2\xi^2\cos\phi}{(1+4\chi^2)^{1/2}}\sin(\phi+\omega z/c)\Big\}\hat{\mathbf{e}}_x - \cos\omega t\Big\{\sin\omega z/c - \frac{2\xi^2\sin\phi}{(1+4\chi^2)^{1/2}}\cos(\phi+\omega z/c)\Big\}\hat{\mathbf{e}}_y - \frac{8\Delta\xi}{(1+4\chi^2)^{1/2}}\cos(\phi+\omega z/c)\cos\omega t\,\hat{\mathbf{e}}_z\Bigg]. \tag{2.3}$$

Here, ω is the frequency of the laser pulse, λ is the wavelength, Δ is the focusing parameter; x, y, and z are the spatial coordinates; $\rho = \sqrt{x^2+y^2}$, $\xi = \rho/R$, $\chi = z/L$, $\exp(i\phi) = (x+iy)/\rho$, $\Delta = c/\omega R = \lambda/2\pi R$, $L = R/\Delta$, and g is the temporal pulse envelope to account for the finite pulse width of the laser beams and it is taken as $g = \exp(-4(t^2/\tau^2 + z^2/c^2\tau^2))$. The pulse duration τ is taken to be $10fs$. The technical details of the derivation are relegated to **Appendix** A. Using the Eqs. (2.2,2.3), the expression of the Lorentz invariants are given as

$$\mathcal{F}^e \approx \frac{2E_0^2 g^2 e^{-\frac{2\xi^2}{1+4\chi^2}}}{(1+4\chi^2)^2}\Bigg[\cos 2\omega z/c - \frac{2\xi^2}{(1+4\chi^2)^{1/2}}\Big\{\cos 2\omega z/c + \cos 2\omega t\cos 2\phi\Big\} + O(\xi^4)\Bigg], \tag{2.4}$$

$$\mathcal{G}^e \approx \frac{2E_0^2 g^2 e^{-\frac{2\xi^2}{1+4\chi^2}}}{(1+4\chi^2)^2}\Bigg[\sin 2\omega z/c - \frac{2\xi^2}{(1+4\chi^2)^{1/2}}\Big\{\sin 2\omega z/c - \cos 2\omega t\sin 2\phi\Big\} + O(\xi^4)\Bigg]. \tag{2.5}$$

When the counterpropagating beams are made up of h-waves, it follows from the duality [10] (see **Appendix** A) that $\mathcal{F}^h = -\mathcal{F}^e$, $\mathcal{G}^h = \mathcal{G}^e$.

For the case when the counterpropagating pulses are made up of the equal mixture of e- and h-waves, using the expressions of $\mathbf{E}^{e+h}$ and $\mathbf{H}^{e+h}$ derived in **Appendix** A, the expressions of $\mathcal{F}^{e+h}$ and $\mathcal{G}^{e+h}$ become

$$\begin{aligned}\mathcal{F}^{e+h} &\approx -A\Big[\cos 2(\omega t+\phi-\psi/2) - \frac{16\Delta^2\cos 2\omega t}{(1+4\chi^2)^{1/2}}\cos^2(\phi+\omega z/c) - \frac{\xi^2\cos 2(\omega t+\phi)}{(1+4\chi^2)^{1/2}}\Big]\\ \mathcal{G}^{e+h} &\approx A\Big[\sin 2(\omega t+\phi-\psi/2) - \frac{16\Delta^2\sin 2\omega t}{(1+4\chi^2)^{1/2}}\cos^2(\phi+\omega z/c) - \frac{\xi^2\sin 2(\omega t+\phi)}{(1+4\chi^2)^{1/2}}\Big],\end{aligned} \tag{2.6}$$

where $A = 2E_0^2 g^2\xi^2\exp(-2\xi^2/1+4\chi^2)/(1+4\chi^2)^{5/2}$. At this point it may be worthwhile to compare the expressions of invariants $\mathcal{F}$ and $\mathcal{G}$ for $\mu = 0$ with those for $\mu = \mp 1$. First, the amplitude part of $\mathcal{F}$ and $\mathcal{G}$ for $\mu = 0$ has a factor of ξ^2 which makes it negligibly small in the focal region where $\xi \ll 1$. Away from the focal region ξ^2 increases but the amplitude is exponentially suppressed by the Gaussian profile factor $\exp(-2\xi^2/(1+4\chi^2))$. Therefore the amplitudes of $\mathcal{F}$ and $\mathcal{G}$ for $\mu = 0$ are always much smaller to those for $\mu = \mp 1$ which do not have ξ^2 dependence in the leading order.

Second, the phase part of invariants for $\mu = -1$ shows oscillatory behaviour along the propagation direction with a length scale of the order $2\pi c/\omega$ which is quite expected feature associated with the standing wave formation. This type of interference, which gets carried over to the reduced field invariants ϵ and η (see Eq. 2.7) is the root cause of effective pair production by the two laser beams. As $\mathcal{G}^e/|\mathbf{E}^e||\mathbf{H}^e| \approx 1 - O(\xi^2)$ near the focus, the electric and magnetic fields in the focal region are nearly parallel to each other in the lab frame.

The expressions of the reduced invariant electric and magnetic fields for $\mu = -1$ in the limit of small χ, ξ in the focal region are given as

$$\epsilon^e \approx \frac{2E_0 g e^{-\frac{\xi^2}{1+4\chi^2}}}{(1+4\chi^2)} |\cos \omega z/c| \left[1 - \frac{\xi^2}{(1+4\chi^2)^{1/2}} \left\{ 1 + \cos 2\omega t \cos 2\phi \right\} + O(\xi^4) \right], \tag{2.7}$$

and

$$\eta^e \approx \frac{2E_0 g e^{-\frac{\xi^2}{1+4\chi^2}}}{(1+4\chi^2)} |\sin \omega z/c| \left[1 - \frac{\xi^2}{(1+4\chi^2)^{1/2}} \left\{ 1 - \cos 2\omega t \cos 2\phi \right\} + O(\xi^4) \right]. \tag{2.8}$$

For h-wave beams, the reduced electric and magnetic fields are given $\epsilon^h = \eta^e$ and $\eta^h = \epsilon^e$. Finally, the reduced invariant fields for $\mu = 0$ can be expressed as

$$\epsilon^{e+h} \approx \frac{2E_0 g e^{-\frac{\xi^2}{1+4\chi^2}} \xi}{(1+4\chi^2)^{5/4}} |\sin(\omega t + \phi - \psi/2)| \left[1 - \frac{8\Delta^2 \cos^2(\phi + \omega z/c) \sin(\omega t - \phi + \psi/2)}{(1+4\chi^2)^{1/2} \sin(\omega t + \phi - \psi/2)} + O(\xi^2) \right], \tag{2.9}$$

and

$$\eta^{e+h} \approx \frac{2E_0 g e^{-\frac{\xi^2}{1+4\chi^2}} \xi}{(1+4\chi^2)^{5/4}} |\cos(\omega t + \phi - \psi/2)| \left[1 - \frac{8\Delta^2 \cos^2(\phi + \omega z/c) \cos(\omega t - \phi + \psi/2)}{(1+4\chi^2)^{1/2} \cos(\omega t + \phi - \psi/2)} + O(\xi^2) \right]. \tag{2.10}$$

The above expressions for ϵ and η are derived in the small χ, ξ approximation in order to understand the physical origin of the pair production in terms of the structure of EM fields and the invariants in the focal region. It is clear that the qualitative features of the invariants $\mathcal{F}$ and $\mathcal{G}$ get translated into reduced field invariants ϵ and η. As before the amplitudes of ϵ and η are the same in all the cases. While it is maximum for $\xi = 0$ for $\mu = -1$ it identically vanishes for $\mu = 0$ case and is much smaller for any other value of ξ because of the presence of the factor ξ in the leading order term for the amplitude in the latter case. For $\mu = \mp 1$ both ϵ and η show oscillatory behaviour with phase difference of $\pi/2$ with spatial frequency $\approx 2\pi\omega/c$ in z-direction, the propagation direction. The origin of this oscillation, as discussed earlier, is the interference of the counterpropagating beams. This type of oscillation is absent in ϵ and η for $\mu = 0$. However, it shows oscillatory behaviour in time. For $\mu = -1$, ϵ shows a maximum for $\xi = 0$ and $\chi = 0$. Consequently the spatial distribution of e^+e^- pairs would show a peak at the centre of the focal spot. However, for $\mu = 1$, ϵ is minimum for $\xi = \chi = 0$ and hence the spatial distribution of e^+e^- pairs will show a dip right at the centre of the focal spot. We will return this point later.

2.2 Results and Discussion

As discussed in the previous section the invariant fields are quite sensitive to the polarization of the colliding pulses. In this section we discuss the spatiotemporal distribution of the invariant fields, ϵ and η, their relationship with the fields in the lab frame and finally the distributions of the created pairs for various polarization states of the colliding pulses.

2.2.1 Pulses made up of purely e-waves ($\mu = -1$)

The invariant electric field given by Eq. 2.7 shows striking similarities with magnitude of the corresponding electric field in the lab frame given by Eq. B.20. In fact, comparing the expression of $|\mathbf{E}^e|$ in Eq. B.22 with that of ϵ^e reveals that the two differ only by terms of the order of ξ^2 or higher. Thus the two are identical for $\xi = 0$ and nearly identical in the entire focal region where $\xi < 1$. The same holds good for the invariant magnetic field η^e Eq. 2.3 and $|\mathbf{H}^e|$ the magnitude of the magnetic field in the lab frame Eq. B.23. This point is illustrated in Fig. 2.1 which shows the distribution of the fields, ($|\mathbf{E}^e|$, ϵ^e) at the top and ($|\mathbf{H}^e|$, η^e) at the bottom, as a function of the normalized longitudinal coordinate χ for $\xi = 0.8$ and $t = 0.3\tau$. The fields in both the frames are nearly same even for the regions close to the periphery of the focal region. The field distributions form standing wave patterns with decreasing amplitude within the pulse envelope function g. The multiple maxima of the field oscillations are spaced by $\approx 0.03272L$ along the propagation direction. The electric field distribution has a dominant central lobe located at $\chi = 0$. On the other hand, the magnetic field distribution has two equally dominant side lobes located on either side of its minimum at $\chi = 0$. The longitudinal extent of the focused field in both the cases is up to $\chi = \pm 0.2$ and is symmetrical about $\chi = 0$.

Since that ϵ and η have the meaning of the electric and magnetic fields in the Lorentz frame in which they are parallel to each other, their approximate equality to the respective fields in the Lab frame follows from the fact that the e-polarized counterpropagating pulses produce nearly

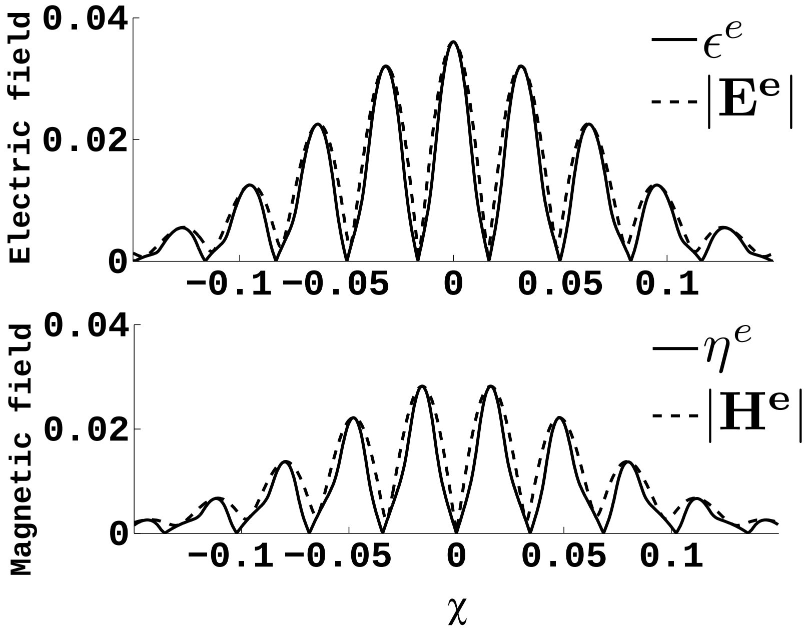

FIGURE 2.1: (Top) $|\mathbf{E}^e|$, ϵ^e, and (Bottom) $|\mathbf{H}^e|$, η^e as function of χ for the counterpropagating laser beams with $\mu = -1$. $\xi = 0.8$, $t = 0.3\tau$, and $\phi = \pi/2$. The field parameters are: $E_0 = 0.0565E_S$, $\Delta = 0.1$, $\lambda = 1\mu m$, and $\tau = 10fs$.

parallel electric and magnetic field in the focal region as already mentioned in the previous section. This may be further analysed by invoking the well known result [4, 69] that for given non-orthogonal $\mathbf{E}$ and $\mathbf{H}$ fields one can achieve the frame of ϵ and η by the Lorentz boost $\mathbf{V}$ (in the units of c) such that $\mathbf{V}/(1+V^2) = (\mathbf{E}\times\mathbf{H})/(|\mathbf{E}|^2+|\mathbf{H}|^2)$. In this case, for $\mu = -1$, the components of $\mathbf{C}^e (= \mathbf{E}^e \times \mathbf{H}^e)$ and $\mathbf{V}^e$ are given as

$$C_x^e \approx \frac{16E_0^2 g^2 e^{-\frac{2\xi^2}{1+4\chi^2}}\Delta\xi\cos\phi}{(1+4\chi^2)^{5/2}}\cos^2\omega z/c\sin 2\omega t \quad V_x^e \approx -\frac{\Delta\xi\sin 2\omega t}{(1+4\chi^2)^2}\cos\omega z/c, \tag{2.11}$$

$$C_y^e \approx \frac{32E_0^2 g^2 e^{-\frac{2\xi^2}{1+4\chi^2}}\Delta\xi\cos\phi}{(1+4\chi^2)^{5/2}}\cos^2\omega z/c\sin^2\omega t \quad V_y^e \approx -\frac{2\Delta\xi\sin^2\omega t}{(1+4\chi^2)^2}\cos\omega z/c, \tag{2.12}$$

and

$$C_z^e \approx -\frac{4E_0^2 g^2 e^{-\frac{2\xi^2}{1+4\chi^2}}\xi^2\sin 2\phi}{(1+4\chi^2)^{5/2}}\sin 2\omega t \quad V_z^e \approx -\frac{\xi^2\sin 2\phi}{2(1+4\chi^2)^{1/2}}\sin 2\omega t. \tag{2.13}$$

As both ξ and $\Delta \ll 1$, $|\mathbf{V}^e|$ is negligibly small in the focal region and vanishes at $\xi = 0$. This explains the observation that the transformation from $(\mathbf{E}, \mathbf{H})$ to (ϵ, η) is nearly identity near the focal region and for the special case of $\xi = 0$ it is exactly identity. The physical consequence of a very small value of $|\mathbf{C}^e|$, in the focal region, is that a very small amount of EM energy flows out from the focal region and thereby resulting in an efficient pair production for counterpropagating beams with $\mu = -1$. Furthermore, since $|\mathbf{C}^e|$ is proportional to Δ, a smaller value of Δ will lead to a larger number of pairs. This effect has been attributed to the increase in the focal volume in the literature [15]. However, the explanation given here is more direct and physical. In view of the near equality of the fields in both the frames, it is natural to examine if one can use the expressions for the magnitude of electric and magnetic fields in the lab frame instead of those for ϵ and η for calculating the number of pairs using the Eq. 2.1. We use the field expressions in both the frames and calculate the number of pairs which is tabulated in Table 2.1. The first column shows the results of using fields $|\mathbf{E}^e|$ and $|\mathbf{H}^e|$ in the place of ϵ^e and η^e. The second column shows the results using ϵ^e and η^e. It is seen that the number of pairs is almost same in column 1 and 2. One immediate ramification of this observation is that one can work in the lab frame for the circularly colliding pulses made of e-waves. This would offer enormous simplification for analytical calculation and thus may help in getting the physical insight of the underlying process. Having discussed the structure of the EM fields in the focal region

$I \times 10^{27} W/cm^2$	$N_{e^+e^-}(\lvert\mathbf{E}^e\rvert, \lvert\mathbf{H}^h\rvert)$	$N_{e^+e^-}(\epsilon^e, \eta^e)$
0.2	3.7157	3.5269
0.3	2.1308(4)	2.0135(4)
0.4	4.1661(6)	3.9253(6)
0.5	1.5907(8)	1.4944(8)
0.6	2.4276(9)	2.2782(9)
0.7	2.0694(10)	1.9375(10)
0.8	1.1857(11)	1.1091(11)
0.9	5.158(11)	4.82(11)
1	1.7912(12)	1.6723(12)

Table 2.1: $N_{e^+e^-}$ calculated using Eq. 2.1 for different values of intensities of the counterpropagating laser beams with $\mu = -1$. This is shown in the last column. The middle column shows the number of pairs when ($|\mathbf{E}^e|$,$|\mathbf{H}^e|$) are used in place of (ϵ^e,η^e) in Eq. 2.1 for the calculation. $\Delta = 0.1$, $\tau = 10fs$, and $\lambda = 1\mu m$. The numbers in the brackets indicate in powers of 10.

and their relationship with the reduced field invariants, we now investigate the spatiotemporal distribution of the created pairs in the focal region. For convenience, we define the differential particle distribution with respect to a particular space or time coordinate which is integrated over all the other coordinates except for the coordinate under the consideration. This obviously gives the derivative of $N_{e^+e^-}$ with respect to that coordinate. Such a differential particle distribution provides a measure to know the space-time extent of the pairs in the focal region. These differential distribution closely follows the distribution of the invariant electric field ϵ or $|\mathbf{E}|$ (as

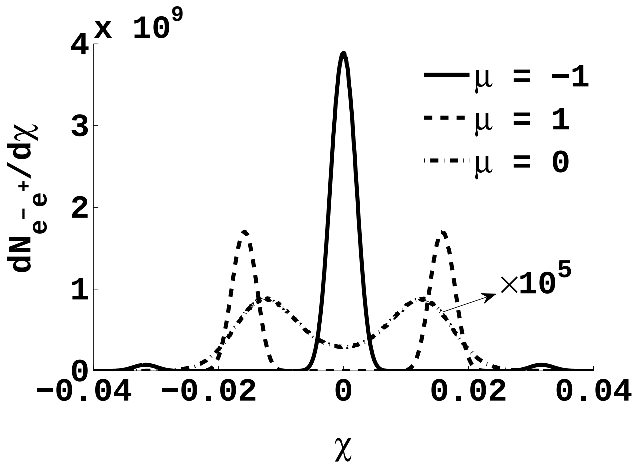

FIGURE 2.2: The differential pair distributions for the counterpropagating laser beams with $\mu = -1,\ 1$, and 0 as a functions of χ. The data for $\mu = 0$ is multiplied by a factor of 10^5. The field parameters are same as those in Fig. 2.1.

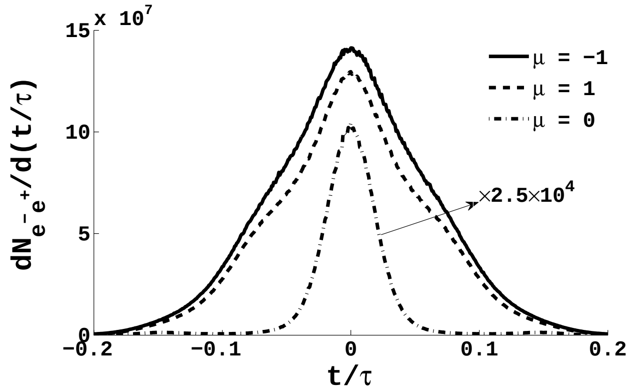

FIGURE 2.3: The differential pair distributions for the counterpropagating laser beams with $\mu = -1,\ 1$, and 0 as a functions of t/τ, the scaled time. The data for $\mu = 0$ is multiplied by the factor of 2.5×10^4. The field parameters are same as those in Fig. 2.1.

discussed above). The consequence of the standing wave formation in the electric field distribution is manifested in the spiky differential particle distribution $dN_{e^+e^-}/d\chi$ along the propagation direction Fig. 2.2. It implies that the pair production takes place in a smaller region of the central antinode of the electric field distribution at $\chi = 0$. The longitudinal extent of the pairs is $0.0048L \approx 0.076\mu m$. The transverse extent of the pairs in the x direction is $0.17R \approx 0.27\mu m$ while that in the y direction is $0.2R \approx 0.31\mu m$ (the data not shown). The transverse distribution is mainly governed by the Gaussian form function F_1. The slight asymmetry along the x and y directions is because of the ϕ dependence of the fields appearing with the ξ^2 term through the form function F_2. The temporal distribution is dictated by the pulse envelope function g, although the particles are produced over much shorter time duration compared to the pulse duration. It is shown in Fig. 2.3. The bunch duration of e^+e^- pairs estimated by FWHM of the distribution is of the order of $1.4fs$.

2.2.2 Pulses made up of purely h-waves ($\mu = 1$)

Because of the duality between the h-wave configuration and the e-wave configuration of the counterpropagating pulses, the structure of the fields and the invariant fields and the relationship between the two remain same as that for $\mu = -1$. There is, however, interchange between the invariant electric and magnetic fields: $\epsilon^h = \eta^e$; $\eta^h = \epsilon^e$ and $|\mathbf{E}^h| = |\mathbf{H}^e|$; $|\mathbf{H}^h| = |\mathbf{E}^e|$. As a result of this interchange, ϵ^h as a function of χ is $\pi/2$ phase-shifted with respect to ϵ^e. It, therefore, has a node at $\chi = 0$ and two equally prominent antinodes on either side of $\chi = 0$ wherein pairs are mostly created. Thus the spatial distribution of the particles in the longitudinal direction is bimodal with the peaks coinciding with those of the antinodes located at $\chi = \mp 0.0164$. The peak values are slightly less than half of that for $\mu = -1$. The longitudinal extent of the pairs on both the locations is $0.0732\mu m$. The spatial distribution in the transverse direction and the temporal distribution of pairs are expectedly more or less same as those for $\mu = -1$.

2.2.3 Pulses made up of the equal mixtures of e-and h-waves ($\mu = 0$)

The resulting invariant fields Eqs. (2.9,2.10) are quite different from those of the e-wave Eqs. (2.7,2.8) or h-wave configurations - both qualitatively and quantitatively. The invariant fields are much smaller in the focal region by a factor of 2ξ. The invariant fields are significantly non-identical to the respective fields in the lab frames given by Eqs. (2.9,2.10,A.16,A.17). This can be explained by evaluating $\mathbf{C}^{e+h} = \mathbf{E}^{e+h} \times \mathbf{H}^{e+h}$. The x and y components of $\mathbf{C}^{e+h}$ are proportional to $\xi\Delta$ and hence negligibly small however, the z-component is quite significant which is given by

$$C_z^{e+h} = \frac{4E_0^2 g^2 e^{-\frac{2\xi^2}{1+4\chi^2}}}{(1+4\chi^2)^2}[1 - \frac{2\xi^2}{(1+4\chi^2)^{1/2}} \cos\psi]. \tag{2.14}$$

The above expression implies that the electric and the magnetic fields are almost orthogonal to each other in the lab frame. The parallel portion of the fields goes as ξ^2 which can also be inferred from the presence of the ξ^2 factor in the invariant $\mathcal{G}^{e+h}$ in Eq. A.15. The invariant fields, therefore, are much less compared to the fields in the lab frame. It also implies that a large amount of EM field energy flows out from the focal region. Hence this field configuration is not efficient for the pair production.

Unlike the $\mu = \pm 1$, the invariant electric field in this case does not have, in its leading order, the oscillatory term with spatial frequency $\omega z/c$ along the propagation direction Eq. 2.9. Consequently, the longitudinal distribution of pairs is much broader. However, because of the presence of this oscillatory term in the next higher order, the distribution, as shown in Fig. 2.2, has a dip in the centre and has two peaks on its either side. The extent of the effective region of pairs has increased in comparison to those of $\mu = \mp 1$ cases. FWHM of each peak is $0.0139L$. The transverse extent of the pairs in the x direction is $0.15R \approx 0.23\mu m$ while that in the y direction is $0.8R \approx 1.27\mu m$ (the data not shown). The large asymmetry in the transverse distribution is because of the strong dependence of the invariant fields on the azimuthal angle ϕ.

The interference effect of the counterpropagating beams is seen in the temporal distribution of

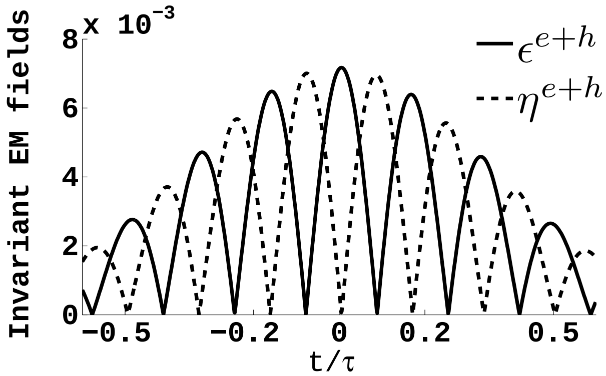

FIGURE 2.4: The invariant fields ϵ^{e+h}, and η^{e+h} for $\mu = 0$ as a function of t/τ the scaled time. $\xi = 0.1, \chi = 0.1$, and $\phi = \pi/2$. The field parameters are as those in Fig. 2.1.

the invariant fields Fig. 2.4. It has multiple maxima/minima within the pulse envelope function g. In Fig. 2.3 which presents the differential particle distribution in time, a very sharp peak of FWHM $449as$ is seen for $\mu = 0$. This implies that it is possible to generate ultrashort particle bunches using this configuration - much shorter than what can be obtained using laser pulses with $\mu = \mp 1$.

2.3 Conclusion

We have studied the particle production via Schwinger mechanism for counterpropagating focused laser beams with the parameter of asymmetry $\mu = \mp 1$, and 0. The complete features of the pair generation are explained on the basis of the structure of the electromagnetic (EM) fields and their relationship with the EM fields invariants and the reduced invariant fields in the transformed frame where both electric and magnetic fields are parallel. Analytical expressions of the resultant field distribution in both the frames are discussed which are used to pinpoint why colliding beam configurations with $\mu = \mp 1$ are particularly efficient for pair production and why that corresponding to $\mu = 0$ gives much lower number of the pairs. It has been established that the configurations with $\mu = \mp 1$ yields electric and magnetic fields which are almost parallel to each other in the focal region. This minimizes the energy flowing out of the focal region and thereby producing a maximum number of pairs. Just opposite situation arises for the configuration $\mu = 0$. In this case, the resulting electric and magnetic fields are nearly orthogonal to each other and the most of EM field energy flows out from the focal region thereby effecting less number of pairs. Though $\mu = 0$ configuration is not efficient for pair production, it offers the possibility for generating ultrashort bunches of electrons and positrons.

Chapter 3

Electron-positron pair creation by counterpropagating laser pulses:role of carrier envelope phase

A few cycle ultra-short laser pulse propagation has significant dependence on the carrier envelope phase (CEP) which is basically the phase difference between the carrier wave and the envelope of the pulse profile [42–44]. It has significant bearing on the QED processes like pair production, Compton effects etc. In fact, the determination CEP can be taken place as reported in Ref. [42] where the angular distribution of photons emitted by an electron via multiphoton Compton scattering due to an intense laser pulse has been shown. It is shown that the reported study [42] has direct dependence on CEP of the laser pulse. The effect of CEP on the momentum distribution of the produced pairs has also been extensively explored for the time dependent but spatially uniform electric field [19, 31, 70].

In this **Chapter** we study the effects of CEP on the invariant fields distributions and the corresponding differential production rates of e^+e^- pairs in spatio-temporal coordinates for the counterpropagating linear and circular polarizations e-wave focused Gaussian laser pulses. Here e-wave refers the EM wave configuration in which electric field is perpendicular to the propagation direction [10]. We consider the circularly polarized forward and backward propagating laser pulses are in the combinations of right-right and right-left in their polarization vector rotations. We see that such kinds of polarization vectors combinations result CEP dependence in the invariant fields structure for circular polarization.

This **Chapter** is organized as follows. In Sec. 3.1 we discuss the EM field configurations for linearly and circularly e-waves laser pulses. The dependence of the CEP on the energy flow from the focal volume is studied for the linear polarization. The CEP dependence on the structure of the invariant electric and magnetic fields for circularly e-polarized laser pulses is also discussed in this section for right-right and right-left configurations. The distributions of the invariant fields and the differential production rates of e^+e^- pairs are discussed in 3.2. The particle production yield for three configurations of polarizations (linear, circular right-right,circular right-left) is presented in Sec. 3.3. Finally we conclude in Sec. 3.4. The technical details of the analytical expressions for the EM field are given in **Appendix** B.

3.1 Theoretical Method

The present section is devoted for the calculation of the invariant electric and magnetic fields in the focal region for counterpropagating focused Gaussian laser pulses. We consider both linear and circular polarizations of the pulse of e-wave configuration. First we calculate for the linear polarization and second we do the calculation for the circular polarization case.

3.1.1 Structure of the EM fields due the superposition of counterpropagating linearly e-polarized focused Gaussian laser pulses

We consider the EM field structure of two linearly polarized counterpropagating focused laser pulses. In the pulsed laser EM field profile for ultra-short in time, we take the effect of CEP between the carrier wave and the envelope function. Using N-F field model [10] the expressions of the laser pulses propagating in z and $-z$ directions and having their focal region centred about the origin for the case where the pulses are made up of two e-waves are given as (detailed calculations have been shown in **Appendix** B):

$$Re\mathbf{E}^e = 2E_0 g\frac{e^{-\xi^2/(1+4\chi^2)}}{1+4\chi^2}\sin(\omega t+\tilde{\varphi})\left[\hat{\mathbf{e}}_x\left\{\cos(\omega z/c-2\psi)-\frac{2\xi^2}{(1+4\chi^2)^{1/2}}\sin^2\phi\cos(\omega z/c-3\psi)\right\}\right.$$
$$\left.+\hat{\mathbf{e}}_y\frac{\xi^2}{(1+4\chi^2)^{1/2}}\sin 2\phi\cos(\omega z/c-3\psi)\right], \tag{3.1}$$

and

$$ReH^e \approx -2E_0 g \frac{e^{-\xi^2/(1+4\chi^2)}}{1+4\chi^2}\Bigg[\cos(\omega t+\tilde{\varphi})\Bigg(\hat{\mathbf{e}}_x \frac{\xi^2}{(1+4\chi^2)^{1/2}}\sin 2\phi \sin(\omega z/c - 3\psi) - \hat{\mathbf{e}}_y \left\{\sin(\omega z/c - 2\psi) - \frac{2\xi^2}{(1+4\chi^2)^{1/2}}\sin^2\phi \sin(\omega z/c - 3\psi)\right\}\Bigg) + 4\xi\Delta \frac{\sin(\omega t+\tilde{\varphi})}{(1+4\chi^2)^{1/2}}\sin\phi \sin(\omega z/c - 3\psi)\hat{\mathbf{e}}_z\Bigg]. \tag{3.2}$$

Here E_0 is the normalized (by Schwinger field E_S) peak electric field strength of the laser beams, ω is the corresponding central frequency, λ is the wavelength, Δ is the focusing or spatial inhomogeneity parameter, R is the focusing radius, L is the Rayleigh length; and $\xi = \rho/R, \chi = z/L, \rho = \sqrt{x^2+y^2}$, $\exp(i\phi) = (x+iy)/\rho$, $\Delta = c/\omega R = \lambda/2\pi R$, $L = R/\Delta$, and $\exp(i\psi) = (1+2i\chi)/\sqrt{1+4\chi^2}$. The superscript e refers to the focused EM field in e-wave mode [10]. In Eqs. (3.1-3.2), g is the temporal envelope function to account for the finite pulse width and $\tilde{\varphi}$ is the corresponding CEP. Though there can be various functional forms of g consistent with the condition that $g(0) = 1$ and g should decrease very fast at the periphery of the focal pulse for $|\varphi| \gg \omega\tau$ [10, 15], we take $g = \exp(-4(t^2/\tau^2 + z^2/c^2\tau^2))$ for all the calculations presented here [65]. Here $\varphi = \omega(t - z/c)$ is defined as the instantaneous phase of the laser EM wave. The magnitude of the resultant EM field given in Eqs. (3.1,3.2) in the focal region ($|\chi| < 1, \xi < 1$) can be approximated as

$$|ReE^e| \approx 2E_0 g \frac{e^{-\xi^2/(1+4\chi^2)}}{1+4\chi^2}|\sin(\omega t+\tilde{\varphi})|\,|\cos(\omega z/c - 2\psi)|\left[1 - \frac{2\xi^2}{(1+4\chi^2)^{1/2}}\sin^2\phi\right], \tag{3.3}$$

and

$$|ReH^e| \approx 2E_0 g \frac{e^{-\xi^2/(1+4\chi^2)}}{1+4\chi^2}|\cos(\omega t+\tilde{\varphi})|\,|\sin(\omega z/c - 2\psi)|\left[1 - \frac{2\xi^2}{(1+4\chi^2)^{1/2}}\sin^2\phi\right]. \tag{3.4}$$

It shows that the magnitude of the electric and magnetic fields for linearly e-polarized counterpropagating laser pulses has standing wave structure in which the temporal oscillation has additive CEP dependence and the longitudinal oscillation has a phase term $\psi(=\arctan(2\chi))$ due to the complex Gaussian beam functions F_1 and F_2. Since the pair creation process is solely governed by the invariant EM fields so it is worthwhile to calculate the EM field invariants. The expression for the Lorentz invariants $\mathcal{F}^e$, $\mathcal{G}^e$ of the EM field given by Eqs. (3.1-3.2) is

$$\mathcal{F}^e = \frac{1}{2}(ReE^{e2} - ReH^{e2}) \approx 2E_0^2 g^2 \frac{e^{-2\xi^2/(1+4\chi^2)}}{(1+4\chi^2)^2}\left\{\sin^2(\omega t+\tilde{\varphi}) - \sin^2(\omega z/c - 2\psi)\right\}\left[1 - \frac{4\xi^2}{(1+4\chi^2)^{1/2}}\sin^2\phi\right], \tag{3.5}$$

and

$$\mathcal{G}^e = Re\mathbf{E}^e \cdot Re\mathbf{H}^e \approx -4E_0^2 g^2 \xi^2 \chi \frac{e^{-2\xi^2/(1+4\chi^2)}}{(1+4\chi^2)^{5/2}} \sin 2(\omega t + \tilde{\varphi}) \sin 2\phi \left[1 + 3\xi^2\right]. \tag{3.6}$$

For e-wave beam configuration the reduced invariant electric and magnetic fields are defined as [1, 65]:

$$\epsilon^e = \sqrt{\sqrt{\mathcal{F}^{e2} + \mathcal{G}^{e2}} + \mathcal{F}^e}, \quad \eta^e = \sqrt{\sqrt{\mathcal{F}^{e2} + \mathcal{G}^{e2}} - \mathcal{F}^e}. \tag{3.7}$$

The value of $\mathcal{G}^e$ is negligibly small in the focal region. It is maximum in the peripheral region $\xi = 0.75$, $\chi = \pm 0.25$ for $t = 0.001\tau$, $\phi = \pi/4$, and $\tilde{\varphi} = \pi/2$. Still this maximum value is 0.01 times less than that of $\mathcal{F}^e$ at the space-time position. In this approximation where $\mathcal{G}^e$ can be neglected, the sign of $\mathcal{F}^e$ (which is given by whether $\sin^2(\omega t + \tilde{\varphi}) - \sin^2(\omega z/c - 2\psi)$ is positive or negative) gives two non-trivial situations. If $\sin^2(\omega t + \tilde{\varphi}) > \sin^2(\omega z/c - 2\psi)$, then $\mathcal{F}^e$ is positive and consequently ϵ^e is non zero and η^e is zero. This gives rise to what is known as electric regime [71]:

$$\epsilon^e \approx 2E_0 g \frac{e^{-\xi^2/(1+4\chi^2)}}{1+4\chi^2} \left\{\sin^2(\omega t + \tilde{\varphi}) - \sin^2(\omega z/c - 2\psi)\right\}^{1/2} \left[1 - \frac{2\xi^2}{(1+4\chi^2)^{1/2}} \sin^2\phi\right], \text{ and } \eta^e \approx 0. \tag{3.8}$$

Similarly one has magnetic regime ($\mathcal{F}^e$ is negative) for the case when $\sin^2(\omega t + \tilde{\varphi}) < \sin^2(\omega z/c - 2\psi)$ [71]. Here ϵ^e vanishes and η^e is non zero:

$$\epsilon^e \approx 0, \text{ and } \eta^e \approx 2E_0 g \frac{e^{-\xi^2/(1+4\chi^2)}}{1+4\chi^2} \left\{\sin^2(\omega z/c - 2\psi) - \sin^2(\omega t + \tilde{\varphi})\right\}^{1/2} \left[1 - \frac{2\xi^2}{(1+4\chi^2)^{1/2}} \sin^2\phi\right]. \tag{3.9}$$

Recalling that ϵ^e and η^e are the electric and magnetic fields strengths in the frame where they are parallel, it can be easily seen that expressions of the electric and magnetic fields in both the frames are not identical as seen in the Eqs. (3.3,3.8, 3.9, 3.4). Since electric and magnetic fields in this case are not parallel, there will be flow of energy from the focal region governed by the Poynting vector ($\mathbf{S}^e$). The x, y, and z components of $\mathbf{S}^e$ are given as

$$S_x^e \approx 16E_0^2 g^2 \xi^3 \Delta \frac{e^{-2\xi^2/(1+4\chi^2)}}{(1+4\chi^2)^3} \sin^2(\omega t + \tilde{\varphi}) \sin^2\phi \cos\phi \sin 2(\omega z/c - 3\psi), \tag{3.10}$$

$$\begin{aligned} S_y^e \approx -16E_0^2 g^2 \xi \Delta \frac{e^{-2\xi^2/(1+4\chi^2)}}{(1+4\chi^2)^{5/2}} \sin^2(\omega t + \tilde{\varphi}) \sin\phi \sin(\omega z/c - 3\psi) \Big[& \cos 2(\omega z/c - 2\psi) \\ & - \frac{2\xi^2}{(1+4\chi^2)^{1/2}} \sin^2\phi \cos(\omega z/c - 3\psi)\Big], \end{aligned} \tag{3.11}$$

and

$$S^e_z \approx -E_0^2 g^2 \frac{e^{-2\xi^2/(1+4\chi^2)}}{(1+4\chi^2)^2} \sin 2(\omega t + \tilde{\varphi}) \left[\sin 2(\omega z/c - 2\psi) - \frac{4\xi^2}{(1+4\chi^2)^{1/2}} \cos^2\phi \sin(2\omega z/c - 5\psi) \right]. \tag{3.12}$$

In Eqs. (3.10,3.11,3.12), the Cartesian components of $\mathbf{S}^e$ show that the energy flow in x and y directions is much smaller compared to the z-direction. The oscillatory nature of S^e_z leads to instantaneous energy flow whereas the average energy flow is zero.

For e-linearly polarized counterpropagating laser pulses (e-LPCLP) beam discussed above, an additional control over the pair production mechanism can be achieved by tuning CEP with respect to the dynamic phase φ of the laser pulses. In particular, if $\sin^2(\omega t + \tilde{\varphi}) < \sin^2(\omega z/c - 2\psi)$ then EM field energy will remain confined within this region as a standing wave without any loss due to e^+e^- pair production.

3.1.2 Circular polarization with CEP dependence in invariant fields for the counterpropagating focused Gaussian laser pulses

In this section we discuss the CEP dependence on the resultant field configuration in both the frames. We consider the EM field structure in lab frame and in the Lorentz transformed frame for the counterpropagating circularly e-polarized laser pulses propagating in $+z$ (forward propagation) and $-z$ (backward propagation) directions using N-F field model [10]. We consider the two counterpropagating laser pulses in the following combinations: First both the forward and backward beams are right circularly polarized and second the forward beam is right circularly polarized and backward beam is left circularly polarized. We see that the former one gives spatially localized field distribution whereas the later one gives the temporally localized fields with CEP dependent terms in the leading order.

3.1.2.1 Structure of the EM field for circularly right-right combination in the counterpropagating configuration

The expression of the EM fields strength due to the superposition of counterpropagating circularly e-polarized laser pulses of same state of rotation of the polarization vectors (we assume both are right circularly polarized) is given as (detailed derivation is given in **Appendix** B)

$$|Re\mathbf{E}^e| \approx \frac{2E_0 g e^{-\xi^2/1+4\chi^2}}{(1+4\chi^2)}|\cos(\omega z/c - 2\psi)|\Bigg[1 - \frac{\xi^2}{\cos(\omega z/c - 2\psi)(1+4\chi^2)^{1/2}}\Big\{\cos(\omega z/c - 3\psi) + \cos 2(\omega t + \tilde{\varphi})\cos(3\psi - \omega z/c - 2\phi)\Big\} + O(\xi^4)\Bigg], \tag{3.13}$$

and

$$|Re\mathbf{H}^e| \approx \frac{2E_0 g e^{-\xi^2/1+4\chi^2}}{(1+4\chi^2)}|\sin(\omega z/c - 2\psi)|\Bigg[1 - \frac{\xi^2}{\sin(\omega z/c - 2\psi)(1+4\chi^2)^{1/2}}\Big\{\sin(\omega z/c - 3\psi) + \cos 2(\omega t + \tilde{\varphi})\sin(3\psi - \omega z/c - 2\phi)\Big\} + O(\xi^4)\Bigg]. \tag{3.14}$$

Eqs. (3.13,3.14) show that in the leading order it contains oscillatory term in longitudinal coordinate whereas CEP dependence is not seen. The leading order expression of the invariant electric and magnetic fields is

$$\epsilon^e \approx \frac{2E_0 g e^{-\xi^2/1+4\chi^2}}{(1+4\chi^2)}|\cos(\omega z/c - 2\psi)|, \;\text{ and }\; \eta^e \approx \frac{2E_0 g e^{-\xi^2/1+4\chi^2}}{(1+4\chi^2)}|\sin(\omega z/c - 2\psi)|.$$

It reflects that such combination of the polarization vectors for counterpropagating laser pulses has no CEP dependence at the field magnitude level and also in the invariant fields expression.

3.1.2.2 Structure of the EM field for circularly right-left combination in the counter-propagating configuration

We use the focused EM field structure and derive the structure of the resultant electric and magnetic fields due to the superposition of right circularly e-wave in $+z$-direction and left circularly e-wave propagating in $-z$-direction. The expression of the real part of the electric and magnetic fields in the above mentioned configuration is given by (detailed derivation is given in **Appendix** B)

$$Re\mathbf{E}^e = 2E_0 g\Bigg[\Big\{\sin(\omega t + \tilde{\varphi})Re[F_1 e^{i\omega z/c}] - \sin(\omega t + \tilde{\varphi} - 2\phi)Re[F_2 e^{i\omega z/c}]\Big\}\hat{\mathbf{e}}_x - \Big\{\sin(\omega t + \tilde{\varphi})Im[F_1 e^{i\omega z/c}] + \sin(\omega t + \tilde{\varphi} - 2\phi)Im[F_2 e^{i\omega z/c}]\Big\}\hat{\mathbf{e}}_y\Bigg], \tag{3.15}$$

and

$$ReH^e = 2E_0 g\Big[\Big\{\cos(\omega t+\tilde{\varphi})Re[F_1 e^{i\omega z/c}] + \cos(\omega t+\tilde{\varphi}-2\phi)Re[F_2 e^{i\omega z/c}]\Big\}\hat{\mathbf{e}}_x - \Big\{\cos(\omega t+\tilde{\varphi})Im[F_1 e^{i\omega z/c}] - \cos(\omega t+\tilde{\varphi}-2\phi)Im[F_2 e^{i\omega z/c}]\Big\}\hat{\mathbf{e}}_y + 2\Delta\sin(\omega t+\tilde{\varphi}-\phi)Re[e^{i\omega z/c}\frac{\partial F_1}{\partial \xi}]\Big]. \tag{3.16}$$

We use the expression of $Re\mathbf{E}^e$ and $Re\mathbf{H}^e$ given in Eqs. (3.15,3.16) to calculate the expression of the Lorentz invariants $\mathcal{F}^e$ and $\mathcal{G}^e$ as

$$\mathcal{F}^e \approx -2E_0^2 g^2 \frac{e^{-2\xi^2/1+4\chi^2}}{(1+4\chi^2)^2}\Big[\Big(1-\frac{2\xi^2\cos\psi}{(1+4\chi^2)^{1/2}}\Big)\cos 2(\omega t+\tilde{\varphi}) - \frac{2\xi^2\cos 2\phi}{(1+4\chi^2)^{1/2}}\cos(2\omega z/c-5\psi)\Big], \tag{3.17}$$

and

$$\mathcal{G}^e \approx 2E_0^2 g^2 \frac{e^{-2\xi^2/1+4\chi^2}}{(1+4\chi^2)^2}\Big[\Big(1-\frac{2\xi^2\cos\psi}{(1+4\chi^2)^{1/2}}\Big)\sin 2(\omega t+\tilde{\varphi}) - \frac{2\xi^2\sin 2\phi}{(1+4\chi^2)^{1/2}}\cos(2\omega z/c-5\psi)\Big]. \tag{3.18}$$

Here the approximate expression of F_1 and F_2, the complex Gaussian form functions of focused laser beam stated in **Appendix** B in normalized spatial coordinates χ and ξ is used. The approximate expression of the Lorentz invariants $\mathcal{F}^e$ and $\mathcal{G}^e$ as given in Eqs. (3.17,3.18) shows oscillatory behaviour in time. The value of $\mathcal{F}^e$ is positive in negative half cycle of its oscillation period. Such feature is translated into the invariant electric and magnetic fields expression which are given as

$$\epsilon^e \approx 2E_0 g\frac{e^{-\xi^2/1+4\chi^2}}{(1+4\chi^2)}\Big(1-\frac{2\xi^2\cos\psi}{(1+4\chi^2)^{1/2}}\Big)^{1/2}|\sin(\omega t+\tilde{\varphi})|\Big[1-\frac{\xi^2\cos(2\omega z/c-5\psi)}{(1+4\chi^2)^{1/2}}\frac{\sin(2\phi-\omega t-\tilde{\varphi})}{\sin(\omega t+\tilde{\varphi})} + O(\xi^4)\Big], \tag{3.19}$$

and

$$\eta^e \approx 2E_0 g\frac{e^{-\xi^2/1+4\chi^2}}{(1+4\chi^2)}\Big(1-\frac{2\xi^2\cos\psi}{(1+4\chi^2)^{1/2}}\Big)^{1/2}|\cos(\omega t+\tilde{\varphi})|\Big[1-\frac{\xi^2\cos(2\omega z/c-5\psi)}{(1+4\chi^2)^{1/2}}\frac{\cos(2\phi-\omega t-\tilde{\varphi})}{\cos(\omega t+\tilde{\varphi})} + O(\xi^4)\Big]. \tag{3.20}$$

It shows the oscillating structure of invariant electric and magnetic fields in the leading order in time and the oscillating phase ωt has a additive $\tilde{\varphi}$ term which reflects the direct CEP dependence. Hence the combination of the polarization vectors' rotation plays an important role in the structure of the resultant field due to the superposition of two counterpropagating circularly e-polarized laser pulses.

3.2 Results and discussions

Here we discuss the spatio-temporal distribution of the invariant fields (ϵ^e and η^e) and the differential pair production rates for counterpropagating focused Gaussian laser pulses as derived in Sec. 3.1.1. First the distribution of fields is discussed in Sec. 3.2.1-3.2.2 and later the pair production rates are presented in Sec. 3.2.3. The space-time variables are scaled by the laser parameters such as: time is scaled by the pulse duration τ; longitudinal variable z is scaled by the Rayleigh length L; and the transverse variables x, y are by the focusing radius R of the laser beam.

3.2.1 Field distribution: Linear polarization

The spatio-temporal distribution of ϵ^e for e-LPCLP for which the analytical expression is given in Sec. 3.1.1 is discussed here for different values of CEP. Fig. 3.1(a) shows the temporal distributions of ϵ^e for CEP $\tilde{\varphi} = 0$, $\pi/4$, and $\pi/2$ at the focal point. The invariant field shows oscillatory behaviour inside the pulse envelope function g due to the interference between the counterpropagating pulses in time. For $\tilde{\varphi} = \pi/2$ the invariant electric field has a central peak (located at $t = 0$) accompanied by other small peaks symmetrically placed on the either side of the central peak in time. As the value of $\tilde{\varphi}$ is reduced to $\pi/4$, the temporal profile of ϵ^e shifts to the right, i.e. towards the leading part of the laser pulse. Moreover the profile becomes asymmetric in time. The peaks in the leading part of the laser pulse are smaller and the ones in the trailing part are large compared to those for $\tilde{\varphi} = \pi/2$. For $\tilde{\varphi} = 0$, the temporal profile is again symmetric. However, it has a minimum at the centre of the laser pulse and has two major maxima on either side of the centre. The reduced magnetic field η^e vanishes completely in this case (data not shown) as $\mathcal{G}^e$ is identically equal to zero and $\mathcal{F}^e$ is positive for $z = 0$. For $z \neq 0$ and $x = y = 0$ (where $\mathcal{G}^e = 0$), depending on the sign of $\mathcal{F}^e$, we have a mesh like structure in the zt-plane where some regions belong to the electric regime and other to the magnetic regime. In Fig. 3.1(b-d), the contour of ϵ^e is shown in zt-plane for $\tilde{\varphi} = \pi/2, 3\pi/4,$ and π. It shows that the peak positions are getting shifted in temporal axis with CEP whereas in the z-axis, no changes

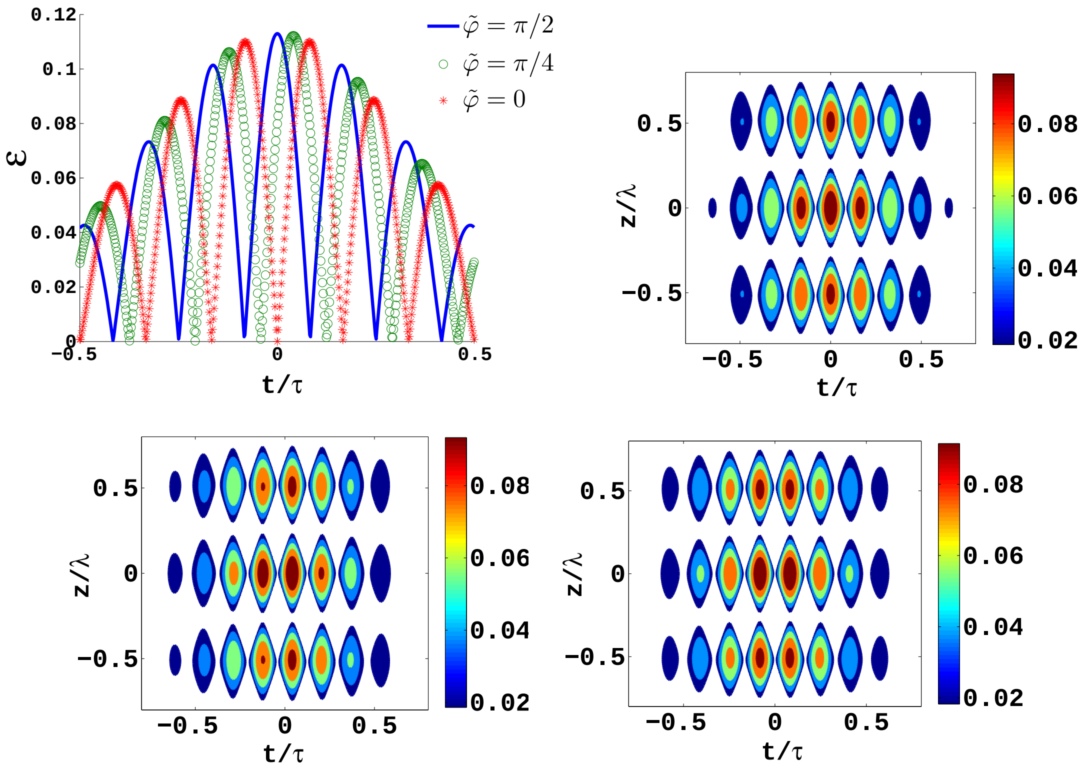

FIGURE 3.1: The temporal evolution of ϵ^e and its contour plots in zt-plane (in scaled variables) for different values of CEP, showing the locations of the peak field positions for linearly polarized counterpropagating laser pulses. Top left panel shows the temporal evolution of ϵ^e for $\tilde{\varphi} = 0$, $\pi/4$, and $\pi/2$. From top right to bottom right panels the contour plots for $\tilde{\varphi} = \pi/2$, $3\pi/4$, and π in the zt-plane for $x = y = 0$ are shown. The laser EM field parameters are $E_0 = 0.0565$, $\Delta = 0.1$, $\tau = 10fs$, and $\lambda = 1\mu m$. The adjacent colour bars are showing the normalized field strength at the field peak positions.

have been observed in the peak positions. It is obvious from the simplified expression of ϵ^e in Eq. 3.8. Here due to the shift in the peak positions, the maximum peak height also gets reduced because of the Gaussian pulse envelope function g. It ensures that the control over the CEP is important in the context of the process which depends on the peak field strength.

It shows that the maximum electric field is located at $z = 0$, and due to the interference between the counterpropagating beams in z and t, the reduced electric field is distributed like localized spikes in zt-plane. The z-distribution or the location of the peaks along the z-axis is not affected by the variation of $\tilde{\varphi}$ and it shows one central peak $z = 0$ and two non-central peaks located symmetrically about $z = 0$ in the leading order. Hence because of the three peaks in the leading order in z-distribution of ϵ^e, it results trimodal distribution of differential pairs which we see in Sec. 3.2.3. The temporal location of the peak positions is very sensitive to CEP. For $\tilde{\varphi} = \pi/2$, the contour of the reduced field ϵ^e is shown in the Fig. 3.1(b) which describes the locations of the maximum field intensities in the zt-plane. Here at the central position ($z = t = 0$) the field distribution possesses maximum intensity. Fig. 3.1(c) shows the same for $\tilde{\varphi} = 3\pi/4$ where it reflects the shift in the temporal axis. Significant changes have observed in the contour ϵ^e in zt-plane for $\tilde{\varphi} = \pi$ in which the peak field intensity in the central position is zero and it gets splitted into two peaks located symmetrically about $t = 0$ in the time axis. It causes bimodal distribution of differential pair production rates in time, which we discuss in Sec. 3.2.3.

From the analytical expression of the simplified reduced electric field ϵ^e in Eq. 3.8 , we discuss the locations of the peak positions and the corresponding shifts with CEP as presented in Fig. 3.1(a). We consider at the focus ($z = 0$). From Eq. 3.8, we have the location of the central peak position as $\omega t + \tilde{\varphi} = \pm\pi/2$, which ends up with two values such as $\omega t_+ = \pi/2 - \tilde{\varphi}$ and $\omega t_- = -\pi/2 - \tilde{\varphi}$. Here $+(-)$ sign in the subscript denotes the temporal position corresponding positive (negative) time axis. So the difference between the locations of the central peaks in positive and negative time axis is given by $\omega(t_+ - t_-) = \pi$ or $(t_+ - t_-) = \pi/\omega$. It concludes that the separation between temporal positions in central peaks are independent on the values of CEP. Some special cases are as follows: (1) For $\tilde{\varphi} = \pi/2$, we have central peak at $\omega t_{central} = 0$ along with two side peaks at $\omega t_+ = \pi$ and $\omega t_- = -\pi$. (2) For $\tilde{\varphi} = \pi/4$, we have $\omega t_+ = \pi/4$ and $\omega t_- = -3\pi/4$. (3)Similarly for $\tilde{\varphi} = 0$, we have $\omega t_+ = \pi/2$ and $\omega t_- = -\pi/2$. So the above analysis and the distribution of reduced electric field in the Fig. 3.1 coincide and it tells that the central maxima are changing, depending on the values of CEP. Such features also contribute in the relative shift in the location of the particle distribution in time which we discuss in the next section.

Fig. 3.2(a-b) shows the invariant electric field distributions in xt-plane for $\tilde{\varphi} = \pi/2$ and π. It is seen that the x-distribution follows the Gaussian profile as we have seen in the leading expression of ϵ^e (it varies as $\exp(-\xi^2/(1+4\chi^2))$) in Eq. 3.8. The temporal profile has oscillating structure. It is also seen that the x-distribution remains same whereas shifts in the location of the intensity peak value have been observed in t-distribution. So the peak field strength gets reduced for $\tilde{\varphi} = \pi$ configuration as seen in the colour bar in Fig. 3.2(b). But the yt-distribution presents slightly different dependence on CEP. In the Fig. 3.2(c-d), the invariant electric field distributions in the yt-plane has been shown for the same of values of $\tilde{\varphi}$ as in the xt-distribution. The temporal distributions are same but in y axis, it shows two extra peaks apart from the central maxima which is also obvious from the Eq. 3.8. All such invariant electric field distributions control the rate of the particle distributions with space-time coordinates for different values of $\tilde{\varphi}$ which we see in Sec. 3.2.3.

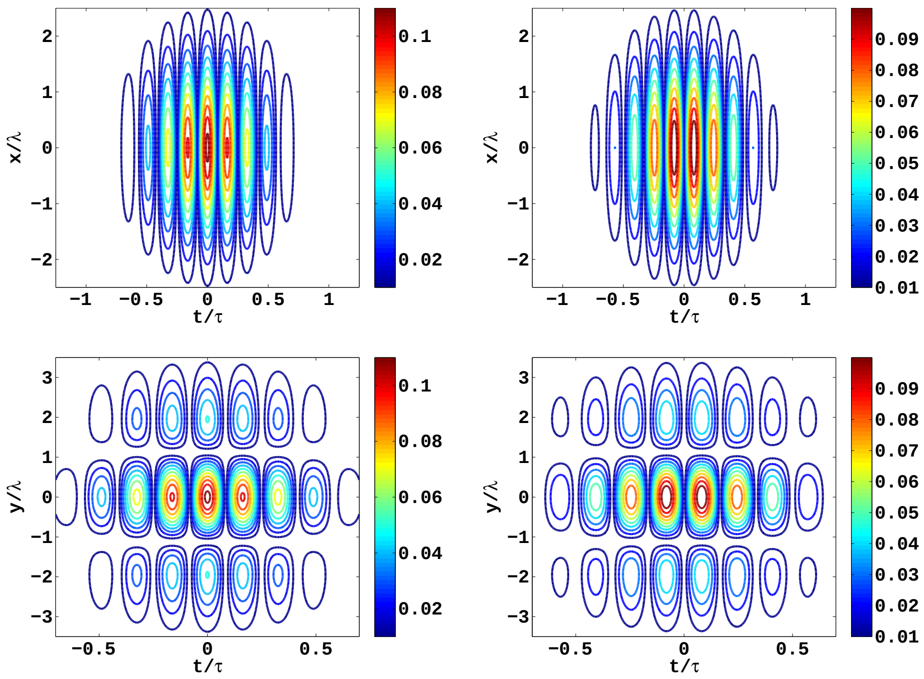

FIGURE 3.2: Contour plots of the ϵ^e in xt-and yt-planes in scaled variables for CEP $\tilde{\varphi} = \pi/2$ and π, showing the locations of the peak field positions for linearly e-polarized counterpropagating laser pulses. Top left panel shows for $\tilde{\varphi} = \pi/2$ and in the top right it is for $\tilde{\varphi} = \pi$ in the xt-plane for $y = z = 0$. In the bottom it shows same in the yt-plane for $x = z = 0$ are given. The laser EM field parameters are $E_0 = 0.0565$, $\Delta = 0.1$, $\tau = 10fs$, and $\lambda = 1\mu m$. The adjacent colour bars are showing the normalized field strength at the field peak positions.

3.2.2 Field distribution: Circular polarization

We have seen in Sec. 3.1.2.1 that the two right circularly counterpropagating laser pulses, the resultant expressions of the electric and magnetic fields in both the frames do not have CEP dependence in leading order. Therefore we present electric and magnetic fields due to the superposition of right circularly forward propagating laser pulse with the left circularly backward propagating pulse in consideration as theoretically derived in Sec. 3.1.2.2. The analytical expression of ϵ^e and η^e shows that the CEP dependence comes in the temporal oscillations whereas other variables do not include any CEP dependence. So we present the invariant electric and magnetic fields distributions in time as a function of CEP.

Temporal distributions of the reduced invariant electric and magnetic fields profiles for different values of CEP are shown in Fig. 3.3. Both upper and lower panels show oscillating field profiles in time. The locations of the antinodal positions change with CEP and consequently their peak values get change. It shows that the maximum electric field occurs at $t = 0$ for $\tilde{\varphi} = \pi/2$ and the magnetic field possesses minimum value. But for $\tilde{\varphi} = 0$ the magnetic field reaches maximum and electric field vanishes at $t = 0$. These two values of CEP give the maximum and minimum values of the invariant electric and magnetic fields as shown in the left panel of upper and lower figure in Fig. 3.3. Such kind of temporal fields profiles get translated into the temporal distribution of the particle-antiparticle production rates. Other features in the oscillating field profiles such as the formation of the two peaks in the central region instead of the single peak, asymmetric locations of the peaks about $t = 0$, and the corresponding asymmetry in their peak heights are shown in the right panel of upper and lower figures in Fig. 3.3. Such field distribution manifest in the distribution of particle production rates in time which we see in Fig. 3.5.

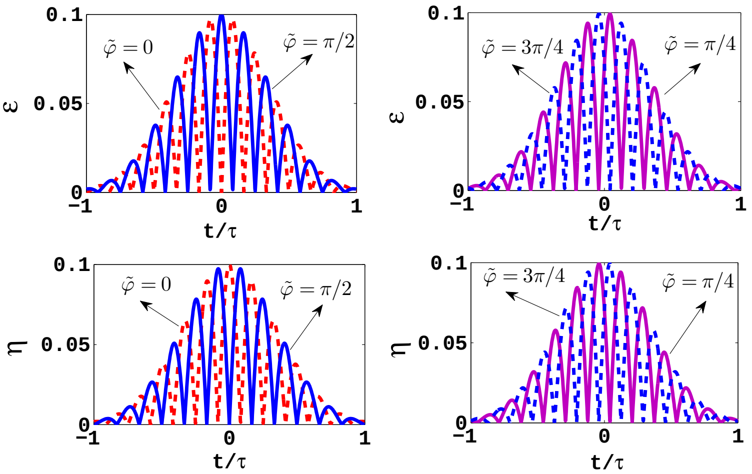

FIGURE 3.3: Temporal distributions of invariant electric and magnetic fields for counterpropagating circularly e-polarized laser pulses in right-left combination of the polarization vectors as function of CEP. The upper panel shows invariant electric field distributions for $\tilde{\varphi} = 0, \pi/2$ in the left and $\pi/4, 3\pi/4$ in the right. The lower panel shows the same for invariant magnetic field. The laser EM field parameters are $E_0 = 0.0565$, $\Delta = 0.1$, $\tau = 10fs$, and $\lambda = 1\mu m$.

3.2.3 Particle distribution: Linear polarization

Here we show the distribution of pair production rates in space-time coordinates by applying Nikishov formula [3]. It tells that the average number of e^+e^- pairs produced in the presence of constant electric and magnetic fields per unit volume and per unit time is given by

$$w_{e^-e^+} = \frac{dN_{e^-e^+}}{dVdt} = \frac{e^2E_S^2}{4\pi^2\hbar^2c}\epsilon^e\eta^e \coth(\frac{\pi\eta^e}{\epsilon^e})\exp(-\frac{\pi}{\epsilon^e}). \tag{3.21}$$

Using Eq. 3.21, we calculate the differential pairs numerically and present the distributions in space-time coordinates (such as x/R, y/R, $\chi = z/L$, and in t/τ) for e-LPCLP mode for different values of CEP. First we discuss the x-distribution of the differential pairs for two values of $\tilde{\varphi}$ ($\pi/2$ and π) which are the two optimum values of $\tilde{\varphi}$ for producing maximum and minimum rates of the differential pairs and the average production yields. Fig. 3.4(a) displays the differential pairs distributions in x/R for $\tilde{\varphi} = \pi/2$ and π. It forms like a Gaussian profile which is obvious as the reduced electric field distribution exhibits such profiles (Fig. 3.2(a-b)). The contour plot of ϵ^e in normalized xt-plane shows Gaussian nature along the x axis and oscillatory nature in the time axis. Because of the extended electric field distribution in x axis due to the prefactor $\exp(-\xi^2/(1+4\chi^2))$ term in ϵ^e given in Eq. 3.8, the rate of pair production gets broadened.

The differential particle distribution in normalized y-axis is shown in Fig. 3.4 b. The distribution profile is Gaussian and $\tilde{\varphi} = \pi/2$ leads to the maximum differential pair production rate in y. Such pair distribution can be explained from the contour plot of ϵ^e as shown in Fig. 3.2(c). Here apart from the Gaussian factor $\exp(-\xi^2/(1+4\chi^2))$ in the analytical expression of ϵ^e, see Eq. 3.8, it exhibits quadratic variation in y in the leading order. So the y-distribution of invariant electric field ϵ^e has nodal structure, seen in Fig. 3.2(c-d). The central region contributes in pair production as it possesses maximum peak field strength whereas the other lobes do not have sufficient field strength to produce pairs. So effectively the y-distribution gets localized and we have non-identical particle distribution in x and y axes. Such localization of the invariant electric field also produces higher production rate in y than x axis.

Fig. 3.4(c) shows the variation $dN_{e^+e^-}/d\chi$ with χ for $\tilde{\varphi} = \pi/2$ and π. The distribution rate shows trimodal profile for both the value of CEP. For $\tilde{\varphi} = \pi/2$, the maximum production rate occurs at $\chi = 0$ and the other two peaks are located symmetrically about the central position $\chi = 0$. The separation between the non-central peaks is insensitive with the CEP values. Although for $\tilde{\varphi} = \pi$, the profile of the particle production rate falls under the same profile with $\tilde{\varphi} = \pi/2$ but the non central peaks exceed from $\tilde{\varphi} = \pi/2$ case. Such kind of particle distribution has resemblance to the invariant electric field distribution as seen in Fig. 3.1(a-b)-Fig. 3.1(d). Here $dN_{e^+e^-}/d\chi$ shows very spiky nature because of the localization of ϵ^e in χ.

Fig. 3.4(d) shows $dN_{e^+e^-}/d(t/\tau)$ in time for $\tilde{\varphi} = 0,\ \pi/4$, and $\pi/2$. It shows CEP sensitivity in the differential pair distribution. The maximum rate of pair production occurs at $\tilde{\varphi} = \pi/2$ and minimum at $\tilde{\varphi} = 0$.

The shift in the central peak results the reduction of the peak height due to the temporal pulse envelope function g. So the temporal distribution of the pairs gets reduced for CEP other than $\pi/2$. We have observed such asymmetrical distribution for $\tilde{\varphi} = \pi/4$. This can be explained by calculating the locations of the reduced electric field maxima. In the central zone we have two points which are located at $t_+ = \pi/4\omega$ and $t_- = -3\pi/\omega$. These two values correspond to

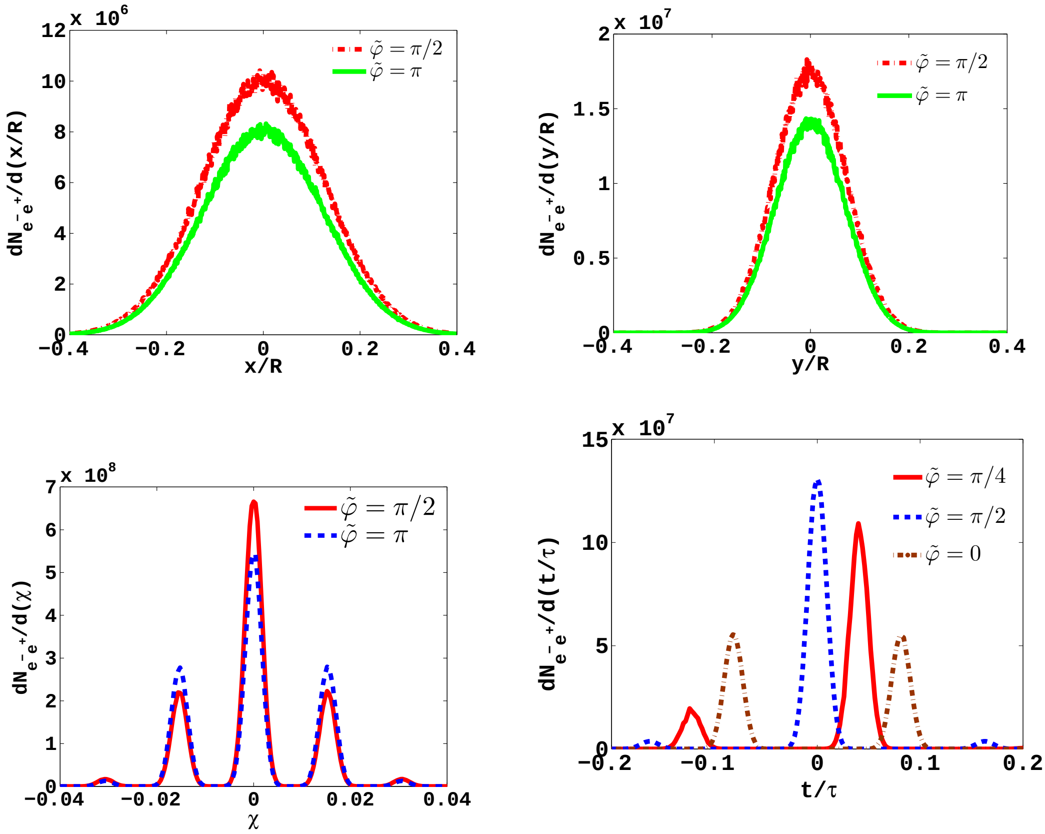

FIGURE 3.4: The differential e^+e^- pair production rates in scaled space-time variables for different values of CEP $\tilde{\varphi}$ for the counterpropagating linearly polarized laser pulses. The upper panel shows the distribution in transverse coordinates x and y and the lower panel shows in longitudinal variable χ and time. The laser EM field parameters are $E_0 = 0.0565$, $\Delta = 0.1$, $\tau = 10fs$, and $\lambda = 1\mu m$.

the reduction of the peak electric field strength differently which causes an asymmetric particle distribution. Because of the CEP, the internal field oscillation advances towards the leading edge of the pulse envelope and peak position of the field is being shifted. So at such positions due to the pulse envelope function, the peak field strength gets reduced and the temporal rate of the pair generation gets lowered. The other observed feature of $dN_{e^+e^-}/d(t/\tau)$ in t/τ is that it shows very sharp distribution and the corresponding width of the profile at FWHM is $200as$ for a laser profile of pulse duration $10fs$. Such kind of sharp bunch generation is important for the generation of e^- or e^+ beams having small temporal spread, high γ value etc. by applying a suitable magnetic field.

3.2.4 Particle distribution: Circular polarization

Here we discuss about the differential particle production rates in time for the counterpropagating circularly e-polarized focused Gaussian laser pulses. We consider the forward propagating pulse is right circularly polarized and backward propagating pulse is right circularly polarized for the first case and left circularly polarized pulse for the second case. It is seen that in the resultant expression of the invariant electric and magnetic fields for the right-right combination in the polarization vector rotation is devoid of temporal oscillation in the leading order and it shows oscillations in longitudinal coordinate. It is also seen that the leading order spatiotemporal dependence is independent of CEP. So as a result the differential particle production in time is insensitive with CEP and it follows the overall smooth variation due to the pulse envelope function g.

Distribution of the particles in spatiotemporal coordinates for the circularly e-polarized right-left combination in the counterpropagating configuration

Differential particle distribution in time is shown in Fig. 3.5 for circularly e-polarized focused Gaussian laser pulses in right-left combination for the counterpropagating fields. Fig. 3.5 shows that the production rates are sharp and localized within the interval of time smaller than the laser pulse duration. It has some other feature such as unimodal particle distribution gets changed to bimodal one depending on CEP. For $\tilde{\varphi} = \pi/2$, the production rate is occurred at $t = 0$ which gives maximum peak value and displays symmetric unimodal structure. But by changing the value of CEP, the profile becomes bimodal one having symmetric and asymmetric both in peak values and the occurrence of the peaks about $t = 0$. The separation of the peaks in bimodal profile for a particular value of CEP is fixed and it holds for other values of CEP. We have calculated the FWHM of the distribution profiles as $220as$ which shows the generation of very short particle bunch for circular polarization in counterpropagating configuration. For $\tilde{\varphi} \neq \pi/2$, the particle production rate in time changes its location and it is accompanied with the reduction of peak height. So the proper control over CEP is required to get maximum rate of particle production in time.

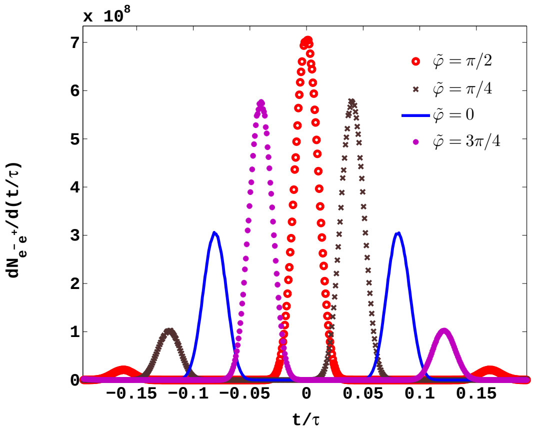

FIGURE 3.5: Differential e^+e^- pair production rates in time for $\tilde{\varphi} = 0, \pi/4, \pi/2$, and $3\pi/4$ for the counterpropagating circularly e-polarized focused Gaussian laser pulses in right-left combination in polarization vectors rotation. The laser EM field parameters are $E_0 = 0.0565$, $\Delta = 0.1$, $\tau = 10fs$, and $\lambda = 1\mu m$.

3.3 Particle production yield: linear and circular polarizations

The average numbers of created pairs $N_{e^+e^-}$ for different values of CEP for the counterpropagating laser pulses are shown in Table 3.1. The data shows for both linear and circular polarizations laser pulses in e-wave configuration. For circular polarization case, we have separately shown for right-right and right-left combinations of their polarization vector rotations in column two and three. Although the data shows less sensitivity with CEP on average pair number generation relative to the differential particle production rate. However it shows that the average particle number increases (slightly) with CEP varied from 0 to $\pi/2$ and then reduces for linear polarization and circular polarization in right-left combination. The right-right combination in circular polarization, the average particle numbers are almost insensitive with CEP.

3.4 Conclusion

To conclude, the present studies examined the electron-position pair production process via Schwinger mechanism for the counterpropagating focused Gaussian ultrashort a few cycle ($\tau = 10fs$ with laser radiation wavelength $\lambda = 1\mu m$ which corresponds three oscillation) laser pulses. It includes linear and circular polarizations in e-wave configuration. For the circular

$\tilde{\varphi}$	$N_{e^+e^-}$(linear)	$N_{e^+e^-}$(cir right-right)	$N_{e^+e^-}$(cir right-left)
0	2.517×10^6	1.980×10^7	1.547×10^7
$\frac{\pi}{8}$	2.605×10^6	1.992×10^7	1.577×10^7
$\frac{\pi}{4}$	2.856×10^6	1.976×10^7	1.729×10^7
$\frac{3\pi}{8}$	3.051×10^6	2.011×10^7	1.876×10^7
$\frac{\pi}{2}$	3.157×10^6	1.994×10^7	1.919×10^7
$\frac{3\pi}{4}$	2.826×10^6	1.984×10^7	1.734×10^7
$\frac{5\pi}{6}$	2.651×10^6	1.983×10^7	1.611×10^7

TABLE 3.1: The average number of created particles $N_{e^+e^-}$ as a function of CEP $\tilde{\varphi}$ for counterpropagating linear and circular polarizations in e-wave mode. The column two and three are for the circular polarization in right-right and right-left combinations in the rotation of the polarization vector. Here $E_0 = 0.0565$, $\Delta = 0.1$, $\tau = 10fs$, and $\lambda = 1\mu m$.

polarization we considered both right and left handedness of the rotation of the polarization vector and the effect of the carrier envelope phase (CEP) dependence also considered.

First it has been shown for the linear polarization where CEP dependence came into the leading order of the invariant field distribution. The focal region composed of electric and magnetic regimes where the Lorentz invariant $\mathcal{F}^e$ is either positive or negative. It is seen oscillatory structure in both longitudinal coordinate and in time. Such kind of field distribution made the differential particle production process more localized and hence very short particle bunch can be produced in longitudinal coordinate and in time. Here we have calculated that for CEP $= \pi/2$, the resultant field configuration produces maximum production rate in time with width at FWHM is $200as$.

Second, it has been studied for the circular polarization case of counterpropagating configuration. The combinations of right-right and right-left in the polarization vector rotations for the forward and backward propagating laser pulses have been studied. The resultant field distribution for the right-right combination showed oscillatory field profile in longitudinal coordinate which does not include any CEP dependence. But for the right-left combination generates oscillation in time and in the leading order it depended on CEP. Consequently two cases have been seen, one in which particle production rate is insensitive with CEP and two in which particle production rate is very sensitive with CEP. Former one produces spatially localized particle distribution whereas the later one produces temporally localized particle production.

One basic observation is that for the circularly e-polarized counterpropagating laser pulses, the mixture of right-right in the rotation of the polarization vector gives localized invariant electric and magnetic fields in longitudinal coordinate irrespective of the value of CEP in the leading order whereas the temporal profile follows the pulse envelope function. Therefore such field profile gives rise to localized particle bunch formation in the longitudinal axis. On the other hand when the superposition is taken between right-left combination between the two pulses in polarization vector *i.e.,* the forward beam is right circularly polarized and backward beam is left circularly polarized (the opposite configuration also give same result), it is seen that the invariant electric and magnetic fields depend on the fast oscillation in time with CEP under the envelope function. It has a temporally localized invariant fields which causes the differential pair distribution short.

So the proper control over CEP is essential for the ultrashort laser pulses in counterpropagating configuration in particle-antiparticle production mechanism.

Chapter 4

Phase control of Schwinger pair production by colliding laser pulses

So far we have studied the spatiotemporal distribution of the created pairs by the counterpropagating laser pulses at focus where it is assumed the colliding pulses are in phase configuration. However, it has been shown recently in Ref. [66] that for a focused linearly polarized standing wave the invariant electric field distribution, and hence also pair production, are sensitive to the carrier envelope phase (CEP) $\tilde{\varphi}$. Here we study the spatio-temporal distribution of e^+e^- pairs created via the Schwinger mechanism at a focal region of the colliding laser pulses described by the Narozhny-Fofanov model [10], assuming that the pulses are in addition mutually phase shifted. As we demonstrate, the phase shift Ψ considerably affects the longitudinal spatial (here, z-) coordinate and time distributions of the resulting EM field, especially for ultrashort (few cycle) laser pulses. Furthermore, we study the dependence of the invariant field structure and of the distribution of the created pairs on polarization, relative sense of rotation (for circular polarization), and CEP of the counterpropagating pulses.

The **Chapter** is organized as follows: in Sec. 4.1 we briefly discuss the basic theory: the Schwinger formula for average pair production and the structure of the invariant electric and magnetic fields of the coherently superposed counterpropagating focused laser pulses. Next we present the differential pair production rates in spatiotemporal coordinates and explanation of their features in terms of the invariant electric field distribution in Sec. 4.2, finally concluding in Sec. 4.3. A technically useful simplification of the envelope of counterpropagating pulses is discussed in **Appendix** C.

4.1 Theoretical background and field model

Assuming the validity of a locally constant field approximation, the average number of created pairs per unit time and volume can be calculated using the Nikishov formula [3, 72]:

$$w_{e^-e^+} = \frac{d^2 N_{e^-e^+}}{dVdt} = \frac{e^2 E_S^2}{4\pi^2\hbar^2 c}\epsilon\eta \coth\left(\frac{\pi\eta}{\epsilon}\right)\exp\left(-\frac{\pi}{\epsilon}\right), \tag{4.1}$$

where e is the magnitude of the electron charge, and $\epsilon,\ \eta = \sqrt{\sqrt{\mathcal{F}^2+\mathcal{G}^2} \pm \mathcal{F}}$ [with $\mathcal{F} = \frac{1}{2}\left(\mathbf{E}^2 - \mathbf{H}^2\right)$ and $\mathcal{G} = \mathbf{E}\cdot\mathbf{H}$] are the normalized (by E_S) invariant electric and magnetic field strengths, i.e. the magnitudes of the electric and magnetic field strengths in a reference frame where they are locally either zero or parallel. Eq. (4.1) is valid in a locally constant field approximation based on an assumption that the characteristic length and time scales of the e^+e^- pair production process (the Compton length $\hbar/m_e c$ and time $\hbar/m_e c^2$ scales) are much smaller than the carrier wavelength ($\lambda \approx 1\mu$m) and the period ($\lambda/c \approx 3$fs) of the laser field, respectively [72]. In particular, pair production is negligible if ϵ is small or vanishing in a focal region, while in the opposite case of nearly vanishing η Eq. (4.1) reduces to

$$w_{e^-e^+} = \frac{d^2 N_{e^-e^+}}{dVdt} \approx \frac{e^2 E_S^2}{4\pi^3\hbar^2 c}\epsilon^2 \exp\left(-\frac{\pi}{\epsilon}\right). \tag{4.2}$$

As we will see later on, these special cases are realized for the magnetic and electric regimes in the focal region for collision of linearly polarized laser pulses. Hence we use Eq. (4.2) for presenting the numerical results of differential particle production rates in spatiotemporal coordinates for linearly polarized laser pulses and Eq. (4.1) otherwise. To obtain a temporal particle distribution we integrate $w_{e^+e^-}$ over the spatial coordinates, and to obtain the longitudinal spatial distribution of particle production we integrate the production rate $w_{e^+e^-}$ over the transverse spatial coordinates and time. The actual distribution of the invariant fields in a focal region of colliding pulses strongly depends on their polarization and is discussed below. In all numerical calculations, we use the exact expressions for the EM fields and assume for definiteness the amplitude $E_0 = 0.0565$, carrier wavelength $\lambda = 1\mu m$, focusing parameter $\Delta = 0.1$, and pulse duration $\tau = 10fs$ for each of the counterpropagating pulses. However, to easier interpret the results, in the rest of the section we also derive the approximate analytical expressions for field invariants near the focus.

Let us start with a field configuration of linearly polarized counterpropagating focused laser pulses based on the Narozhny-Fofanov field model [10]. We assume the normalized (by E_S) electric fields of the pulses propagating in a forward ($+z$) and backward ($-z$) directions of the form [15]

$$\mathbf{E}_f = iE_0 e^{-i\omega(t-z/c)-i\tilde{\varphi}} g \Big[\hat{\mathbf{e}}_x (F_1 - F_2 \cos 2\phi) - \hat{\mathbf{e}}_y F_2 \sin 2\phi \Big], \tag{4.3}$$

and

$$\mathbf{E}_b = iE_0 e^{-i\omega(t+z/c)-i\tilde{\varphi}-i\Psi} g \Big[\hat{\mathbf{e}}_x (F_1^* - F_2^* \cos 2\phi) - \hat{\mathbf{e}}_y F_2^* \sin 2\phi \Big], \tag{4.4}$$

respectively, where E_0 is the normalized (by E_S) peak electric field strength of the laser pulse; $\omega = 2\pi c/\lambda$ is the central frequency of the pulse; λ is the laser carrier wavelength; F_1, F_2 are the Gaussian-like functions of the form [10]

$$F_1 = \frac{1}{(1+2i\chi)^2}\left(1 - \frac{\xi^2}{1+2i\chi}\right)\exp\left(-\frac{\xi^2}{1+2i\chi}\right), \quad F_2 = -\frac{\xi^2}{(1+2i\chi)^3}\exp\left(-\frac{\xi^2}{1+2i\chi}\right),$$

F_1^* and F_2^* are their complex conjugates; $\xi = \rho/R$ is the normalized radial variable with $\rho = \sqrt{x^2+y^2}$ at the transverse Cartesian spatial coordinates x, y; R is the focal radius; $\phi = \arctan(y/x)$ is the azimuthal angle; $\chi = z/L$ is the normalized longitudinal coordinate with $L = R/\Delta$ being the Rayleigh length for a focusing aperture parameter $\Delta = c/\omega R$. The envelope function g accounts for temporal finiteness of the laser pulses. In this paper we take $g = \exp(-4t^2/\tau^2 - 4z^2/c^2\tau^2)$ [65, 66] (a detailed explanation of our method of introducing g is given in **Appendix** C). Finally, $\tilde{\varphi}$ and Ψ are CEP and the phase shift of the backward propagating pulse, respectively.

The corresponding expressions for the normalized magnetic field of the forward and backward propagating pulses are [15]

$$\mathbf{H}_f = iE_0 e^{-i\omega(t-z/c)-i\tilde{\varphi}} g \left[\left(1 - i\Delta^2 \frac{\partial}{\partial\chi}\right) \Big\{ \hat{\mathbf{e}}_x F_2 \sin 2\phi - \hat{\mathbf{e}}_y (F_1 - F_2 \cos 2\phi) \Big\} + 2i\Delta \sin\phi \frac{\partial F_1}{\partial \xi} \hat{\mathbf{e}}_z \right], \tag{4.5}$$

and

$$\mathbf{H}_b = -iE_0 e^{-i\omega(t+z/c)-i\tilde{\varphi}-i\Psi} g \left[\left(1 + i\Delta^2 \frac{\partial}{\partial\chi}\right) \Big\{ \hat{\mathbf{e}}_x F_2^* \sin 2\phi - \hat{\mathbf{e}}_y (F_1^* - F_2^* \cos 2\phi) \Big\} + 2i\Delta \sin\phi \frac{\partial F_1^*}{\partial \xi} \hat{\mathbf{e}}_z \right]. \tag{4.6}$$

Following the procedure of Ref. [66], the expressions for the Lorentz invariants of the resultant EM field $\mathbf{E} = \mathbf{E}_f + \mathbf{E}_b$, $\mathbf{H} = \mathbf{H}_f + \mathbf{H}_b$ of the superposed counterpropagating pulses can be derived,

$$\mathcal{F} = \frac{1}{2}\Big(Re\mathbf{E}^2 - Re\mathbf{H}^2\Big) \approx \frac{2E_0^2 g^2 e^{-\frac{2\xi^2}{1+4\chi^2}}}{(1+4\chi^2)^2}\Big[\sin^2(\omega t + \tilde{\varphi} + \Psi/2) - \sin^2(\omega z/c + \Psi/2)\Big], \tag{4.7}$$

and

$$\mathcal{G} = Re\mathbf{E} \cdot Re\mathbf{H}^e \approx \frac{2E_0^2 g^2 \xi^2 e^{-\frac{2\xi^2}{1+4\chi^2}}}{(1+4\chi^2)^{5/2}} \sin(2\phi) \sin[2(\omega t + \tilde{\varphi} + \Psi/2)] \sin[2(\omega z/c + \Psi/2)], \tag{4.8}$$

where we retain only the leading order terms in Δ, ξ, and χ, as justified in the focal region in a weak focusing limit. Since $\mathcal{G} = O\left(\xi^2\right)$ is negligibly small there, one of the invariant fields (depending on the sign of $\mathcal{F}$) is vanishingly small. For $\mathcal{F} > 0$ we have so-called electric regime [71]

$$\epsilon_{elec} \approx \frac{2E_0 g e^{-\frac{\xi^2}{1+4\chi^2}}}{(1+4\chi^2)} \left[\sin^2(\omega t + \tilde{\varphi} + \Psi/2) - \sin^2(\omega z/c + \Psi/2)\right]^{1/2}, \quad \text{and} \quad \eta_{elec} \approx 0, \tag{4.9}$$

whereas, for a magnetic regime $\mathcal{F} < 0$ [71]

$$\epsilon_{mag} \approx 0, \quad \text{and} \quad \eta_{mag} \approx \frac{2E_0 g e^{-\frac{\xi^2}{1+4\chi^2}}}{(1+4\chi^2)} \left[\sin^2(\omega z/c + \Psi/2) - \sin^2(\omega t + \tilde{\varphi} + \Psi/2)\right]^{1/2}. \tag{4.10}$$

Clearly, pairs are created solely during an electric regime, and the phases Ψ and $\tilde{\varphi}$ control toggling between the electric and magnetic regimes at given point and time, thereby controlling also the pair production. As is seen from the obtained approximate expressions (and in fact is also true for the exact ones), it is enough to restrict phases by $0 \leq \tilde{\varphi} < \pi$ and $0 \leq \Psi < 2\pi$.

Spatiotemporal distributions of the invariant field ϵ^e for few representative values $\Psi = 0,\ \pi/2,\ \pi$ and $\tilde{\varphi} = 0,\ \pi/2$ are presented in Fig. 4.1, where the rhombic structure corresponds to the aforementioned separation into the alternating electric (color) and magnetic (dark) regimes. It is clear from the figure, as well as from the above equations, that the maxima are shifted with respect to the origin $t = z = 0$, and that their shift is determined by the phases. If the maxima are remote from the origin (which is at the center of the envelope) then their magnitudes are reduced, in this way they are also indirectly controlled by the phases. The figure illustrates a variety of possible opportunities: the maxima can be located symmetrically about the origin, with either one [see Fig. 4.1(d)] or a gap [Figs. 4.1(a,c,f)] seating at the origin (in the latter case there can be either four or two maxima closest to it: if there are two then they can be lined up along either axis); or off centered [like in Figs. 4.1(b,e)] – in the latter case the magnitudes of the maxima are lined up according to their distance from the origin. Qualitatively, the pair production rate behaves the same way [see Eq. (4.1) or (4.2)], hence, as we will see below, this variety of opportunities precisely corresponds to peculiarities of distribution of created pairs that we observe in our calculations.

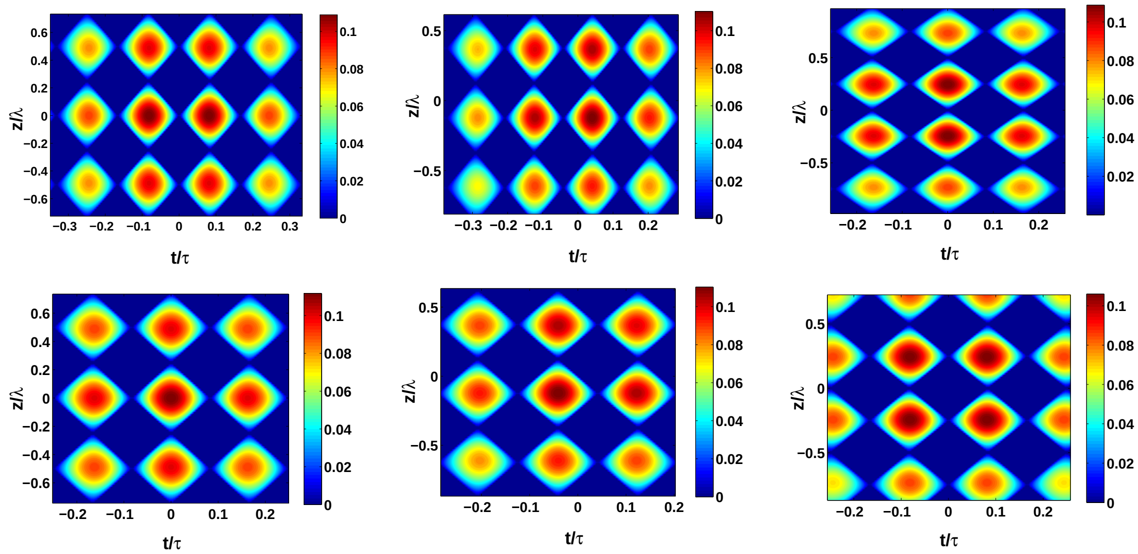

FIGURE 4.1: Spatiotemporal distributions of the invariant electric field $\epsilon(x = 0, y = 0, z, t)$ for linearly e-polarized Gaussian laser pulses colliding with different values of the phases $\tilde{\varphi}$ and Ψ. The laser parameters are $E_0 = 0.0565$, $\Delta = 0.1$, $\tau = 10fs$, and $\lambda = 1\mu m$.

Now consider circularly polarized forward and backward propagating laser pulses with a relative phase difference Ψ. We follow closely the steps discussed in Ref. [65, 66]. For a forward propagating (along $+z$) laser pulse, the electric and magnetic fields are given by

$$\mathbf{E}_f = iE_0 e^{-i\omega(t-z/c)-i\tilde{\varphi}} g\Big[F_1(\hat{\mathbf{e}}_x \pm i\hat{\mathbf{e}}_y) - F_2 e^{\pm 2i\phi}(\hat{\mathbf{e}}_x \mp i\hat{\mathbf{e}}_y)\Big], \tag{4.11}$$

and

$$\mathbf{H}_f = \pm E_0 e^{-i\omega(t-z/c)-i\tilde{\varphi}} g\left[\left(1 - i\Delta^2\frac{\partial}{\partial\chi}\right)\Big[F_1(\hat{\mathbf{e}}_x \pm i\hat{\mathbf{e}}_y) + F_2 e^{\pm 2i\phi}(\hat{\mathbf{e}}_x \mp i\hat{\mathbf{e}}_y)\Big] + 2i\Delta e^{\pm i\phi}\frac{\partial F_1}{\partial\xi}\hat{\mathbf{e}}_z\right], \tag{4.12}$$

respectively. Here the signs correspond to the right (+)- and left (−)- handed rotation of the electric field vector with respect to propagation direction. For a backward propagating (along $-z$) laser pulse with a relative phase shift Ψ the expressions for the electric and magnetic fields are given by

$$\mathbf{E}_b = iE_0 e^{-i\omega(t+z/c)-i\tilde{\varphi}-i\Psi} g\Big[F_1^*(\hat{\mathbf{e}}_x \pm i\hat{\mathbf{e}}_y) - F_2^* e^{\mp 2i\phi}(\hat{\mathbf{e}}_x \mp i\hat{\mathbf{e}}_y)\Big], \tag{4.13}$$

and

$$\mathbf{H}_b = \mp E_0 e^{-i\omega(t+z/c)-i\tilde{\varphi}-i\Psi} g\left[\left(1 + i\Delta^2\frac{\partial}{\partial\chi}\right)\Big[F_1^*(\hat{\mathbf{e}}_x \pm i\hat{\mathbf{e}}_y) + F_2^* e^{\mp 2i\phi}(\hat{\mathbf{e}}_x \mp i\hat{\mathbf{e}}_y)\Big] + 2i\Delta e^{\mp i\phi}\frac{\partial F_1^*}{\partial\xi}\hat{\mathbf{e}}_z\right]. \tag{4.14}$$

For a pair of counterpropagating circularly polarized pulses, we have two alternatives: either both pulses have the same polarization (for definiteness right handed, hereafter referred to as the RR configuration), or opposite polarizations (for definiteness we assume that the forward propagating pulse has the right handed polarization and the backward propagating one has the left handed polarization, hereafter referred to as the RL configuration).

For the RR configuration the Lorentz invariants near the focus ($\xi, \chi \ll 1$) are given by

$$\mathcal{F}_{RR} \approx \frac{2E_0^2 g^2 e^{-\frac{2\xi^2}{1+4\chi^2}}}{(1+4\chi^2)^2} \cos\left[2(\omega z/c + \Psi/2)\right], \quad \mathcal{G}_{RR} \approx \frac{2E_0^2 g^2 e^{-\frac{2\xi^2}{1+4\chi^2}}}{(1+4\chi^2)^2} \sin\left[2(\omega z/c + \Psi/2)\right], \tag{4.15}$$

so that the invariant electric and magnetic fields are

$$\epsilon_{RR} \approx \frac{2E_0 g e^{-\frac{\xi^2}{1+4\chi^2}}}{(1+4\chi^2)} |\cos(\omega z/c + \Psi/2)|, \quad \eta_{RR} \approx \frac{2E_0 g e^{-\frac{\xi^2}{1+4\chi^2}}}{(1+4\chi^2)} |\sin(\omega z/c + \Psi/2)|. \tag{4.16}$$

One can see that, unlike the case of linearly polarized configuration, now their phases are time-independent and are solely controlled by single phase Ψ. The overall smooth temporal dependence on a time scale τ remains only due to the pulse envelope function g. The oscillatory dependence on longitudinal coordinate χ is shown in Fig. 4.2. It is clear that as Ψ is growing from zero, the highest central spike becomes off-centered, and eventually at $\Psi = \pi$ is replaced with two spikes of equal height located symmetrically about the center.

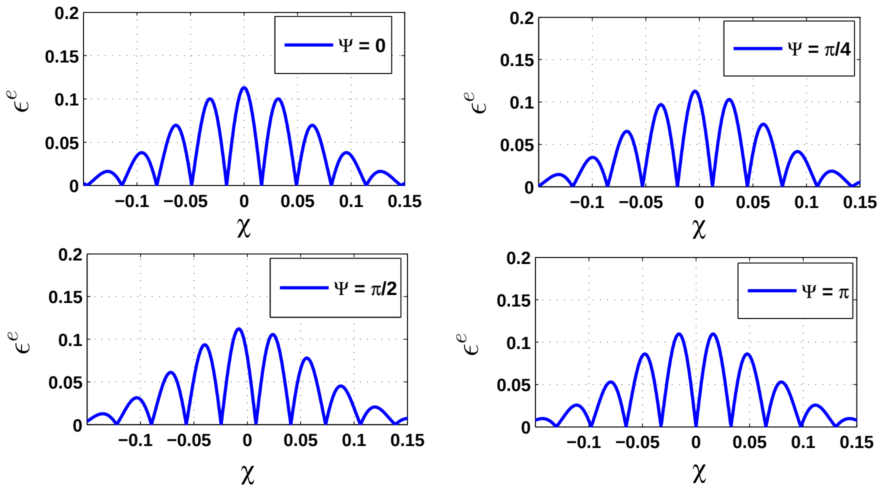

FIGURE 4.2: Dependence of the invariant electric field ϵ at $\xi = \phi = 0$ on the longitudinal coordinate χ for counterpropagating circularly e-polarized focused Gaussian laser pulses in RR configuration with relative phases for $\Psi = 0, \pi/4, \pi/2$, and π. Laser parameters are the same as in Fig. 4.1.

Proceeding the same way for the RL configuration, we obtain the leading order expressions of the Lorentz invariants

$$\mathcal{F}_{RL} \approx -2E_0^2 g^2 \frac{e^{-\frac{2\xi^2}{1+4\chi^2}}}{(1+4\chi^2)^2} \cos\left[2(\omega t + \tilde{\varphi} + \Psi/2)\right], \quad \mathcal{G}_{RL} \approx 2E_0^2 g^2 \frac{e^{-\frac{2\xi^2}{1+4\chi^2}}}{(1+4\chi^2)^2} \sin\left[2(\omega t + \tilde{\varphi} + \Psi/2)\right], \tag{4.17}$$

and the invariant electric and magnetic fields read as follows:

$$\epsilon_{RL} \approx 2E_0 g \frac{e^{-\frac{\xi^2}{1+4\chi^2}}}{(1+4\chi^2)} |\sin(\omega t + \tilde{\varphi} + \Psi/2)|, \quad \eta_{RL} \approx 2E_0 g \frac{e^{-\frac{\xi^2}{1+4\chi^2}}}{(1+4\chi^2)} |\cos(\omega t + \tilde{\varphi} + \Psi/2)|. \tag{4.18}$$

In contrast to the RR case here their oscillations are purely temporal and depend on both Ψ and $\tilde{\varphi}$, see Fig. 4.3. As it shows, variation of the phases, like in previous case, results in a shift of the main maximum from the center. Namely, it is located at the origin $t = 0$ for $\tilde{\varphi} = 0$ at $\Psi = \pi$, whereas for $\tilde{\varphi} = \pi/2$ at $\Psi = 0$. As we will see in the next section, off-centering of the main maximum results in passing from unimodal to bimodal profile of created pairs.

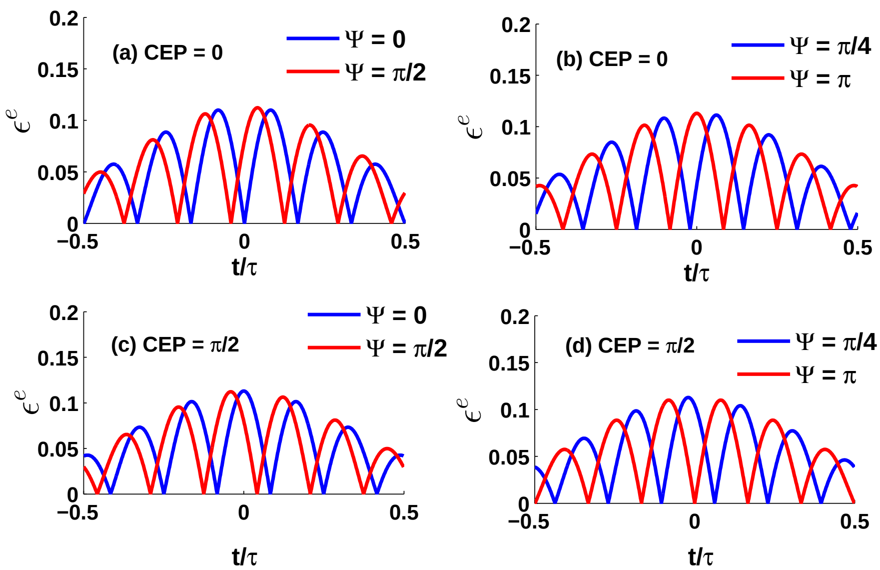

FIGURE 4.3: Time evolution of the invariant electric field ϵ at $\xi = \phi = \chi = 0$ for counter-propagating circularly e-polarized focused Gaussian laser pulses in RL configuration with CEP $\tilde{\varphi} = 0,\ \pi/2$ and with relative phase $\Psi = \ 0,\ \pi/4,\ \pi/2$, and π. Laser parameters are the same as in Fig. 4.1.

4.2 Results and discussion

According to Eq. (4.1), the pair production rate depends exponentially and monotonously on the spatiotemporal distribution of the invariant electric field in the focal region, which in turn is controlled by the phase shifts Ψ and $\tilde{\varphi}$. Hence, we present and discuss the results of calculation of differential particle production rate for various polarizations of the collided pulses and in dependence on the values of Ψ and $\tilde{\varphi}$. The main goal is to demonstrate how its features can be natively understood in terms of the underlying invariant EM field spatiotemporal structure.

4.2.1 Differential pair production rate (linear polarization)

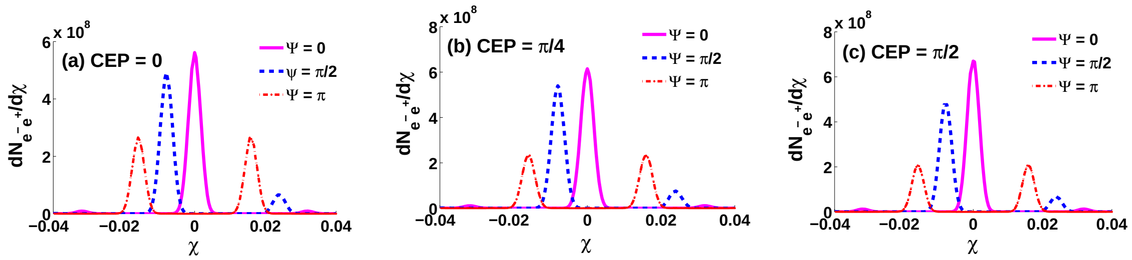

FIGURE 4.4: Spatial distributions in longitudinal coordinate χ of particles created by colliding linearly polarized laser pulses with $\Psi = 0,\ \pi/2,\ \pi$ and $\tilde{\varphi} = 0, \pi/4, \pi/2$. Laser parameters are the same as in Fig. 4.1.

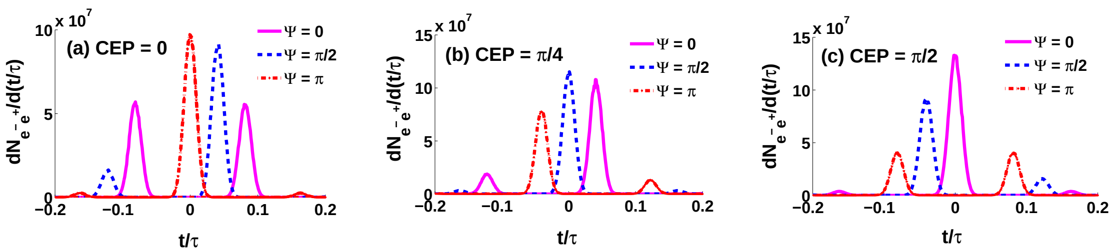

FIGURE 4.5: Temporal distributions of particles created by colliding linearly polarized laser pulses with $\Psi = 0,\ \pi/2,\ \pi$ and $\tilde{\varphi} = 0, \pi/4, \pi/2$. Laser parameters are the same as in Fig. 4.1.

Let us first discuss pair production in the case of linearly polarized colliding pulses. The differential particle distributions in longitudinal z-coordinate, calculated by means of Eqs. (4.2) – (4.6) for the values 0, $\pi/2$, π of relative phase Ψ and for CEP $\tilde{\varphi} = 0, \pi/4, \pi/2$, are shown in Fig. 4.4. The distributions possess a spiky structure, with the peaks positions sensitive to Ψ but independent of $\tilde{\varphi}$. This feature is obvious from the form of the simplified expression (4.9) of the invariant ϵ in electric regime. Furthermore, the production rate is maximal for $\Psi = 0$ and $\tilde{\varphi} = \pi/2$. As Ψ varies, the peaks are shifted from the focus center (as is the case e.g., for $\Psi = \pi/2$

or π), hence the distribution becomes asymmetric (changes from unimodal to bimodal) and the production rate is reduced. For $\Psi = \pi$ the bimodal distribution becomes symmetric. In contrast to the position, the separation of the peaks is merely independent of phase shifts (remains about $\pi\Delta^2 = 0.0314$ in dimensionless units used at the figure). The same is approximately true also for the peak widths. It is seen that for the adopted values of parameters pair production results the generation of narrow (FWHM = $0.0636\mu m$) particle-antiparticle bunches localized in longitudinal direction.

Similar features are observed also in a temporal distribution (see Fig. 4.5), where, however, the distribution profiles (peak heights as well as their locations) are sensitive to both phase shifts. In all the cases shown, in agreement with Eq. (4.9), the temporal distribution is unimodal and maximal for $\tilde{\varphi}+\Psi/2 \approx \pi/2$ and bimodal symmetric for $\tilde{\varphi}+\Psi/2 \approx 0$ or π. The peaks FWHM width is here as narrow as 200as. As expected from Fig. 4.1, the most prolific production rate is observed in Fig. 4.5(c) for $\tilde{\varphi} = \pi/2$ and $\Psi = 0$, *i.e.,* for an in-phase configuration of the counterpropagating beams.

4.2.2 Differential pair production rate (circular polarization)

For colliding circularly e-polarized laser pulses it has been observed earlier [66] that the structure of the invariant electric and magnetic fields and the pair production rate depend on their relative handedness. In particular, in RR configuration the invariant fields and the differential particle production rates do not reveal any CEP dependence. When the counterpropagating pulses are in-phase, a broad unimodal temporal particle distribution is produced. On the other hand, the colliding pulses in RL configuration produce particle bunches localized in time and with notable CEP dependence. It is, therefore, natural to consider these two cases separately.

4.2.2.1 Particle distribution for the circularly e-polarized colliding pulses in RR configuration

For RR configuration, since the invariant fields trivially depend on time and are independent on $\tilde{\varphi}$ [see Eq. (4.16) and note that the same is true exactly], it is enough to present the spatial distribution of created pairs only in dependence on Ψ, see Fig. 4.6. The maximal production rate is achieved with $\Psi = 0$, in this case the distribution looks unimodal and symmetric. The minimal production rate corresponds to a symmetric bimodal distribution at $\Psi = \pi$, while for the intermediate values of Ψ the distribution is bimodal but asymmetric. The FWHM width (about $0.0764\mu m$) of the peaks, as well as separation between them ($\lambda/2 = 0.5\mu m$), are both

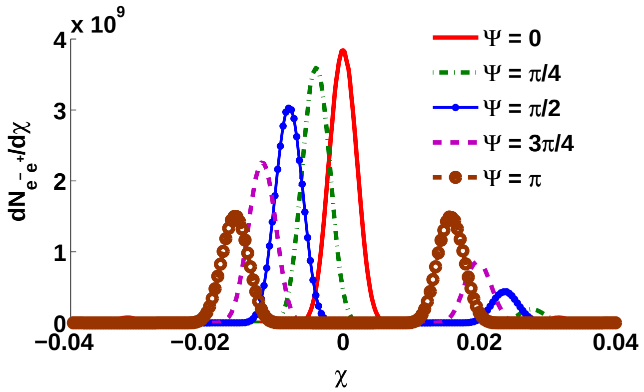

FIGURE 4.6: Spatial longitudinal distributions of e^+e^- pairs created in RR configuration for $\Psi = 0,\ \pi/4,\ \pi/2,\ 3\pi/4,\ \pi$. The laser parameters are same as in Fig. 4.1.

insensitive to the phase Ψ. All these results are in obvious agreement with our above discussion of the invariant field structure [see Eq. (4.16) and Fig. 4.2].

4.2.2.2 Particle distribution for the circularly e-polarized colliding pulses in RL configuration

For RL configuration, in contrast, the invariant fields trivially depend on position, but are sensitive to both phase shifts, hence it is enough to present only temporal evolution of the production rate, but in dependence on both phase shifts, see Fig. 4.7. As in previous cases, at variation of

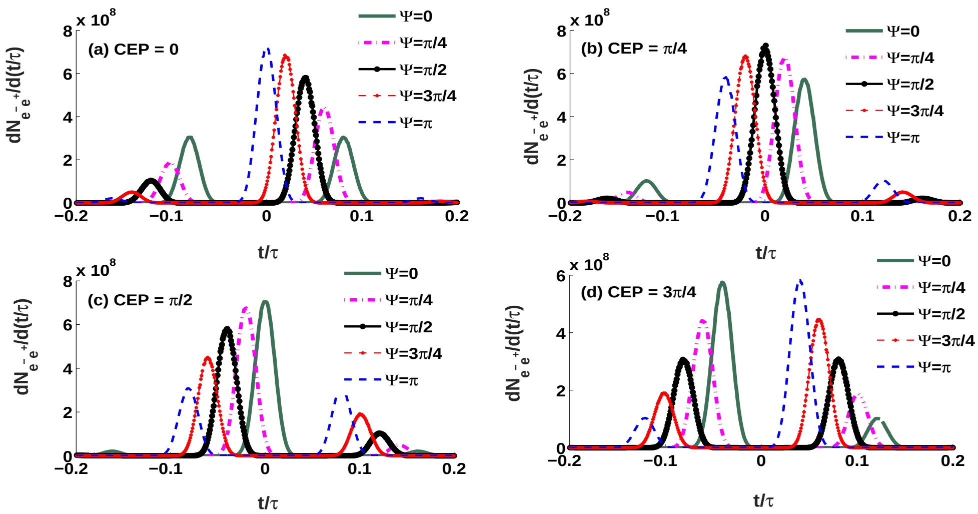

FIGURE 4.7: Evolution of the e^+e^- pair production rate in RL configuration for $\tilde{\varphi} = 0,\ \pi/4,\ \pi/2,\ 3\pi/4$ and for $\Psi = 0,\ \pi/4,\ \pi/2,\ 3\pi/4,\ \pi$. Laser parameters are the same as in Fig. 4.1.

phases the distribution profile changes from unimodal through asymmetric bimodal to symmetric bimodal. In agreement with Eq. (4.18), the particular form of the distribution depends solely on the combination $\tilde{\varphi} + \Psi/2$, with maximal and minimal production rates when it is close to $\pi/2$ and to zero or π, respectively. The FWHM width of the generated particle bunches is about $220as$, much shorter than laser pulse duration $10fs$. As before, it is insensitive to both phases $\tilde{\varphi}$ and Ψ, as well as to separation between the peaks when the profiles are bimodal, which is about $1.6fs$.

By comparing the figures of this section, we conclude that for the same values of parameters the circularly polarized RR-configuration with $\Psi = 0$ maximizes the total number of created pairs. Namely this configuration was discussed in greater details (in particular, in dependence of amplitude and focusing degree) in Ref. [15].

4.3 Conclusion

It was proposed [13, 15, 16, 20, 25, 73, 74] that coherent superposition of focused optical laser pulses is favorable for future observations of spontaneous pair production below the Schwinger limit because of constructive interference, which notably increases the peak field strength. In this context, it is natural to analyze phase dependence of the arising interference pattern, as well as the possibilities for phase control of the corresponding pair production rate. Here we have done it with respect to both phase shifts inherent to the problem, the carrier envelope phase $\tilde{\varphi}$ of individual pulses, and their relative phase shift Ψ. As shown, their variation shifts the spiky interference pattern of the invariant electric field with respect to the carrier envelope, leaving the widths of the peaks unaltered.

The same conclusion broadly refers to the pair production rate, which depends on the invariant fields monotonously. Indeed, in all the cases considered here we could relate the peculiarities of particle distribution to the underlying invariant field structure. However, since due to exponentiation in Eqs. (4.1) or (4.2), at the level of production rate only those peaks of the invariant electric field that are closest to the center of the spatiotemporal envelope remain significant, the resulting spatial and temporal distributions of created pairs can look either nearly unimodal or bimodal. For the same reason, their longitudinal and temporal spike widths are much smaller than of the original invariant field structure, meaning time-localized (during hundreds attoseconds) formation of extremely short (tens nanometers long) electron-positron bunches. The post production dynamics of such dense bunches may be highly non-trivial [74] and may need a separate study.

We predict that the total pair production is maximal when one of the spikes is located near the center of the spatiotemporal envelope (and distribution of created pairs looks approximately unimodal), and minimal when the neighboring spikes are off-centered but located symmetrically. The particular phase shifts required for each case depend on polarization of the pulses. Among the considered cases, for the parameters adopted here the global maximum is achieved with a circularly polarized RR configuration considered in Ref. [15].

Possibility of phase control of Schwinger pair production under discussion may be useful, e.g., to increase the attainable intensity of tightly focused colliding laser pulses by reducing pair production and hence preventing field depletion at their crossing, or, conversely, to measure the typically unknown field structure and phase relations of extremely strong laser pulses in a way similar to proposed in Ref. [42] by using the multiphoton Compton scattering.

Chapter 5

Imprint of temporal envelope of ultra short laser pulses on momentum spectrum of e^+e^- pairs

In this **Chapter** effect of temporal pulse shape of intense ultrashort pulses on the momentum distribution of e^+e^- pairs is studied using quantum kinetic equation. Two closely resembling temporal envelopes namely, Gaussian and Sauter, keeping all the other pulse parameters same, are considered to this end.

In previous **Chapters**, Schwinger's formula was used to compute the spatio-temporal distribution of pairs created by time and space varying fields due of ultrashort and ultraintense laser pulses with the justification that the length and time scales of the variation are much larger than the characteristic Compton length and time. However, as the pulse duration is reduced further in the range of few hundreds of atto-second when it is no more much larger than the characteristic Compton time, use of Schwinger formula to describe the pair production rate is questionable. Furthermore in such cases the transient and non-equilibrium dynamics of the produced particles can only be described in the framework of the kinetic theory approach using quantum Vlasov equation (QVE) [19, 31, 45–60]. This methodology has a strong relevance in the context of the momentum distribution of the created pairs in semiclassical approximation where the asymptotic reflection coefficient gives the average particle numbers in a particular mode [61]. The momentum spectrum of created particles has also been studied in nonpertubative multiphoton regime where the Keldysh adiabaticity parameter $\xi \sim 1$ [75]. The semiclassical formulation was used in studying the time-domain multiple-slit interference effect from vacuum in [76]. The theory was used to study the rich dynamical behaviour of the pair creation process for the time dependent but spatially homogeneous field configuration [19, 53, 62]. In particular, it was shown that a quasi particle mode evolves through three distinct temporal stages, namely the quasi electron positron plasma (QEEP) stage, the transient stage and finally the residual electron-positron plasma (REPP) stage [58–60] The temporal characteristics of the ultrashort pulses consist of a temporal profile with a given pulse duration τ, number of subcycle oscillations $\omega\tau$ with ω being the carrier frequency, carrier envelope phase (CEP) and frequency chirp parameter(s). Gaussian and Sauter are the two most commonly used (quite often interchangeably) temporal profiles. A simple Sauter pulse without any subcycle oscillation (also known as single sheeted Sauter pulse) offers analytical solutions for the momentum distribution [56] and the dynamics of produced pairs [49]. However, a Sauter pulse with subcycle oscillations (multi sheeted pulse) is no longer analytically tractable. On the other hand, for a multi sheeted Gaussian pulse it is possible to express the vector potential in an analytically closed form in terms of error function. These analytical conveniences have led researchers to use Sauter and Gaussian temporal profiles for the kinetic studies of the pairs created by the single sheeted and multi sheeted pulses, respectively [31], sometimes even in the same report [59]. This is possibly due to the perception that both the pulses should give very similar results because of their close resemblance. This, to the best of our knowledge, has not been verified so far. This is one of the motivations of this study. While the evolution of individual modes was studies in Ref. [59, 60], the evolution of the momentum distribution as a whole has not been reported so far. This is the second motivation of our study. In this **Chapter** we, therefore, use quantum kinetic equation to present a detailed comparative study of the evolution of longitudinal momentum distribution of the pairs created by these two pulses (Sauter and Gaussian) for a given pulse duration, number sub-cycle oscillations, CEP, and frequency chirp.

We find that the momentum spectrum of the pairs for the Sauter and Gaussian pulses differ significantly at all the temporal stages of the evolution. However, for the qualitative description of the difference only two temporal regions seem to be relevant - first one is the region from the QEEP stage to the transient stage (referred to as the transient region hereafter) and the second one is the region well beyond the transient stage (also referred to as the asymptotic region). In the transient region, the spectrum is smooth with a single peak for both the pulses. However the location of peak, the peak height and the width are different for any instant of time and they evolve differently with time. However the peak height for the Gaussian pulse is consistently higher than that for the Sauter pulse. In the other regime, where the spectrum does not change with time, the peak position of the spectrum nearly coincides in both the cases. However, in the asymptotic region, just contrary to the trend in the transient region, the peak height of the spectrum for the Gaussian pulse is lower than that for the Sauter pulse as long as the number of subcycle oscillations, $\omega\tau < 5$. As reported in Ref. [77], the momentum spectrum for the multisheeted Gaussian shows oscillations over the smooth profile due to the quantum mechanical interference of the reflected quasi particle waves from bumpy time-dependent potential. These oscillation are suppressed in the case of Sauter pulse. The onset of oscillation takes place at $\omega\tau = 6$ for the Sauter pulse compared to $\omega\tau = 4$ for the Gaussian pulse. Furthermore, for the same value of $\omega\tau$ the amplitude of oscillation is smaller for the Sauter pulse. In fact, it is due to this interference effect that the peak height of the momentum spectrum for the Gaussian pulse takes over that for the Sauter pulse for $\omega\tau \geq 5$. These difference in the asymptotic time spectrum of the two pulses get much more prominent on increasing the linear frequency chirp in these pulses and also on varying the CEP.

This **Chapter** is structured as follows: In Sec. 5.1 we discuss briefly the relevance of the aforesaid pulses to the counterpropagating configuration of intense ultrashort pulses. We also outline the basic formulation of the quantum kinetic equation (QKE) in the context of particle production from the time dependent but spatially uniform electric fields. We present our numerical results for the multi-sheeted Sauter and Gaussian pulses with different values of $\omega\tau$ parameter in Sec. 5.2. The effect of varying the carrier-envelope offset phase and the linear frequency chirp on the momentum spectrum is also studied in this section. The results are qualitatively explained by invoking the equivalence between the pair creation by EM field and the over-the-barrier scattering problem and also quantitatively by analysing the structure of turning points in the complex t-plane in the stationary phase approximation. We conclude in Sec. 5.3. Details of the calculation based on the turning point structure showing the essential difference in the momentum spectrum of the two temporal pulse forms are relegated to Appendix. D.

5.1 Theory

5.1.1 Laser field model

It is well known that the electric field given by the spatially homogeneous Sauter/ Gaussian pulse may arise in the focal region of the counterpropagating laser pulses. Here we give two such examples from Ref. [66, 67] wherein the focused EM field model by Narozhny-Fofanov [10] was used. When the counterpropagating pulses with amplitude $E_0/2$ are linearly e-polarized or are in combination of right-left circular polarization the expressions of the electric and magnetic fields at the focus ($x = y = z = 0$) are of the form

$$E(t) = E_0 g(t)\sin(\omega t + \phi), \quad H(t) = 0, \tag{5.1}$$

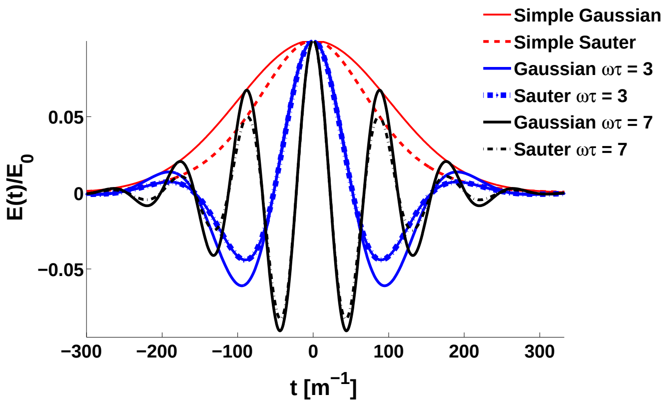

FIGURE 5.1: Plot of multi-sheeted Sauter (dashed line) and Gaussian (simple line) pulses for $\omega\tau = 3$ (blue) to $\omega\tau = 7$ (black) multi-sheeted Sauter and Gaussian pulses. The single-sheeted Sauter and Gaussian fields (red) are given as a reference. The field parameters are $E_0 = 0.1$, $\tau = 100$, $\phi = \pi/2$ and all the units are taken in electron mass unit.

where $g(t)$ is the temporal envelope function which describes the electric field of a finite duration and ϕ is the carrier-envelope offset phase i.e., the phase difference between the high frequency carrier wave and the envelope function [42–44]. If we take $g(t) = \exp(-t^2/2\tau^2)$, we get the spatially uniform multi-sheeted Gaussian field

$$E(t) = E_0 \exp(-t^2/2\tau^2) \sin(\omega t + \phi), \quad H(t) = 0, \tag{5.2}$$

where τ is the total pulse length. On the other hand, by taking $g(t) = \cosh^{-2}(t/\tau)$ the form of the multi-sheeted Sauter field

$$E(t) = E_0 \cosh^{-2}(t/\tau) \sin(\omega t + \phi), \quad H(t) = 0. \tag{5.3}$$

These are the two widely used temporal fields in the studies of QKE.

The applicability of the spatially uniform field approximation may be justified as the spatial length scale of the EM field of the laser pulse is much larger than the characteristic Compton length ($\lambda\!\!\!^- = \hbar/m_e c$) of the QED process. The corresponding time dependent vector potential $\vec{A}(t) = (0, 0, A(t))$ can easily be calculated by the relation $\vec{E}(t) = -\partial\vec{A}(t)/\partial t$ where we have assumed the scalar potential $A_0 = 0$ (temporal gauge). Fig. 5.1 shows the shape of the time dependent electric field for Sauter and Gaussian pulses with different values of $\omega\tau$ parameter. The value of the $\omega\tau$ parameter is taken as 3 and 7. The shape of the simple Sauter ($E(t) = E_0 \cosh^{-2}(t/\tau)$) and simple Gaussian ($E(t) = E_0 \exp(-t^2/2\tau^2)$) fields (these are also known as single-sheeted Sauter and Gaussian fields) are shown as a reference. We use Eq. 5.1 for the multi-sheeted electric fields to calculate the momentum spectrum of created particles.

5.1.2 Mathematical formalism of the quantum kinetic theory

The kinetic equation used in this work has been derived using different techniques by various researchers [32, 56, 57]. Here we give the essential steps closely following the derivation given [32, 55]. The basic formulation of fermionic pair production can be derived from the Dirac equation for the matter field $\Psi(x)$

$$(i\gamma^{\mu}\partial_{\mu} - e\gamma^{\mu}A_{\mu} - m)\Psi(x) = 0. \tag{5.4}$$

Here, we have assumed the external electric field is a classical background and take one dimensional spatially uniform but time dependent electric field which is characterized by the 4-vector potential $A_{\mu} = (0, 0, 0, A(t))$. The electric field can easily be calculated by $E(t) = -dA(t)/dt$. As the external gauge field varies in time one can decompose the spinor field in Fourier mode [61]

$$\Psi(\mathbf{x}, t) = \sum_{s} \int d^3p\, e^{i\mathbf{p}\cdot\mathbf{x}} \Big(u_{\mathbf{p},s}(t) b_{\mathbf{p},s}(t) + v_{-\mathbf{p},s}(t) d^{\dagger}_{-\mathbf{p},s}(t) \Big), \tag{5.5}$$

where $b_{\mathbf{p},s}(t)$ and $d^{\dagger}_{-\mathbf{p},s}(t)$ are the annihilation and creation operators for the particle and antiparticle with momenta $\pm\mathbf{p}$ and spin s in a time dependent basis. In a particular Dirac matrix basis (eigenvectors of $\gamma^0\gamma^3$), one can write the time dependent spinors $u_{\mathbf{p},s}(t)$ and $v_{\mathbf{p},s}(t)$ as a single function $\psi_{\mathbf{p}}(t)$, which satisfies the equation

$$\ddot{\psi}_{\mathbf{p}}(t) + (\omega^2_{\mathbf{p}}(t) + i\dot{P}_3(t))\psi_{\mathbf{p}}(t) = 0, \tag{5.6}$$

where $\omega^2(\mathbf{p}, t) = m^2 + \mathbf{p}^2_{\perp} + P^2_3(t)$ and $P_3(t) = p_3 - eA(t)$.

Here one can define the adiabatic particle number basis where the creation and annihilation operators are written as

$$B_{\mathbf{p},s}(t) = b_{\mathbf{p},s}(t) e^{-i\Theta(\mathbf{p},\, t)}, \quad D_{\mathbf{p},s}(t) = d_{\mathbf{p},s}(t) e^{-i\Theta(\mathbf{p},\, t)}, \tag{5.7}$$

where $\Theta(\mathbf{p}; t) = \int_{t_0}^{t} dt' \omega(\mathbf{p}, t')$ is the dynamical phases accumulated between initial and final states. The operators $B_{\mathbf{p},s}(t)$ and $D_{\mathbf{p},s}(t)$ satisfy the Heisenberg-like equations of motion

$$\begin{aligned} \frac{dB_{\mathbf{p},s}(t)}{dt} &= -\frac{eE(t)\epsilon_{\perp}}{2\omega^2(\mathbf{p}, t)} D^{\dagger}_{-\mathbf{p},s}(t) + i[H(t), B_{\mathbf{p},s}(t)], \\ \frac{dD_{\mathbf{p},s}(t)}{dt} &= \frac{eE(t)\epsilon_{\perp}}{2\omega^2(\mathbf{p}, t)} B^{\dagger}_{-\mathbf{p},s}(t) + i[H(t), D_{\mathbf{p},s}(t)], \end{aligned} \tag{5.8}$$

where the quasi-particle Hamiltonian $H(t)$ is given by

$$H(t) = \sum_{s,\mathbf{p}} \omega(\mathbf{p},t)\Big(B^{\dagger}_{\mathbf{p},s}(t)B_{\mathbf{p},s}(t) - D_{-\mathbf{p},s}(t)D^{\dagger}_{-\mathbf{p},s}(t)\Big). \tag{5.9}$$

We now define the occupation number of electron in a time dependent basis with spin s and momentum $\mathbf{p}$ for the instantaneous vacuum state $f_s(\mathbf{p},t) =< 0_{in}|B^{\dagger}_{\mathbf{p}s}(t)B_{\mathbf{p}s}(t)|0_{in} >$. Similarly one can also define the occupation number of the positron $\bar{f}_s(-\mathbf{p},t) =< 0_{in}|D^{\dagger}_{-\mathbf{p}s}(t)D_{-\mathbf{p}s}(t)|0_{in} >$. Here $f_s(\mathbf{p},t) = \bar{f}_s(-\mathbf{p},t)$ due the charge conjugation invariance. Now $f_s(\mathbf{p},t)$ and $\bar{f}_s(-\mathbf{p},t)$ will serve as a single particle distributions functions in quasi-particle representation [49, 78]. The evolution of $f_s(\mathbf{p},t)$ satisfies the equation

$$\frac{df_s(\mathbf{p},t)}{dt} = -\frac{eE(t)\epsilon_{\perp}}{2\omega^2(\mathbf{p},t)} Re\{\phi_s(\mathbf{p},t)\}, \tag{5.10}$$

where $\phi_s(\mathbf{p},t) =< 0_{in}|D_{-\mathbf{p}s}(t)B_{\mathbf{p}s}(t)|0_{in} >$ is the anomalous average of in-vacuum state denoting the complex particle-antiparticle correlation function. It satisfies the evolution equation

$$\frac{d\phi_s(\mathbf{p},t)}{dt} = \frac{eE(t)\epsilon_{\perp}}{\omega^2(\mathbf{p},t)}[2f_s(\mathbf{p},t) - 1] - 2i\omega(\mathbf{p},t)\phi_s(\mathbf{p},t), \tag{5.11}$$

provided that $f_s(\mathbf{p},t) = \bar{f}_s(-\mathbf{p},t)$ is used. In general, one can write the real and imaginary parts of $\phi_s(\mathbf{p},t) = u_s(\mathbf{p},t) + iv_s(\mathbf{p},t)$ for which Eq. 5.11 can be decomposed into two real equations

$$\begin{aligned} \frac{du_s(\mathbf{p},t)}{dt} &= \frac{eE(t)\epsilon_{\perp}}{\omega^2(\mathbf{p},t)}[2f_s(\mathbf{p},t) - 1] + 2\omega(\mathbf{p},t)v_s(\mathbf{p},t), \\ \frac{dv_s(\mathbf{p},t)}{dt} &= -2\omega(\mathbf{p},t)u_s(\mathbf{p},t). \end{aligned} \tag{5.12}$$

In particular, we have a set of three first order differential equations for the complete dynamical evolution of the vacuum electron-positron pair production process which are listed as (we have absorbed an extra minus sign which appears in above equations of $f(\mathbf{p},t)$, $u(\mathbf{p},t)$ and $v(\mathbf{p},t)$ and the spin index s)

$$\begin{aligned} \frac{df(\mathbf{p},t)}{dt} &= \frac{eE(t)\epsilon_{\perp}}{2\omega^2(\mathbf{p},t)}u(\mathbf{p},t), \\ \frac{du(\mathbf{p},t)}{dt} &= \frac{eE(t)\epsilon_{\perp}}{\omega^2(\mathbf{p},t)}[1 - 2f(\mathbf{p},t)] - 2\omega(\mathbf{p},t)v(\mathbf{p},t), \\ \frac{dv(\mathbf{p},t)}{dt} &= 2\omega(\mathbf{p},t)u(\mathbf{p},t). \end{aligned} \tag{5.13}$$

The real part of the anomalous average term $u(\mathbf{p},t)$ which represents vacuum polarization effects plays an important role in the source term of the pair production. In fact this term gives the information about the quantum statistical character via $[1 - 2f(\mathbf{p},t)]$, due to the Pauli exclusion principle. Similarly the imaginary part of anomalous average term $v(\mathbf{p}, t)$ denotes the counter process of pair production which is basically the pair annihilation in the vacuum excitation process [19]. One can also combine the above set of first order differential equation into a single first order integro-differential equation

$$\frac{df(\mathbf{p},t)}{dt} = \frac{eE(t)\epsilon_\perp^2}{2\omega^2(\mathbf{p},t)} \int_{-\infty}^{t} dt' \frac{eE(t')}{\omega^2(\mathbf{p},t')}[1-2f(\mathbf{p},t')]\cos[2\Theta(\mathbf{p};t,t')], \tag{5.14}$$

which is the quantum transport equation of the vacuum particle pair production [32, 63] where the non-Markovian character or the memory effect is evident via the term $[1-2f(\mathbf{p},t)]$ and the highly oscillating kernel $\cos[2\Theta(\mathbf{p};t,t')]$. The detailed derivation of Eq. 5.14 is given in **Appendix** D.

We solve the Eq. 5.13 numerically for time dependent single and multi-sheeted ultrashort Sauter and Gaussian laser pulses as discussed in Sec. 5.1.1 with initial conditions $f(\mathbf{p},t_i) = u(\mathbf{p},t_i) = v(\mathbf{p},t_i) = 0$ at $t_i \to -\infty$ instead of solving the Eq. 5.14 which is non-local in time and involves very rapidly oscillating phase with double the frequency of $\omega(\mathbf{p},t)$ of the quasi-particle. It is worthwhile to mention that the set of coupled differential equations of $(f(\mathbf{p},t), u(\mathbf{p},t),$ and $v(\mathbf{p},t))$ has the first integral of motion $(1-2f(\mathbf{p},t))^2 + u(\mathbf{p},t)^2 + v(\mathbf{p},t)^2 = 1$ [79].

5.2 Results

In this section we present the momentum spectrum of the created particle based on the numerical solution of Eq. 5.13 for time dependent Sauter and Gaussian pulses, thereby showing its sensitivity to the temporal envelope of the pulse.

5.2.1 Momentum distribution of created particles in the transient and asymptotic regions

The evolution of the vacuum state undergoes Zitterbewegung which gets modified by the interaction of time dependent electric field with quasi-energy $\omega(\mathbf{p},t) = \sqrt{m^2 + \mathbf{p}_\perp^2 + P_3^2(t)}$ and quasi-momentum $P_3(t) = p_3 - eA(t)$. The initial virtual electron-positron pair plasma state in the presence of single sheeted Sauter and multi sheeted Gaussian pulses was shown to evolve from the quasi-electron positron (QEPP) stage to final residual electron-positron plasma (REPP) stage

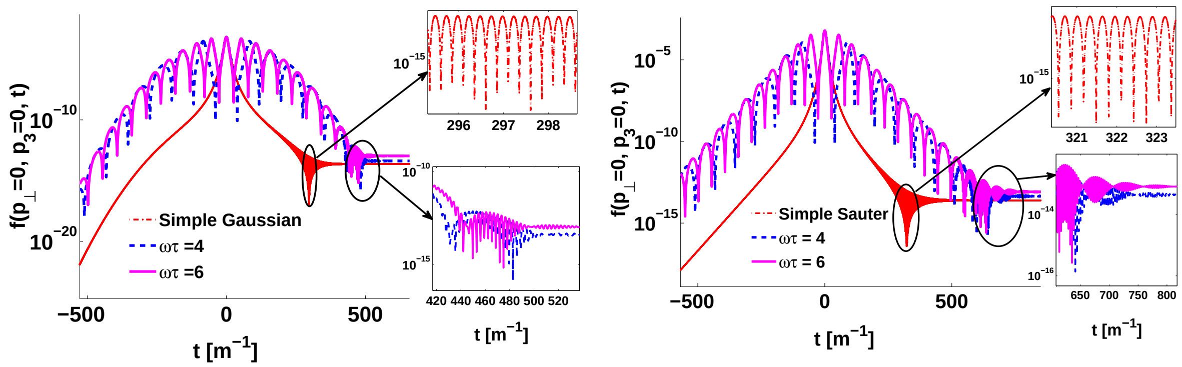

FIGURE 5.2: Evolution of quasi-particle distribution function for single and multi-sheeted ($\omega\tau = 4, 6$) Gaussian and Sauter pulses for longitudinal momentum $p_3 = 0$ and transverse momentum $\mathbf{p}_\perp = 0$. All the units are taken in electrons mass unit. The field parameters are $E_0 = 0.1$, $\tau = 100$, and the carrier-envelope offset phase $\phi = \pi/2$.

via the highly oscillating transient stage [58, 59]. The evolution for single sheeted Gaussian and multi sheeted Sauter pulses has not been reported so far. Moreover, there are no results available for the pulse parameters of both the pulses we wish to consider in this **Chapter**.

We, therefore, show the complete evolution of the quasi-particle distribution function for the single and multi-sheeted ($\omega\tau = 4, 6$) Gaussian (in the left panel) and Sauter (right panel) pulses in Fig. 5.2 for the longitudinal momentum value $p_3 = 0$. The insets of Fig. 5.2 show the evolution of the quasi-particle distribution function in the transient stage of evolution characterized by rapid oscillations. We note here that the transient stage occurs at earlier times for the Gaussian pulse than the Sauter pulse.

Use of the QKE formalism allows us to study the quasi-particle momentum spectrum at any instant of time and hence the evolution thereof. As mentioned before we, however, restrict ourself to two distinct temporal regimes, namely the transient regime (consisting of QEPP and transient stages) and the asymptotic region (well beyond the transient stage in REPP stage). Fig. 5.3 shows momentum spectra for single sheeted Sauter and Gaussian pules. The spectra, which have smooth unimodal structure, change rapidly in the transient region. The location of the central peak and the peak height of the momentum spectrum are quite different for both the pulses. In particular, the spectrum for the Gaussian pulse has larger peak height than that for the Sauter pulse in this region, as seen in Figs. 5.3(a-b). However in the asymptotic region the momentum spectra for both the pulses become centrally symmetric about $p_3 = 0$. Contrary to the trend in the transient region, the peak height is larger for the Sauter pulse in the asymptotic region. For the single-sheeted Sauter pulse with electric field $E(t) = E_0 \cosh^{-2}(t/\tau)$ and the corresponding vector potential $A(t) = -E_0\tau \tanh(t/\tau)$, QKE in Eq. 5.14 was shown to have exact solution in the asymptotic region [63]. It was shown [61] that in the stationary phase

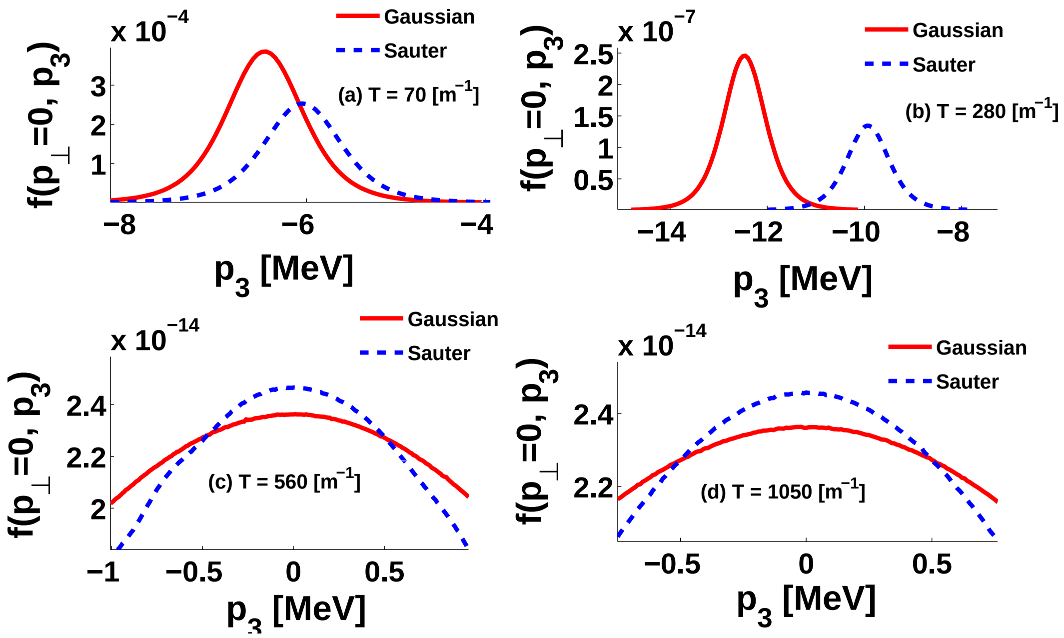

FIGURE 5.3: Longitudinal momentum spectrum of created particles in the presence of time dependent single sheeted Sauter and Gaussian pulses at different times. The value of transverse momentum is taken to be zero and all the units are taken in electrons mass unit. The field parameters are $E_0 = 0.1$, $\tau = 100$, and the carrier-envelope offset phase $\phi = \pi/2$.

approximation, the asymptotic time spectrum is governed by the structure of the turning points t_p in the complex time plane which are defined by the relation $\omega(\mathbf{p}, t_p) = 0$. In this case, $t_p = \tau \tanh^{-1}((\pm im - p_3)/eE_0\tau) + in\pi\tau$ where n is integer number. The turning points appear as complex conjugate pairs. For $p_3 = 0$, all the turning points are located on imaginary axis. The dominant contribution to the momentum spectrum comes from $n = 0$ turning points. Thus, the pair creation mechanism is governed by the single pair of turning point and the asymptotic particle spectrum becomes smooth unimodal profile.

We now consider multi-sheeted Sauter and Gaussian pulses for $\omega\tau = 4$ and 6 and present in Fig. 5.4 the momentum spectrum in the transient region ($t = 70[m^{-1}]$, $280[m^{-1}]$) and in the asymptotic region ($t = 1050[m^{-1}]$ for Sauter and Gaussian pulses. The momentum spectra in the transient region, much like the trend discussed above, significantly differ for the two pulses for the same number of subcycle oscillations, with the peak height for the Sauter pulse being consistently lower than that for the Gaussian pulse. In the asymtotic region, oscillations over the otherwise smooth unimodal momentum spectrum for the multi sheeted Gaussian pulse were reported in [61, 77]. These results are reproduced here for the ready reference here while comparing the results obtained for the corresponding Sauter pulses. We find that the oscillation become noticeable for $\omega\tau \geq 4$ for the Gaussian pulse and for $\omega\tau \geq 6$ for the Sauter pulse, see the lower panel of the Fig. 5.4 and also Fig. 5.5.

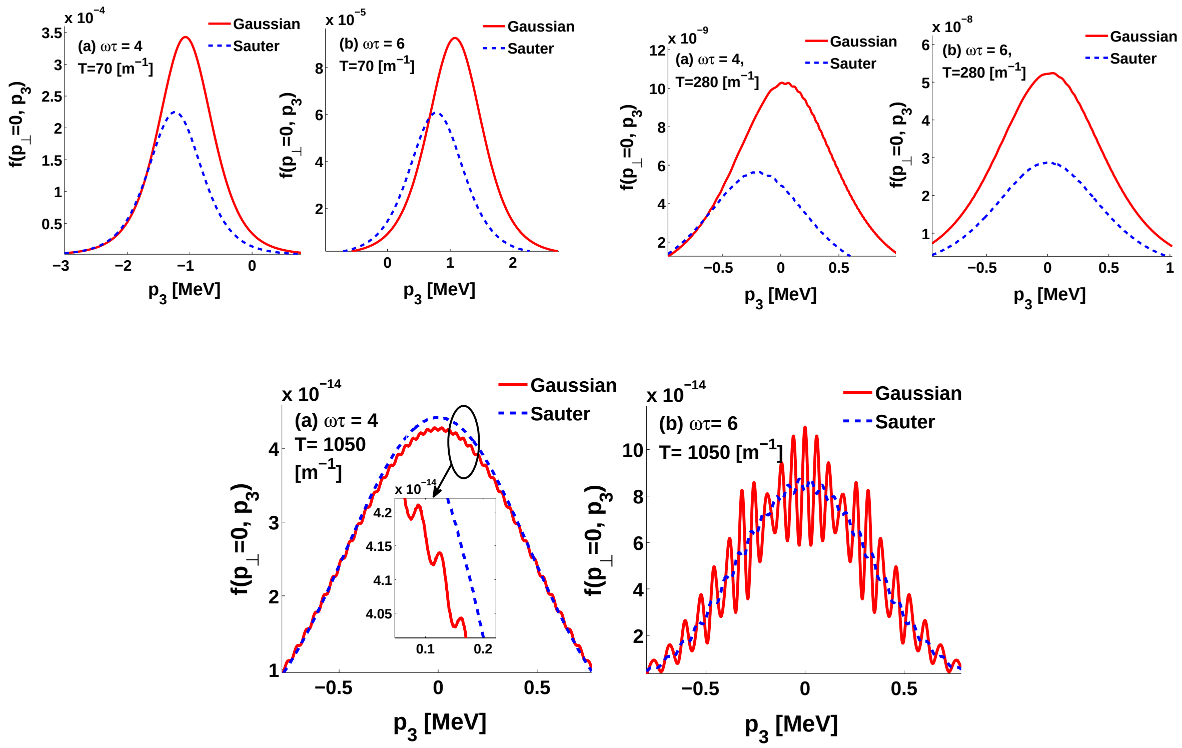

Figure 5.4: Longitudinal momentum spectrum of created particles in the presence of time dependent multi-sheeted Sauter and Gaussian pulses at different times for $\omega\tau = 4, 6$. The value of transverse momentum is taken to be zero and all the units are taken in electrons mass unit. The field parameters are $E_0 = 0.1$, $\tau = 100$, and the carrier-envelope offset phase $\phi = \pi/2$.

For the same number of subcycle oscillations, the amplitude of oscillations is larger for the Gaussian pulse than that for the Sauter pulse, as seen in Fig. 5.5. In fact, the spectrum for the $\omega\tau = 6$ Gaussian pulse is similar to that for the Sauter pulse with $\omega\tau = 7$ (Fig. 5.5) as far as the oscillations in both cases are concerned (note the scaling factors). As long as the oscillations are not prominent ($\omega\tau \leq 5$) the spectrum has higher peak value for the Sauter pulse than that for the Gaussian pulse. With the increase in the oscillation amplitude in the momentum spectrum for Gaussian pulses the trend reverses for ($\omega\tau \geq 6$).

5.2.2 Scattering potential structure for the Gaussian and Sauter pulses

The physical explanation of the onset of oscillation over the otherwise smooth momentum spectrum induced due to the subcycle oscillation in the multi-sheeted Gaussian pulse was provided by Dumlu in a seminal work [31] by mapping the problem of pair creation by the spatially uniform time dependent pulses to the well studied over the barrier scattering problem of quantum mechanics. It was shown that the pairs creation is related to the reflection of the initial

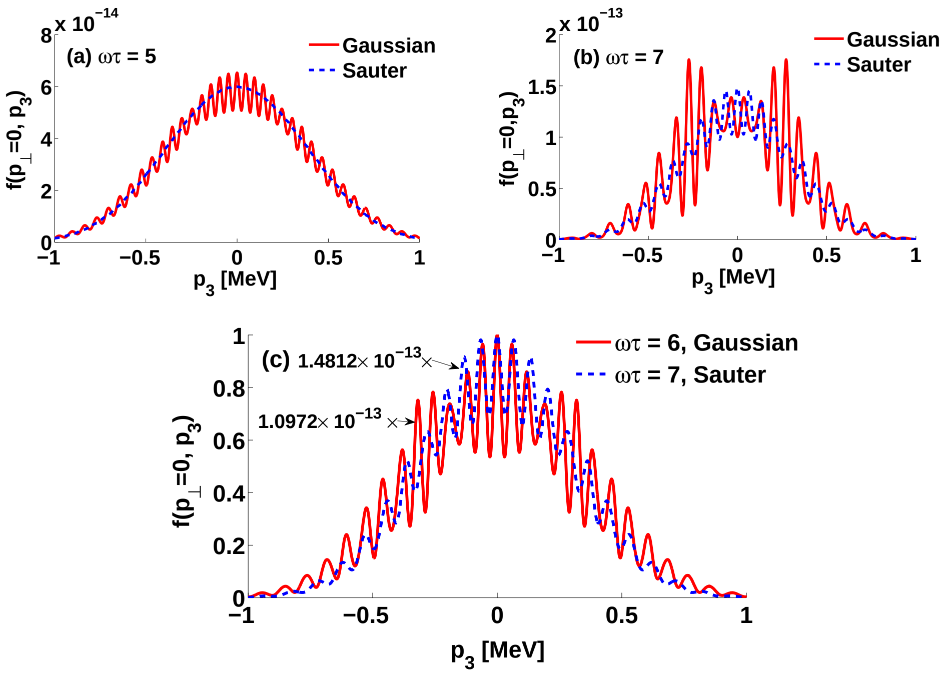

FIGURE 5.5: Asymptotic longitudinal momentum distribution function (calculated at $t = 10.5\tau$) of the created particles in the presence of time dependent multi-sheeted Sauter and Gaussian pulse for different values of $\omega\tau$ parameter. (a) $\omega\tau = 5$, (b) $\omega\tau = 7$ for both the pulses. (c) $\omega\tau = 6$ for the Gaussian pulse and $\omega\tau = 7$ for the Sauter pulse. The distribution functions are scaled with the respective peak values. The value of transverse momentum is taken to be zero and all the units are taken in electrons mass unit. The field parameters are $E_0 = 0.1$, $\tau = 100$, and the carrier-envelope offset phase $\phi = \pi/2$.

$t \to -\infty$ quasi particle mode with longitudinal momentum p_3 (transverse momentum $\mathbf{p}_\perp = \mathbf{0}$ without any loss of generality) at asymptotic times $t \to \infty$ due to the time dependent scattering potential, $V(t) = -(p_3 - eA(t))^2$. We use the same physical picture to explain the suppression of oscillations in the momentum spectrum of the pairs created by the Sauter pulse. In Fig. 5.6, we present the scattering potential $V(t) = -(p_3 - eA(t))^2$ for multi sheeted Sauter and Gaussian pulses with $\omega\tau = 3, 4, 5, 6, 7$ for the longitudinal momentum $p_3 = 0$. The potential is symmetric about $t = 0$. It is smooth, having a single bump (or barrier) for the single sheeted pulses (not shown here) and the multi sheeted pulses having small number of subcycle oscillations, $\omega\tau \leq 3$ (only $\omega\tau = 3$ case shown here). As the value of $\omega\tau$ is increased the structure of the potential gets more bumpy causing multiple reflections of the incident wave. It is the interference of the multiple reflected waves which results in the oscillations in the momentum spectrum at asymptotic times. For $\omega\tau = 4$, the scattering potential, as shown in Fig. 5.6(b) has three bumps – the larger one in the centre and two smaller ones on either side of the central one towards the tail region of the pulse. For the Sauter pulse, on the other hand, the scattering potential has one bump in the centre, with the side bumps being hardly visible. Hence, the momentum spectrum for the Sauter pulse with $\omega\tau = 4$ in Fig. 5.4 does not show the interference effects. On the other hand the spectrum for the corresponding Gaussian pulse in Fig. 5.4 does show mild interference effect in form very small amplitude oscillations over the smooth unimodal profile.

With the increase in the number of subcycle oscillations, the existing side bumps become more prominent and additional side bumps appear in the scattering potential. In all the cases, however, the side bumps for the Sauter pulse are less prominent than those for the corresponding Gaussian pulse. Relative strength of the prominent side bumps relative to the central one is nearly 1/3 for the Sauter pulse and 1/2 for the Gaussian pulse with $\omega\tau = 6$. For $\omega\tau = 7$, it is about 1/2 for the Sauter pulse and 3/2 for the Gaussian pulse. This explains the relative suppression of oscillations in the momentum spectrum for the Sauter pulse.

The side bumps for the Sauter pulse become visible for $\omega\tau = 5$ (Fig. 5.6(c)) but these are too small to cause any discernible interference effects in the momentum spectrum. The onset of oscillation in the momentum spectrum for the Sauter pulse takes place only at $\omega\tau = 6$. In Fig. 5.6, we compare the scattering potential due to the Sauter pulse with $\omega\tau = 7$ with that due to the Gaussian pulse with $\omega\tau = 6$. The similarity of the two potential structures explain the similarity in the momentum spectrum for the two pulses with different number of subcyle oscillations.

It may be helpful to relate the difference in the scattering potential due to Sauter and Gaussian pulses to their respective electric field profiles. As seen in Fig. 5.1, for higher values of $\omega\tau$, the subcycle oscillations located away from the centre of the temporal envelope are more intense for the Gaussian pulse making thereby the side bumps more prominent.

5.2.3 Turning point structure for Sauter and Gaussian pulses

In [31, 61], a theoretical framework was developed to calculate the reflection amplitude for the over barrier scattering problem and hence the momentum spectrum of the created pairs by the spatially uniform time dependent pulses. In particular, it was shown that for a subcritical field for which the reflection amplitude in the asymptotic time limit $|R_{\mathbf{p}}(\infty)| \ll 1$, it is possible express $R_{\mathbf{p}}(\infty)$ as a sum involving all the turning points:

$$R_{\mathbf{p}}(\infty) \approx \sum_{t_p} (-1)^p e^{i\pi/2} e^{-2i \int_{-\infty}^{t_p} dt' \omega(\mathbf{p},t')}. \tag{5.15}$$

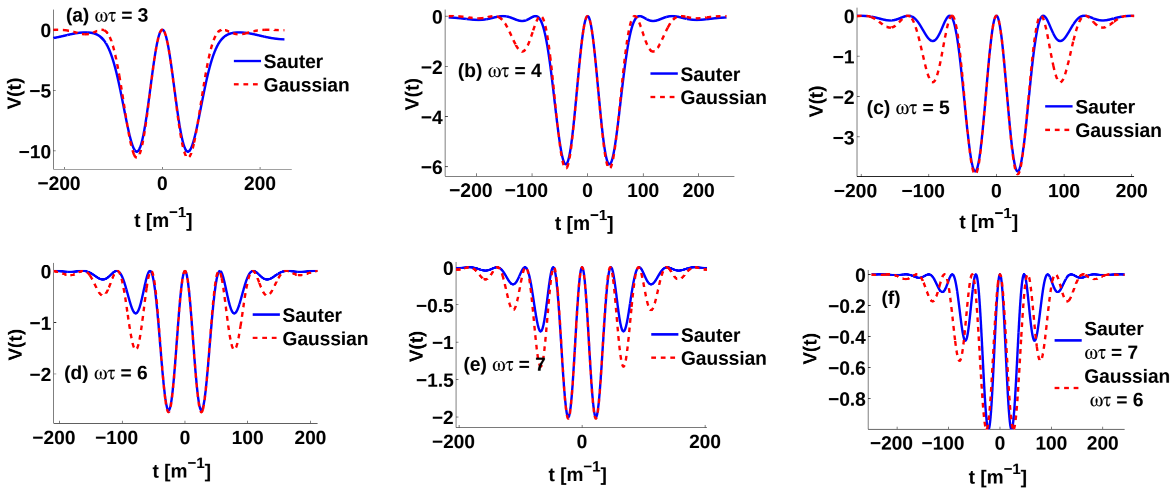

FIGURE 5.6: Over-the-barrier scattering potential $V(t) = -(p_3 - eA(t))^2$ for time dependent multi-sheeted Gaussian and Sauter electric pulses. From top left to bottom middle the value of the $\omega\tau = 3, 4, 5, 6, 7$. The scaled scattering potentials due to the Sauter pulse with $\omega\tau = 7$ and the Gaussian pulse with $\omega\tau = 6$ are shown on the bottom left. Longitudinal and transverse momenta $p_3 = 0$ and $p_\perp = 0$. All units are expressed in electrons mass unit. The field parameters are $E_0 = 0.1$, $\tau = 100$, and the carrier-envelope offset phase $\phi = \pi/2$.

As mentioned earlier, turning points t_p are defined in the complex t-plane by the relation $\omega(\mathbf{p}, t_p) = 0$. They appear in complex conjugate pairs as the vector potential $A(t)$ considered here is real. It was argued in Ref. [52] that the function $\exp(-2i \int_{-\infty}^{t_p} dt' \omega(\mathbf{p}, t'))$ is oscillatory along the real axis of complex t-plane and exponentially decaying along the imaginary axis. Thus, only the pairs of turning points located near the real axis contribute significantly to the reflection amplitude and the corresponding terms in the expression of reflection amplitude represent the reflection due to the significant bumps discussed in the previous subsection. If the reflection is governed by more than a single pair of turning points, the resulting momentum spectrum of pairs will show interference effects in form of oscillations. For definiteness, the asymptotic momentum distribution $f_{\mathbf{p}}(\infty) = |R_{\mathbf{p}}(\infty)|^2$ is given by [61]

$$f_{\mathbf{p}}(\infty) \approx \sum_{t_p} e^{-2K_{\mathbf{p}}^{(p)}} + 2 \sum_{t_{p'} \neq t_p} (-1)^{(p-p')} \cos\left(2\Theta_{\mathbf{p}}^{(p,p')}\right) e^{-K_{\mathbf{p}}^{(p)} - K_{\mathbf{p}}^{(p')}}, \tag{5.16}$$

where $K_{\mathbf{p}}^{(p)} = \left| \int_{t_p^*}^{t_p} dt\, \omega(\mathbf{p}, t) \right|$ and $\Theta_{\mathbf{p}}^{(p,p')} = \int_{Re(t_p)}^{Re(t_{p'})} dt\, \omega(\mathbf{p}, t)$. In Eq. 5.16, the first term on the right hand side contains the contribution of reflections from all the pairs of turning points and the second term represents the inference of reflected waves from different pairs of turning points. Because of the exponential suppression factor $\exp(-2K_{\mathbf{p}}^{(p)})$ the dominant contribution to the asymptotic distribution function comes from those pairs of turning points which are closer to

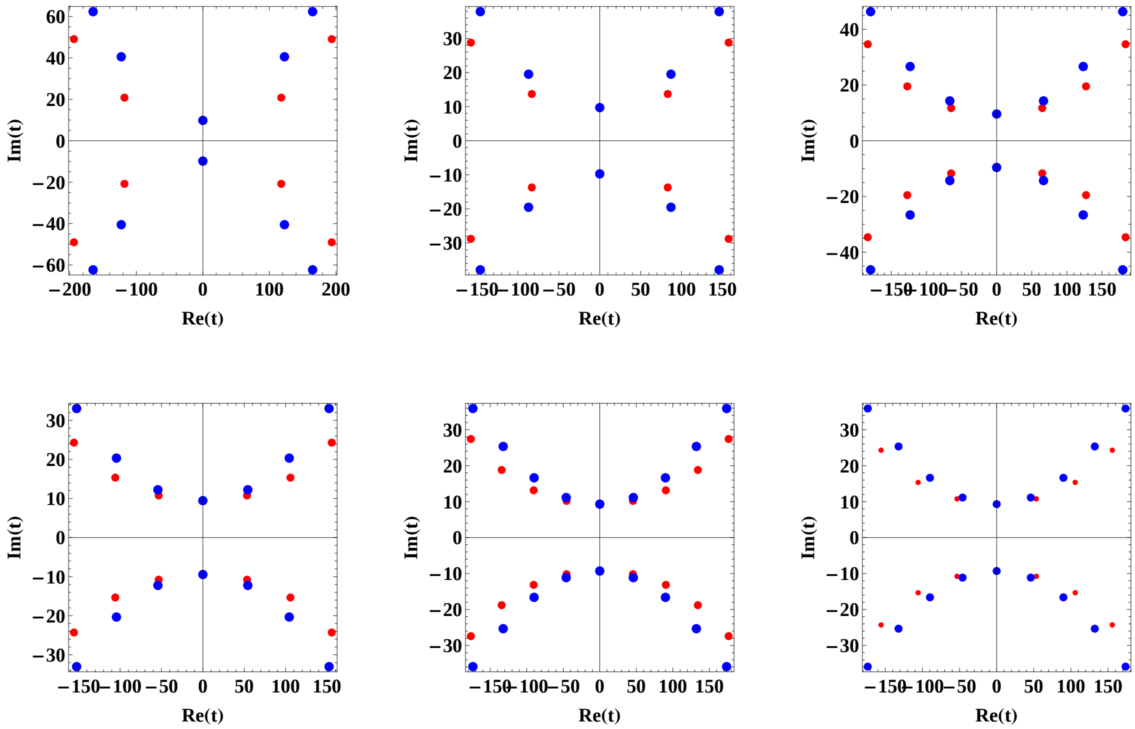

FIGURE 5.7: Turning points t_p in complex t-plane for the multi-sheeted Sauter (blue dots) and Gaussian pulses (red dots) with same number of subcycle oscillations. $\omega\tau$ =3, 4, 5, 6, and 7 from top right to bottom middle. The plot on the bottom left shows the turning points for Sauter pulse with $\omega\tau = 7$ and Gaussian pulse with $\omega\tau = 6$. Longitudinal momentum $p_3 = 0$ and transverse momentum $p_\perp = 0$. All units are expressed in electrons mass unit. The field parameters are $E_0 = 0.1$, $\tau = 100$, and the carrier-envelope offset phase $\phi = \pi/2$.

the real axis. Therefore, a closer look into the structures of the turning points in Fig. 5.7 for both pulses, will be able to shed light on the nature of the resulting momentum spectrum in the asymptotic region.

As mentioned earlier, for $p_3 = 0$ (and $p_\perp = 0$, considered for convenience), all the turning points are located on the imaginary axis for the single sheeted Sauter pulse. The separation between successive turning points is $\pi\tau$ which is enormous. The pair creation, therefore, is dictated by the single pair of turning point which is closest to the real axis and is given by $t_p = \tau \tanh^{-1}((\pm im - p_3)/eE_0\tau) = \pm 9.96687i$. Turning points for the corresponding Gaussian pulse are very close to those for the Sauter pulse, with the relevant pair closest to the real axis being $\pm 9.98339i$. Thus in both the cases, the asymptotic momentum spectrum has smooth unimodal profile. Since the turning point pair for the Sauter pulses is slightly closer to the real axis, the resulting momentum spectrum has somewhat larger peak value as seen is Fig. 5.3.

We present in Fig. 5.7 the turning points structures for multi sheeted pulses with $\omega\tau = 3$, 4, 5, 6 and 7 for the longitudinal momentum mode $p_3 = 0$. For the multi sheeted pulses, besides the central turning point pair on the imaginary axis, there are other pairs of turning points symmetrically located on either side of the imaginary axis. Although these turning points are located much closer to the real axis compared to the $n \neq 0$ turning points for the single sheeted pulses, for the values of $\omega\tau \leq 3$ they are still far-off to give any significant contribution to the reflection amplitude. As the value of $\omega\tau$ is increased, more pairs of turning points have comparable imaginary values of t, thereby giving rise to the possibility of the interference effects in the asymptotic reflection coefficient and hence the oscillatory pattern in the momentum spectrum of created particles. For the Gaussian pulse with $\omega\tau = 4$, there are two such pairs symmetrically located on either side of the central pair, at a distance of 83.1 unit along the real axis (note that the side bumps of the scattering potential also appear close to these locations , see Fig. 5.6). The distance of these turning points from the real axis is 13.7068 unit which is comparable to the distance of 9.7359 unit of the central pair. For the Sauter pulse, the corresponding additional turning point pairs are located at a distance of 19.5236 units which is more than twice the distance at which the central turning point pair is located. This explains the suppression of oscillations in the momentum spectrum for the Sauter pulse . It is only at $\omega\tau = 6$ that the non central turning point pairs are located at a distance (12.2396 units) from the real axis which is comparable to that for the central turning point pair. These turning points cause oscillations in the momentum spectrum. Appendix D contains detailed calculation of interference effect in the momentum spectrum which clearly brings out that the onset of oscillations for the Gaussian pulse takes place for $\omega\tau = 4$ whereas for the Sauter pulse, oscillations start at $\omega\tau = 6$.

For the same number of subcycle oscillations within the pulse duration the amplitude of oscillations in the momentum spectrum is larger for the Gaussian pule as the turning points causing the interference lie closer to the real axis in this case than those for the Sauter pulse. The turning point structure for the Gaussian pulse with $\omega\tau = 6$ and the Sauter pulse with $\omega\tau = 7$ are quite similar as shown in Fig. 5.7 (bottom right). This is consistent with the similarity of the scaled scattering potentials for the two pulses, as shown in Fig. 5.6 (bottom left) and also explains strong resemblance between oscillations in the respective momentum spectra (Fig. 5.5).

The central pair of turning points for the Sauter pulse is always slightly closer to the real axis than that for the Gaussian pulse. Therefore, unless the interference effect due to the other pairs of turning points becomes strong enough, the momentum spectrum for Sauter pulse has a higher peak value.

5.2.4 Momentum spectrum for Sauter and Gaussian pules with carrier-envelope offset phase

Thus far, the carrier-envelope offset phase ϕ is taken to be $\pi/2$ in order to match the maximum of oscillating electric field to the maximum of the temporal envelope. In this case, both Sauter and Gaussian pulses are nearly identical in the central part. Therefore, the overall profile and the centre of the momentum spectra discussed so far are quite similar for both the pulses. The noticeable difference for the two pulses in the non central region is reflected in the suppression of oscillations in the momentum spectrum for the Sauter pulse. For other values of ϕ, the maximum of the electric field is pushed away from the central region towards one of tail regions, making it asymmetrically distributed in the pulse envelope. It is expected that variation in ϕ will make the difference in the momentum spectra for the Sauter and Gaussian pulses more pronounced.

The dashed line of Fig. 5.8 shows the momentum spectrum of the created particles for the Sauter pulse with $\omega\tau = 5$ with the carrier-envelope offset phase $\phi = \pi/4$. The corresponding spectrum for Gaussian pulse was reported in Fig. 3 of Ref. [77]. In the spectrum for the Sauter pulse the oscillations are drastically suppressed, the peak value is lower, the width is larger and the centre is at $p_3 = -1.262$ MeV which results the corresponding kinetic momentum $P_3(\infty) = 357$ keV. Note that the spectrum for the Gaussian pulse has maximum kinetic momentum $P_3(\infty) = 102$ keV.

To understand the origin of these differences we plot vector potential for $\phi = \pi/4$ for both pulses as shown in Fig. 5.9(a). One can see from the plot of vector potential that the spectrum will be off-centred. The respective scattering potential is also shown Fig. 5.9(b). It is seen that the multiple bump structure for the Sauter pulse has less barrier height than the Gaussian pulse case. Therefore the reflection amplitudes from the side bumps of the Sauter pulse have comparatively less contribution and the resulting interference profile of the momentum spectrum at asymptotic time is less than the Gaussian one.

In Fig. 5.8, the momentum spectrum for the Sauter pulse with $\phi = 0$ should be compared with that reported for Gaussian pulse in Fig. 4 of Ref. [77]. All the aforesaid differences in the momentum spectra are once again seen here.

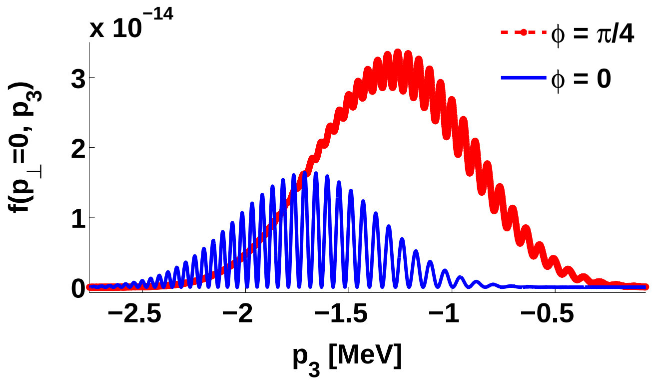

FIGURE 5.8: Asymptotic distribution function of the created particles in the presence of time dependent multi-sheeted Sauter pulse as a function of longitudinal momentum of the particles with different values of carrier-envelope offset phase (ϕ). The transverse momentum is considered to be zero and all the units are taken in electrons mass unit. The field parameters are $E_0 = 0.1$, $\tau = 100$, and $\omega = 0.05$.

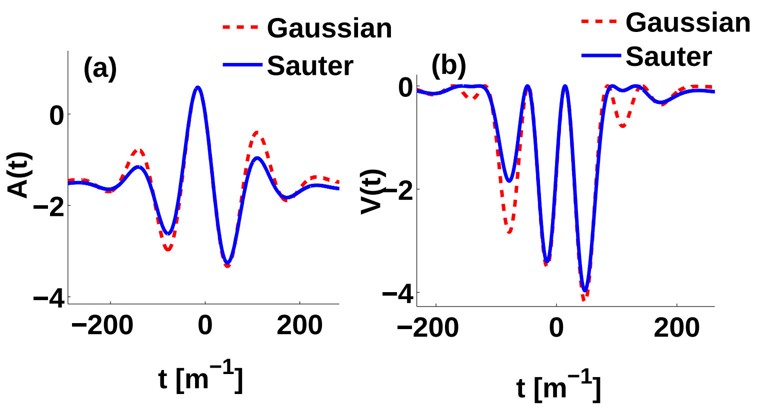

FIGURE 5.9: Plots of $A(t)$ and $V(t)$ for Gaussian (dashed line) and Sauter (line) with carrier-envelope offset phase $(\phi) = \pi/4$. The $V(t) = -(p_3 - eA(t))^2$ is plotted for the longitudinal momentum values $p_3 = -1.286$ for the Gaussian pulse and $p_3 = -1.262$ for the Sauter pulse. The transverse momentum is considered to be zero and all the units are taken in electrons mass unit. The field parameters are $E_0 = 0.1$, $\tau = 100$, and $\omega = 0.05$.

5.2.5 Momentum spectrum for Sauter and Gaussian pules with frequency chirping

The expression of the electric field for the ultrashort pulses with the linear frequency chirp parameter β is given by $E(t) = E_0 g(t) \sin(\omega t + \beta t^2 + \phi)$ with $g(t)$ being either a Gaussian or Sauter envelope. The presence of β modifies the frequency in a time dependent way – for negative times the effective frequency is lower while for positive times the effective frequency is higher. As discussed in the previous subsection the tail regions of the two pulse forms may differ significantly in presence of frequency chirping and hence give rise to different momentum spectrum of created particles at asymptotic times. In order to verify this claim, we plot the momentum spectrum as seen in Fig. 5.10 for multi-sheeted Sauter pulse with $\omega\tau = 5$ and the value of $\beta = 0.00025, 0.0005, 0.00075$. We compare our results with those obtained with the corresponding Gaussian pulse reported in Fig. 3 of Ref. [31]. For small value of linear chirp $\beta = 0.00025$, the asymptotic momentum spectrum for the Sauter pulse shows small oscillation induced over the smooth profile for negative value of p_3 the as seen in Fig. 5.10. For the Gaussian pulse, the oscillations in the spectrum are much more pronounced and the spectrum is not centred at $p_3 = 0$, see top left plot of Fig. 3 in Ref. [31]. As we increase the value of β, the shape of the distribution for the Sauter pulse remains intact although the oscillation amplitude gets enhanced. However, for the Gaussian pulse, it has been shown in [31] that the momentum spectrum becomes highly oscillating with irregular profile.

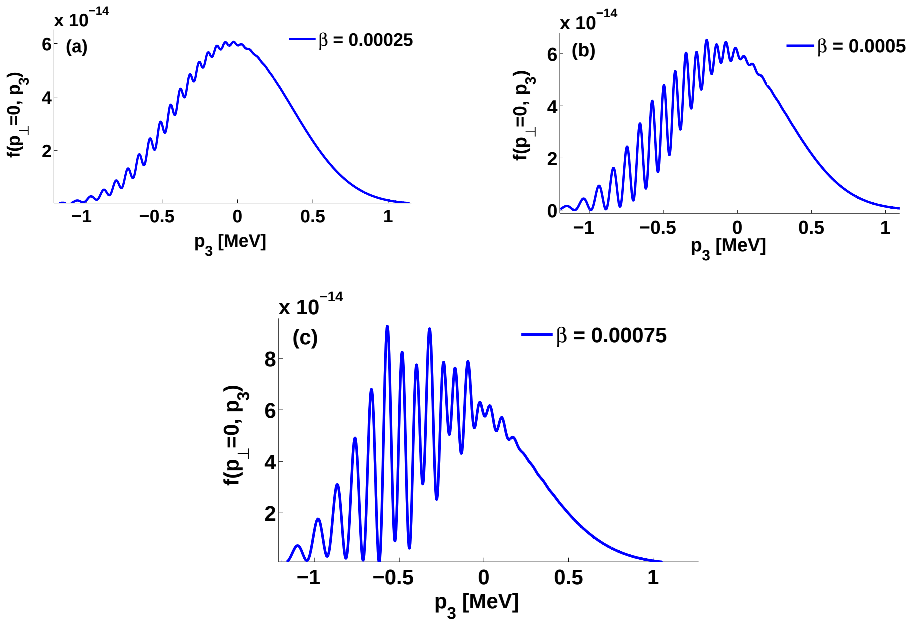

FIGURE 5.10: Asymptotic distribution function of the created particles in the presence of time dependent multi-sheeted Sauter pulse as a function of longitudinal momentum of the particles with different values of linear frequency chirp parameter (β). The transverse momentum of the created particle is taken as zero ($\mathbf{p}_\perp = 0$) and all the units are taken in electronic mass unit. The field parameters are $E_0 = 0.1$, $\tau = 100$, central frequency $\omega\tau = 5$ and carrier-envelope offset phase $\phi = \pi/2$.

5.3 Conclusion

To conclude, the effect of temporal pulse shape of intense ultrashort pulses on the momentum distribution of e^+e^- pairs is studied using quantum kinetic equation. It is shown that the distribution is quite sensitive to the temporal profile – to the extent that the two closely resembling temporal envelopes namely, Gaussian and Sauter with the same pulse parameters give rise to significantly different momentum spectrum of pairs at all the temporal stages of evolution. The temporal stages are classified, for convenience, into two distinct regions – transient and asymptotic regions. It is found that the transient region for the Gaussian pulse has larger temporal extent. In the transient region, the spectrum is smooth with a single peak for both the pulses. However the location of peak, the peak height and the width are different for any instant of time and they evolve differently with time. However the peak height for the Gaussian pulse is consistently higher than that for the Sauter pulse.

In the other regime, where the spectrum does not change with time, the peak position of the spectrum nearly coincides in both the cases. However, in the asymptotic region, just contrary to the trend in the transient region, the peak height of the spectrum for the Gaussian pulse is lower than that for the Sauter pulse as long as the number of subcycle oscillations, $\omega\tau < 5$. As reported in Ref. [20], the momentum spectrum for the multisheeted Gaussian shows oscillations over the smooth profile due to the quantum mechanical interference of the reflected quasi particle waves from bumpy time-dependent potential. These oscillation are suppressed in the case of Sauter pulse. The onset of oscillation takes place at $\omega\tau = 6$ for the Sauter pulse compared to $\omega\tau = 4$ for the Gaussian pulse. Furthermore, for the same value of $\omega\tau$ the amplitude of oscillation is smaller for the Sauter pulse. In fact, it is due to this interference effect that the peak height of the momentum spectrum for the Gaussian pulse takes over that for the Sauter pulse for $\omega\tau \geq 5$. The sensitivity of the momentum spectrum to the temporal pulse forms is explained by analyzing the shape of potential causing over barrier reflections and also the turning point structure in complex time plane for the two pulse forms.

The differences in the asymptotic time spectrum of the two pulses get much more prominent on increasing the linear frequency chirp in these pulses and also on varying the CEP. Furthermore, the profile and the location of the spectrum is vastly different for the two pulses.

Although it may appear somewhat far fetched, measuring momentum spectrum of the pairs may provide a possible method for the determination of the temporal profile for ultrashort pulses.

Chapter 6

Field induced phase transition and entropy production

The production of particle-antiparticle pairs from the vacuum fluctuation in a time-dependent electric field $E(t)$ was seen as a field induced phase transition (FIPT) via the t-non invariant vacuum state because of the non-stationary Hamiltonian [49]. Here, the spontaneous symmetry breaking of the vacuum state takes place under time inversion and consequently electron-positron pairs are generated which are the massive analogue of Goldstone bosons [80]. In order to quantify this symmetry breaking one defines a complex order parameter $\Phi(\mathbf{p}, t) = 2 < 0_{in}|a^\dagger_{\mathbf{p}}(t)b^\dagger_{-\mathbf{p}}(t)|0_{in} >= |\Phi(\mathbf{p}, t)| \exp(i\psi(\mathbf{p}, t))$ [32, 49, 58] where $a^\dagger_{\mathbf{p}}(t)$, $b^\dagger_{-\mathbf{p}}(t)$ are creation operators of particle and antiparticle with momentum $\pm\mathbf{p}$, respectively, in the quasi-particle representation in the time dependent basis. FIPT was studied for the single and multi-sheeted electric pulses [32, 49, 58]. It was shown that the evolution of the modulus of order parameter $|\Phi(\mathbf{p}, t)|$ brings out three distinct stages/ phases namely the quasi-electron positron plasma (QEPP) stage, the transient stage and the final residual electron positron plasma stage (REPP). The effect of sub-cycle field oscillations on these stages was also studied for different longitudinal momentum values [58, 59]. However the evolution of the phase of the complex order parameter, to the best of our knowledge, has not been studied so far. We use quasi-particle representation of quantum kinetic formalism (QKE) [32, 55–57, 63, 78] for the evolution of the quasi-particle vacuum in the presence of a time dependent electric field under the mean field approximation (neglecting the collisional effects of the created particles and back reaction force on the external electric field).

In this **Chapter**, we study the evolution of the modulus and the phase of $\Phi(\mathbf{p}, t)$ and analyse their interrelation. Frequency chirp is an essential and integral part of ultrashort laser pulses.

The frequency chirping changes the time period of subcycle oscillations of the external electric field which further induces complexity in the evolution of the order parameter. We analyse this complexity as a function of linear and quadratic frequency chirp parameters.

The rest of the chapter is organized as follows: in Sec. 6.1 we briefly discuss FIPT and introduce the complex order parameter. The effect of frequency chirping in the evolution of the order parameter is discussed in Sec. 6.2. We discuss the evolution of entropy production in Sec. 6.3. Finally we conclude in Sec. 6.4. The technical details of the derivation of the evolution equation are relegated to **Appendix** E.

6.1 Kinetic equations for evolution of order parameter

Using the quantum kinetic equations in the form of 3-coupled ordinary differential equations [32, 63, 81] for the single particle distribution function $f(\mathbf{p},t) =< 0_{in}|a^\dagger_{\mathbf{p}}(t)a_{\mathbf{p}}(t)|0_{in} >=< 0_{in}|b^\dagger_{-\mathbf{p}}(t)b_{-\mathbf{p}}(t)|0_{in} >$ and the real and imaginary parts of the order parameter $u(\mathbf{p},t) = |\Phi(\mathbf{p},t)|\cos\psi(\mathbf{p},t)$ and $v(\mathbf{p},t) = |\Phi(\mathbf{p},t)|\sin\psi(\mathbf{p},t)$ respectively, we get the following nonlinear coupled differential equations for the evolution of the modulus $|\Phi(\mathbf{p},t)|$ and the phase $\psi(\mathbf{p},t)$ of the order parameter, see **Appendix** E for the technical details of the derivation.

$$\begin{aligned} \frac{d|\Phi(\mathbf{p},t)|}{dt} &= \frac{eE(t)\epsilon_\perp}{2\omega^2(\mathbf{p},t)}\cos\psi(\mathbf{p},t)\sqrt{1-|\Phi(\mathbf{p},t)|^2}, \\ \frac{d\psi(\mathbf{p},t)}{dt} &= 2\omega(\mathbf{p},t) - \frac{eE(t)\epsilon_\perp}{\omega^2(\mathbf{p},t)}\sin\psi(\mathbf{p},t)\frac{\sqrt{1-|\Phi(\mathbf{p},t)|^2}}{|\Phi(\mathbf{p},t)|}. \end{aligned} \tag{6.1}$$

$u(\mathbf{p},t)$ and $v(\mathbf{p},t)$ govern the vacuum polarization and the counter process of pair production i.e., pair annihilation, respectively. The terms $\omega(\mathbf{p},t) = \sqrt{m^2 + p_\perp^2 + P_3^2(t)}$ and $P_3(t) = p_3 - eA(t)$ are the quasi-energy and the longitudinal quasi-momentum respectively of the quasi-particle. The particle acceleration is governed by $dP_3(t)/dt = eE(t)$ in the presence of the time dependent electric field $E(t)$; e is the electronic charge; $\epsilon_\perp = \sqrt{m^2 + \mathbf{p}_\perp^2}$ is the transverse energy.

The electric field in this study is taken as the multi-sheeted Sauter pulse which is considered to describe well the resultant field of counter propagating ultrashort laser pulses in the focal region.

$$E(t) = E_0\cosh^{-2}(t/\tau)\cos(\alpha t^3 + \beta t^2 + \omega_0 t), \tag{6.2}$$

where β and α are the linear and quadratic frequency chirp parameters respectively; ω_0 is the central frequency of the laser electric field oscillation with τ being the total pulse length. Single sheeted Sauter pulse corresponds to $\alpha = \beta = \omega_0 = 0$.

6.2 Results and discussions

We solve Eq. 6.1 numerically for the evolution of $|\Phi(\mathbf{p}, t)|$ and $\psi(\mathbf{p}, t)$ with the initial condition $|\Phi(\mathbf{p}, t \to \infty)| = 0$. The phase $\psi(\mathbf{p}, t)$ is defined only up to an arbitrary additive constant. For definiteness we begin at $t = -10\tau$ with $|\Phi(\mathbf{p}, t = -10\tau)| = 10^{-16}$ and $\psi(\mathbf{p}, t = -10\tau) = \pi/4$ so as to have $u = v = 10^{-16}/\sqrt{2}$ initially.

The complete evolution of the modulus of the order parameter $|\Phi(\mathbf{p}, t)|$ was shown to go through three distinct stages namely initial quasi-electron positron plasma (QEPP) stage, transient stage, and final residual electron-positron plasma (REPP) stage of the created electron-positron pairs by the external time dependent electric field of single sheeted Sauter pulse and multi-sheeted Gaussian pulse [58, 59]. As the evolution of the phase $\psi(\mathbf{p}, t)$ has not been studied so far, we revisit these cases. $|\Phi(\mathbf{p}, t)|$ and $\psi(\mathbf{p}, t)$ are plotted as function of time for single and multi-sheeted Sauter pulses without any frequency chirp ($\omega_0\tau = 5, \alpha = \beta = 0$). It is seen that $|\Phi(\mathbf{p}, t)|$ increases linearly in time in QEPP region for the single-sheeted Sauter pulse up to $t = 0$ at which electric field reaches maximum value and thereafter $|\Phi(\mathbf{p}, t)|$ decreases. Then $|\Phi(\mathbf{p}, t)|$ undergoes rapid oscillations and makes the transition from QEPP to a transient region then finally to REPP state as a consequence of FIPT wherein $|\Phi(\mathbf{p}, t)|$ reaches a constant value different from zero. The phase $\psi(\mathbf{p}, t)$ remains almost constant before increasing rapidly about the time the transient stage in the evolution of $|\Phi(\mathbf{p}, t)|$ appears. For the multi-sheeted Sauter pulse the evolution of $|\Phi(\mathbf{p}, t)|$ shows periodic oscillations corresponding to the subcycle structure of the electric field in the QEPP region. The transient region appears later and becomes elongated before it reaches final REPP state.

As seen in Eq. 6.1 the evolution of $|\Phi(\mathbf{p}, t)|$ is governed by the temporal profiles of the electric field $E(t)$ and the corresponding vector potential $A(t)$ through the ratio $\frac{E(t)}{\omega^2(\mathbf{p},t)}$ (Note that $\epsilon_\perp = e = 1$) and also by the phase term $\cos\psi(\mathbf{p}, t)$. As $\psi(\mathbf{p}, t)$ remains nearly constant, the QEPP stage is largely controlled by $E(t)/\omega^2(\mathbf{p}, t)$ as seen the Fig. 6.1. For the single-sheeted pulse as shown in Fig. 6.2 the electric field profile is smooth having its maximum at $t = 0$ while the vector potential is large in magnitude on the either side of the electric field maximum resulting in a sharper temporal profile of $E(t)/\omega^2(\mathbf{p}, t)$. In Refs. [58, 59] the temporal profile of $|\Phi(\mathbf{p}, t)|$ in the QEPP stage was compared to that of $|E(t)|$. However, the much sharper profile of $|\Phi(\mathbf{p}, t)|$, particularly near the centre of the pulse, and the faster decay thereof in the tail regions is better explained by $|E(t)|/\omega^2(\mathbf{p}, t)$ than $|E(t)|$, see the upper panel of Fig. 6.2. The formation of the transient region takes place because of the sudden increase in the value of the phase $\psi(\mathbf{p}, t)$ which makes $\cos\psi(\mathbf{p}, t)$ (on the right hand side of Eq. 6.1) and hence $|\Phi(\mathbf{p}, t)|$ oscillate rapidly. Once the electric field gets vanishingly small resulting in a constant value of $|\Phi(\mathbf{p}, t)|$

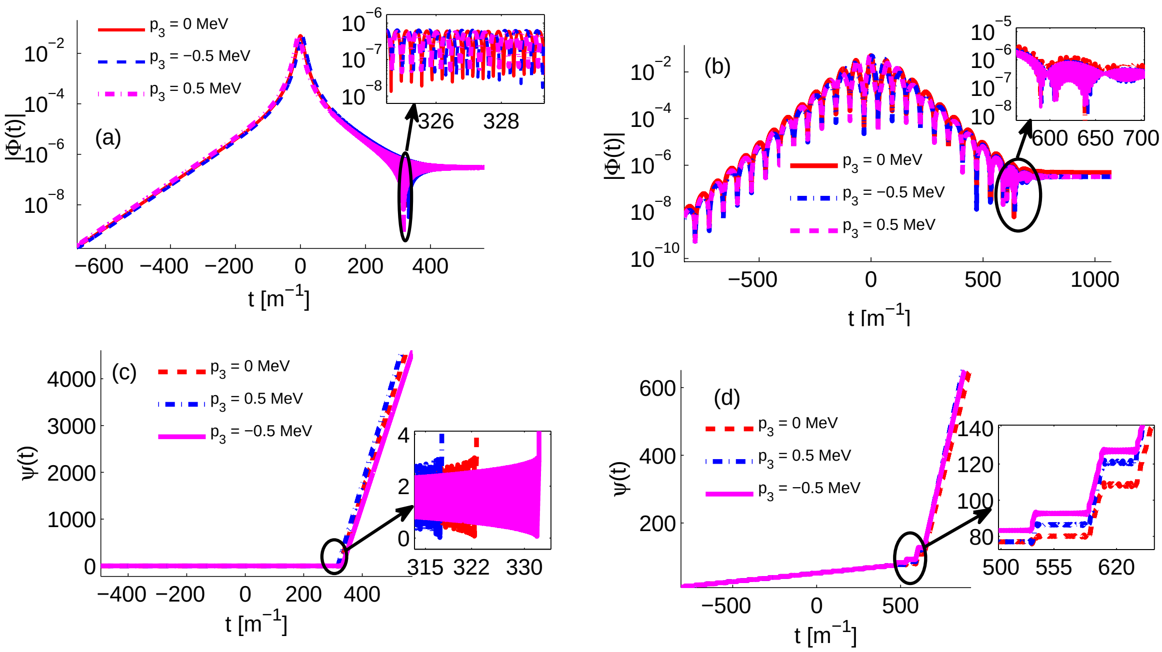

Figure 6.1: Evolution of the modulus $|\Phi(t)|$ and the phase $\psi(t)$ of the order parameter for a time dependent (a) and (c) single-sheeted Sauter pulse;(b) and (d) multi-sheeted ($\omega_0\tau = 5$) Sauter pulse without frequency chirping ($\alpha = \beta = 0$). All the units are taken in electron mass unit. The field parameters are $E_0 = 0.1$, and $\tau = 100$. The insets show magnified view of the evolution in the transient region.

in the REPP region. In this region $d\psi(\mathbf{p}, t)/dt = \omega t$ and hence $\Phi(\mathbf{p}, t) \sim \Phi_R e^{i\omega t}$ where Φ_R is the constant value of $\Phi(\mathbf{p}, t)$. For the multi-sheeted pulse, as shown in the top left panel of the Fig. 6.2 (dashed line), the electric field oscillates within the smooth envelope. In contrast to the single sheeted field case, the vector potential is much suppressed in the tail region of the field having oscillatory structure in the centre (top-middle panel of Fig. 6.2). The resulting $E(t)/\omega^2$ has a temporal profile close that of $E(t)$, except near the pulse centre. The QEPP region is consequently broader and the temporal profile of $|\Phi(\mathbf{p}, t)|$ in this region is modified by the subcycle structures of the electric field. In this case too, the temporal profile of $|\Phi(\mathbf{p}, t)|$ in the QEPP stage is well explained by that of $|E(t)|/\omega^2(\mathbf{p}, t)$. The rapid oscillation of $|\Phi(\mathbf{p}, t)|$ in the transient region in this case is governed by the oscillations in $E(t)$, $\cos\psi(\mathbf{p}, t)$ and $A(t)$, therefore the transient region elongated and the modulation effect is seen in the top right panel of Fig. 6.1. In the QEPP region, the counter term $v(\mathbf{p}, t)$ governing the depolarization/ pair annihilation is stronger than the term $u(\mathbf{p}, t)$ which is responsible for the polarization/ pair creation. Both $u(\mathbf{p}, t)$ and $v(\mathbf{p}, t)$ oscillate with varying amplitudes which is large in the centre of the pulse. The decrease in amplitude of $v(\mathbf{p}, t)$ in moving away from the centre is more than that of $u(\mathbf{p}, t)$. In the transient region both the amplitudes are nearly same, before becoming identical in the REPP stage.

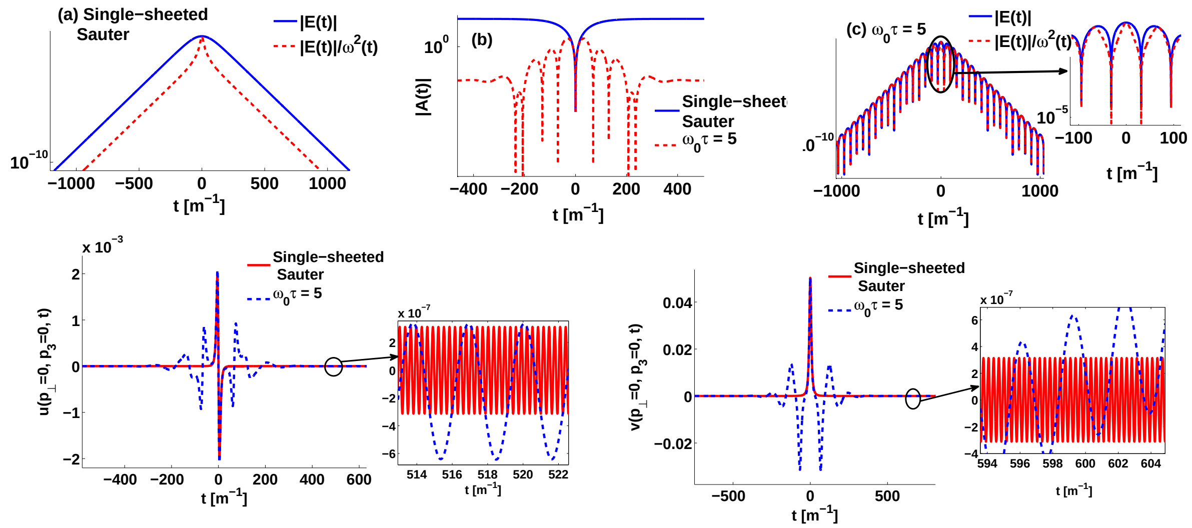

FIGURE 6.2: Plots of time dependent electric field $|E(t)|$ and $|E(t)/\omega^2(\mathbf{p}, t)|$ for single sheeted Sauter (top left); for multi sheeted Sauter pulse (top right); the vector potential $|A(t)|$ for single and multi sheeted Sauter pulses (top middle); real part of order parameter $|u(t)|$ (bottom left) and imaginary part of order parameter $|v(t)|$ (bottom right) for single-sheeted and multi-sheeted Sauter pulses. All the units are taken in electron mass unit. The field parameters are $E_0 = 0.1$, $\tau = 100$, the central frequency of the pulse $\omega_0 = 0.05$, and linear and quadratic frequency chirp parameters $\beta = \alpha = 0$. Transverse and longitudinal momenta are taken to be zero.

6.2.1 Effect of frequency chirping on field induced phase transition

It is clear from the results discussed so far the complexity in the evolution of the modulus and the phase of the order parameter, particularly in the transient stage, is because of the non linear coupling in the dynamical equations governing the evolution of the modulus and the phase. As demonstrated above, in the QEEP region, the evolution of modulus is mostly governed by both electric field $E(t)$ and vector potential $A(t)$. The evolution of the phase, on the other hand, is governed by two distinct terms which contain all the dynamic behaviour. In the QEEP stage, where the phase evolves slowly and smoothly, the two terms seem to balance each other. The transient stage arises when this dynamic balance is lost and hence there is steep increase in the phase over a very small duration. After the transient stage, the dynamics of the phase and modulus of the order parameter are decoupled.

The presence of frequency chirping, in effect makes frequency time dependent. This, in turn affects the number of subcycle oscillations within the envelope. In the presence of linear frequency chirp β, the subcycle oscillations are asymmetric about $t = 0$. As we have taken the positive value of β, the number of oscillations within the pulse envelope is lesser for $t < 0$ than that for $t > 0$. Hence the evolution of $|\Phi(\mathbf{p}, t)|$ shows irregular oscillations in the QEPP state

(Fig. 6.3). As β is increased further the oscillations become faster and are spread throughout the QEPP region as seen in the bottom left plot of Fig. 6.3. The evolution can qualitatively be understood by looking at the temporal profiles of $E(t)$, $A(t)$ and also the ratio $|E(t)/\omega^2(\mathbf{p},t)|$ as shown in Fig. 6.4. The linear frequency chirping makes the electric field asymmetric about

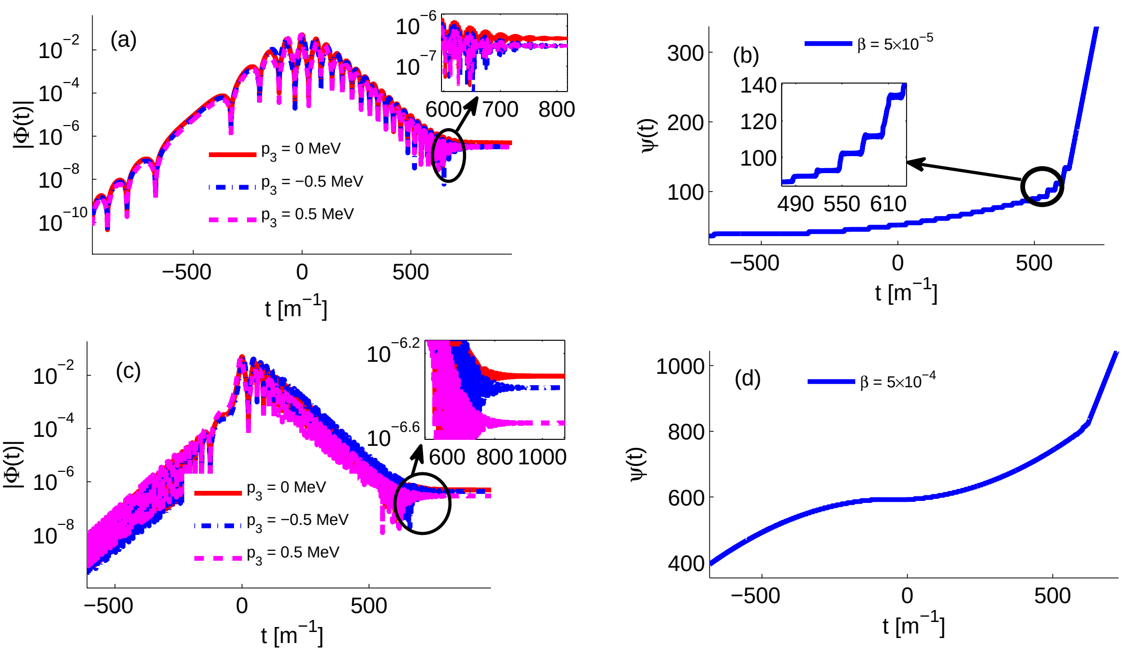

FIGURE 6.3: Evolution of $|\Phi(t)|$ and $\psi(t)$ for a time dependent multi-sheeted Sauter pulse with $\omega_0\tau = 5$ and different values of linear frequency chirping parameter β. The other parameters are same as in Fig. 6.1.

$t = 0$ and as we consider the positive value of β, the subcycle oscillation is more in $t > 0$ than $t < 0$. For $\beta = 5 \times 10^{-5}$, the effect of frequency chirping is small. Hence the evolution of $|\Phi(\mathbf{p},t)|$, as in the case of multi sheeted Sauter pulse discussed above, follows the electric field profile in QEPP stage and the transient stage is marked by the sudden change in the evolution of the phase. For $\beta = 5\times10^{-4}$, however, there is much more asymmetry in the electric field profile and the vector potential is large and constant for $t < 0$, before undergoing quick oscillations near $t = 0$ and attaining a constant value thereafter. The evolution of $|\Phi(\mathbf{p},t)|$ with enhanced oscillation frequencies in the QEPP stage follows the temporal profile of $|E(t)/\omega^2(\mathbf{p},t)|$.

Now we consider the effect of the linear chirp β in the presence of quadratic chirp $\alpha = 1 \times 10^{-6}$. Here for small values of β, the inequality $\omega_0 > \alpha\tau^2 > \beta\tau$ holds and the effect of α dominates the evolution of $|\Phi(\mathbf{p},t)|$. The evolution shows the formation of a pre-transient region in the QEPP region for values of $t < 0$ (before the electric field reaches its maximum value E_0). This is shown in the top panel of Fig. 6.5. However this region gets suppressed for higher values of β to give the uninterrupted QEPP region with irregular, fast and spread

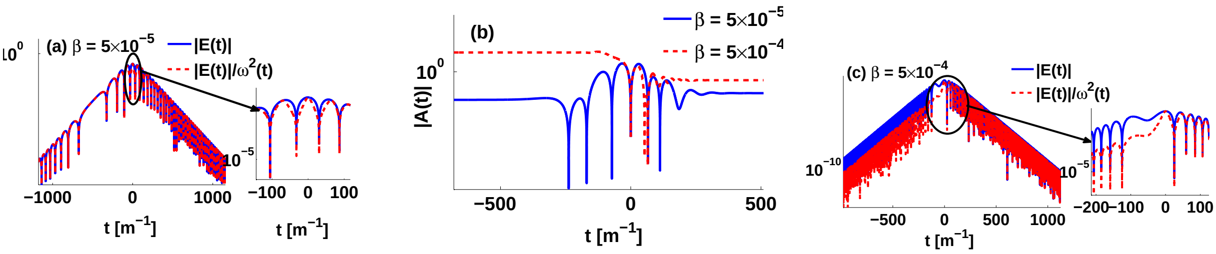

FIGURE 6.4: Plots of $|E(t)|$, $|E(t)|/\omega^2(t)$ and $|A(t)|$ for multi-sheeted Sauter pulse for the linear frequency chirp parameter $\beta = 5 \times 10^{-5}$ and 5×10^{-4} with $\alpha = 0$. Others parameters are same as in Fig. 6.2.

out oscillations as seen in Fig. 6.5(c)-(d). It is seen that for higher values of β, the formation of REPP stage takes place with larger magnitude of the order parameter for $p_3 = -0.5$ MeV mode than $p_3 = 0.5$ MeV. The effect of only quadratic chirping is shown in Fig. 6.7 for

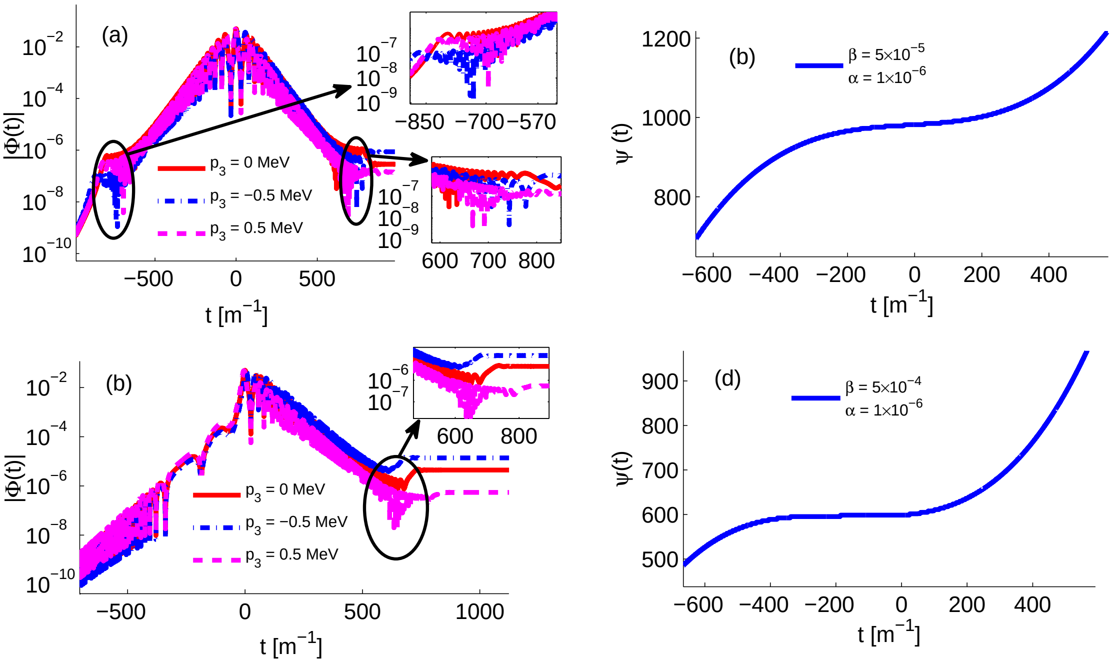

FIGURE 6.5: Evolutions of $|\Phi(t)|$ and $\psi(t)$ for a time dependent multi-sheeted Sauter pulse with $\omega_0\tau = 5$ and different values of linear frequency chirping parameter β with a quadratic frequency chirping, $\alpha = 1 \times 10^{-6}$. The other parameters are same as in Fig. 6.1.

the longitudinal momentum values $p_3 = 0$ MeV and $p_3 = \pm 0.5$ MeV. For $\alpha = 5 \times 10^{-7}$ the evolution of $|\Phi(\mathbf{p}, t)|$ shows high frequency oscillations in QEPP stage, see top panel of Fig. 6.7. There is no formation of the pre-transient region in this case. However, if the value of α is increased to $\alpha = 5 \times 10^{-6}$ the formation of pre-transient region takes place which is seen in the bottom panel of Figs. 6.7. Furthermore, the pre-transient and the transient regions are shifted towards the maximum of the electric field *i.e.* towards $t = 0$. Higher the value of α

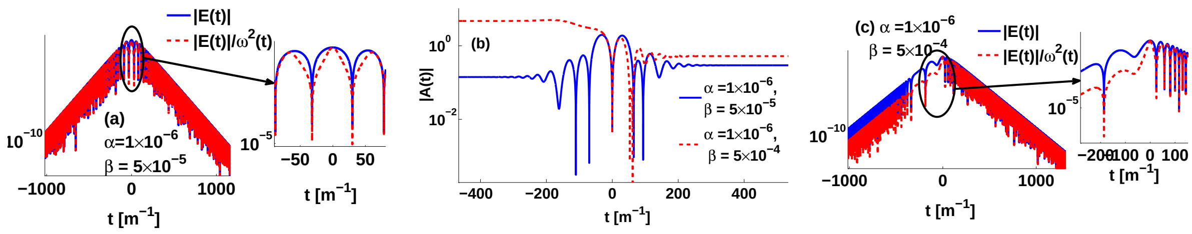

FIGURE 6.6: Plots of $|E(t)|$, $|E(t)|/\omega^2(t)$ and $|A(t)|$ for multi-sheeted Sauter pulse for linear frequency chirp parameter $\beta = 5 \times 10^{-5}$ and 5×10^{-4} with $\alpha = 1 \times 10^{-6}$. Others parameters are the same as in Fig. 6.2.

larger is the shift. Consequently the formation of REPP state takes place earlier as the value of α is increased. The magnitude of the order parameter in the REPP region also increases with increase in the value of α and results in the formation of final electron-positron state with higher correlation. Moreover, the clear separation for different momentum modes can be seen in the pre-transient and transient stages of evolution of order parameter. In order to understand the

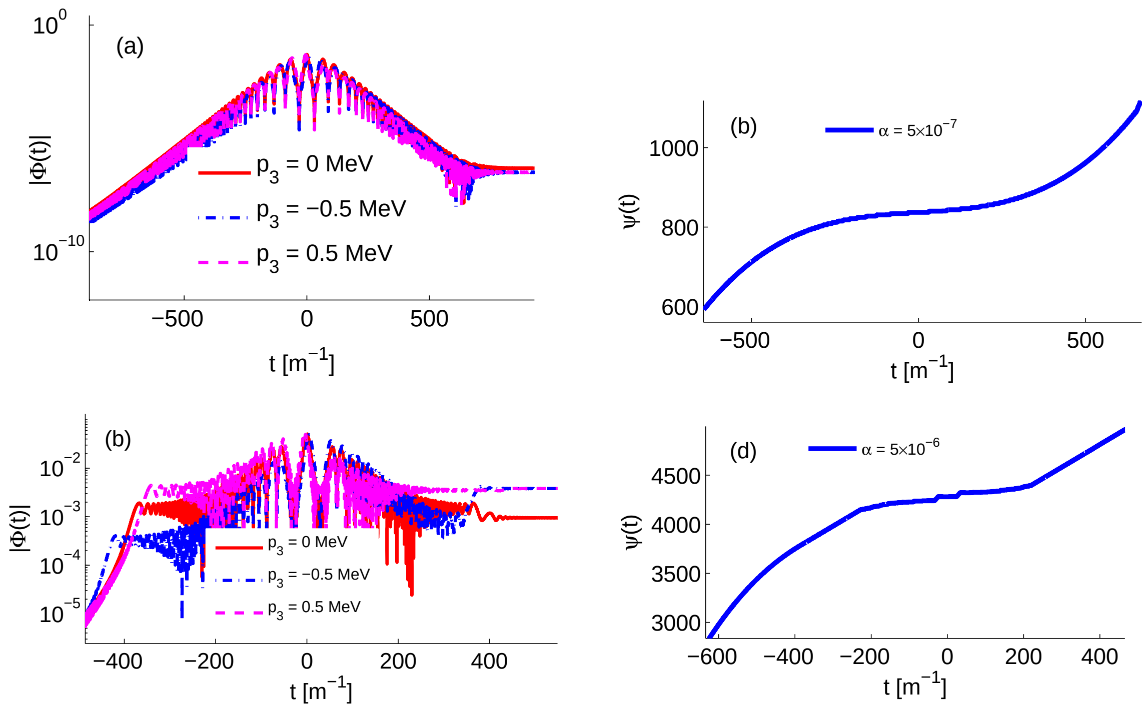

FIGURE 6.7: Evolutions of $|\Phi(t)|$ and $\psi(t)$ for a time dependent multi-sheeted Sauter pulse with $\omega_0\tau = 5$ and different values of quadratic frequency chirping parameter α without linear frequency chirping. The other parameters are same as in Fig. 6.1.

complex evolution of the order parameter we look at the temporal pulse profile of the electric field and the corresponding vector potential. We present $E(t)$ and $A(t)$ for $\alpha = 5 \times 10^{-7}$ and 5×10^{-6} in Fig. 6.8. The subcycle oscillations within the pulse envelope make the evolution of order parameter complicated. The presence of only quadratic frequency chirping makes the electric field symmetric and the vector potential antisymmetric about $t = 0$. For $\alpha = 5 \times 10^{-7}$, the effect of the frequency chirping is less in the electric field dominated regimes and it shows regular oscillation. But for $\alpha = 5 \times 10^{-6}$, the electric field exhibits more oscillations which makes the dynamics of order parameter complex through $E(t)$ and $\omega(\mathbf{p}, t)$.

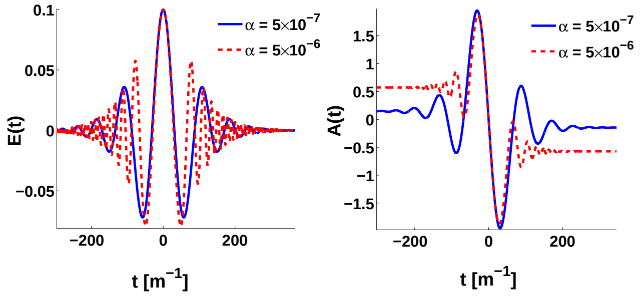

FIGURE 6.8: Plots of $E(t)$ and $A(t)$ for multi-sheeted Sauter pulse for the quadratic frequency chirp parameter $\alpha = 5 \times 10^{-7}$ and 5×10^{-6} with $\beta = 0$. Others parameters are the same as in Fig. 6.2

6.3 Entropy production

Electron-positron pair production in the presence of a time dependent electric field is viewed as a field induced phase transition going through various stages of evolution. Study of pair production from such a point of view provide an opportunity to address the fundamental question as to how irreversible observable behaviour can arise when the underlying dynamics is reversible at the microscopic level. There have been related studies in the area of heavy-ion collisions and quantum chromodynamics [82]. In the context of pair production in presence of an external field irreversibility and entropy production were described in terms of time scales, such as memory time and production time [57]. Kluger *et al.* have related the evolution of entropy to identification of "relevant" and "irrelevant" dynamical variable [83]. Evolution of entropy for single sheeted Sauter pulse was studied in Ref. [58]. Here we present results for the evolution of entropy for pair production due to some of the pulses considered above and try to find possible connection between the evolution of order parameter and the entropy production.

The single particle momentum distribution function $f(\mathbf{p}, t)$ defined earlier is used to define the entropy density of the quantum system by the von-Neuman formula

$$S(t) = -g \int \frac{d^3 p}{(2\pi)^3} [f(\mathbf{p}, t) \ln f(\mathbf{p}, t) + (1 - f(\mathbf{p}, t)) \ln(1 - f(\mathbf{p}, t))]. \tag{6.3}$$

Here g is the spin degeneracy factor which equals to two for the spin-$1/2$ particles. The single particle distribution function f can be expressed in terms of the modulus of the order parameter using the first integral of motion given in Appendix E. However, the phase of the order parameter does not appear in the definition of entropy density and in this sense it is an irrelevant variable. Thus the loss of phase information can be related to monotonic increase in the entropy.

We solve Eq. 6.3 numerically for the time dependent multi sheeted Sauter pulse with different values of $\omega\tau$ parameter. We use all the units in electron mass unit and assume $\hbar = c = e = m = k_B = 1$.

The evolution of entropy density of the quantum system is shown in Fig. 6.9 as consequence of vacuum particle antiparticle pair production. In Figs. 6.9(a)-(d) we choose the value of $\omega\tau = 4, 5, 6,$ and 7 in the sub-cycle structure of the Sauter pulse. Such inclusion of the sub-cycle structure of the Sauter pulse modifies the temporal evolution of the entropy density of the created particle-antiparticle pairs. The entropy evolution has two distinct regions. In the

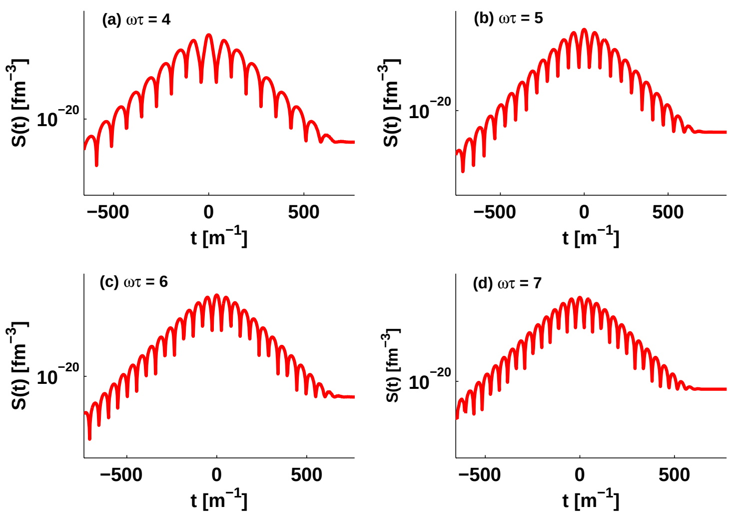

FIGURE 6.9: Evolution of the entropy density in the presence of time dependent multi-sheeted Sauter pulse with different values of $\omega\tau$ parameter. From top left to bottom right the values of $\omega\tau$ parameter are taken as $4, 5, 6,$ and 7. The field parameters are $E_0 = 0.1$, $\tau = 100$ in electron mass unit.

first one has non monotonic growth of entropy. This matches with the QEPP stage of the time evolution of the modulus of the order parameter and hence the single particle distribution function. As discussed earlier, for multi sheeted pulses the evolution is largely governed by the electric field for all the momentum modes. In fact the evolution matches with the temporal profile of $|E(t)|$. In entropy, all momentum modes add to again give the profile of $|E(t)|$ in the QEPP region and hence resulting in its non monotonic increase. In the transient region, because of abrupt increase in the phase of order parameter, the single particle distribution function undergoes rapid oscillations which get washed out when summed over many momentum modes to give a constant non zero value of entropy as a result of decoherance. In the QEEP region the dynamics is non Markovian, whereas from the transient region onwards it is irreversible and Markovian.

In order to establish the connection between the evolutions of entropy and the order parameter modulus we present the evolution of entropy for the Sauter pulses with frequency chirp. It is clear that all the complexities of the evolution of the order parameter modulus are also seen in the evolution of entropy. The appearance of a small flat region corresponding to the pre-transient region is also seen (Fig. 6.10).

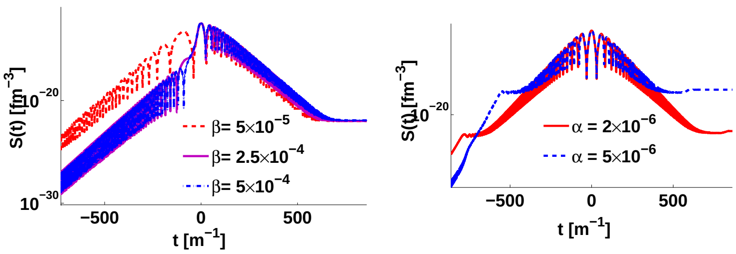

FIGURE 6.10: Evolution of the entropy density in the presence of time dependent multi-sheeted Sauter pulse with frequency chirping. The field parameters are $E_0 = 0.1$, $\tau = 100$ in electron mass unit.

In the end, we consider a combination of two Sauter pulses which are temporally delayed. We use the form of the electric field and vector potential given in [76] as:

$$E(t) = E_0 \cosh^{-2}(\omega(t - T/2)) - E_0 \cosh^{-2}(\omega(t + T/2)), \tag{6.4}$$

(antisymmetric configuration) and

$$A(t) = \frac{E_0}{\omega}\{1 + \tanh(\omega(t - T/2)) - \tanh(\omega(t + T/2))\}. \tag{6.5}$$

Fig. 6.11 it is once again clear that in the QEPP region evolutions of entropy and the order parameter modulus have very similar temporal profile.

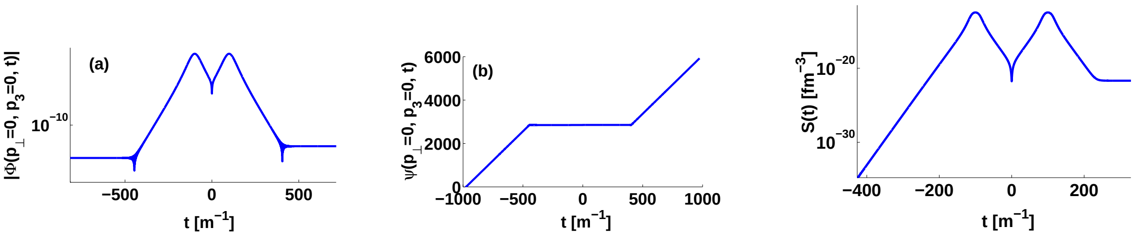

FIGURE 6.11: Evolutions of the $|\Phi(\mathbf{p}, t)|$, $\psi(\mathbf{p}, t)$, and entropy density in the presence of time dependent single-sheeted two Sauter pulses with delayed in time. The field parameters are $E_0 = 0.1$, $\omega = 0.04$, the delay time $T = 200.2$. All units are in electron mass unit.

6.4 Conclusion

To conclude, we have studied the evolution of the complex order parameter which defines the particle-antiparticle correlation due to the vacuum fluctuation in the presence of a multi-sheeted Sauter pulse with frequency chirping. We have considered the both linear and quadratic frequency chirping parameters for the evolution of the complex order parameter for the longitudinal momentum values $p_3 = 0$ MeV, ∓ 0.5 MeV. The evolution stages of the order parameter which undergoes quasi-electron positron plasma oscillation to residual electron-positron plasma stage via the highly non-linear transient region get modified by the frequency chirping of the electric field. In general, the quasi-electron positron plasma state gets modulated by the frequency chirping and the formation of the pre-transient region is seen in the evolution of the order parameter in the presence of quadratic frequency chirping. In the second section, we have studied the evolution of the entropy for the time dependent Sauter pulse sub-cycle pulse oscillations, frequency chirping and time delay. The evolution of the entropy density, in each case was shown to match with that of the order parameter modulus in the QEEP region. The instantaneous increase or decrease in entropy signifies some counter effect of the pair production *i.e.* the pair annihilation process. The monotonic increase in entropy in the transient region and onwards is attributed to the dephasing in the particle anti-particle correlation function.

Chapter 7

Conclusion and outlook

In this chapter, we first summarise the major outcomes of our work based on the studies of electron-positron pair production via Schwinger mechanism by ultrastrong and ultrashort laser electromagnetic (EM) field in the thesis. We have structured our work mainly in two domains, first the geometrical control of focused laser EM field for the production of electron-positron pairs at the focus and second to study the dynamics of the created particle-antiparticle pairs from the single particle distribution function using kinetic theory approach. We have neglected the spin effects of the created particles. First portion of our studies deals with the dependence of local pair production rates in longitudinal coordinate (along the laser pulse propagation) and time on the spatiotemporal structure of the invariant electric and magnetic fields. We have seen that the spatial focusing of the EM field makes it necessary to specify the beam polarization parameter, which determines the transverse and longitudinal component of the generalized focused beam. We have found that the localized particle bunches along the longitudinal direction (propagation direction) are produced by the circularly e- or h- polarized colliding pulses. The colliding pulses made up of equal mixture of e- and h-wave produces ultrashort particle bunches. Carrier envelope phase (CEP) is an important parameter for Ultrashort laser pulses. We find that it influences spatio temporal distribution of pairs. For linearly e-polarized colliding laser pulses, there is zone formation of the invariant electric and magnetic fields. Depending on the value of CEP we get unimodal or bimodal temporal distribution of created pairs. When the colliding circularly e-polarized pulses have same sense of rotation, CEP has no effect on the spatiotemporal distribution of pairs. However, when the pulses have opposite sense of rotation CEP controls the temporal distribution of pairs. We find that colliding pulses with relative phase difference give rise to spiky spatiotemporal distribution of the invariant field in the focal region. Thus the relative phase can be used to control the spatiotemporal distribution of the created pairs by the pulses with linear or circular polarizations. We predict that the total pair production is maximal when one of the spikes in the invariant electric field distribution is located near the center of the spatiotemporal envelope (and distribution of created pairs looks approximately unimodal), and minimal when the neighboring spikes are off-centered but located symmetrically. The particular phase shifts required for each case depend on polarization of the pulses. Among the considered cases, for the parameters adopted here the global maximum is achieved with a circularly polarized pulses with same sense of rotation as considered in Ref. [15].

Possibility of phase control of Schwinger pair production under discussion may be useful, e.g., to increase the attainable intensity of tightly focused colliding laser pulses by reducing pair production and hence preventing field depletion at their crossing, or, conversely, to measure the typically unknown field structure and phase relations of extremely strong laser pulses in a way similar to proposed in Ref. [42] by using the multiphoton Compton scattering.

In the second portion of our thesis, we have studied the evolution of single particle momentum distribution of the created particles by the spatially homogeneous but time dependent electric field using quantum kinetic approach. It is shown that the distribution is quite sensitive to the temporal profile – to the extent that the two closely resembling temporal envelopes namely, Gaussian and Sauter with the same pulse parameters give rise to significantly different momentum spectrum of pairs at all the temporal stages of evolution. The temporal stages are classified, for convenience, into two distinct regions – transient and asymptotic regions. It is found that the transient region for the Gaussian pulse has larger temporal extent. In the transient region, the spectrum is smooth with a single peak for both the pulses. However the location of peak, the peak height and the width are different for any instant of time and they evolve differently with time. However the peak height for the Gaussian pulse is consistently higher than that for the Sauter pulse. In the other regime, where the spectrum does not change with time, the peak position of the spectrum nearly coincides in both the cases. However, in the asymptotic region, just contrary to the trend in the transient region, the peak height of the spectrum for the Gaussian pulse is lower than that for the Sauter pulse as long as the number of subcycle oscillations, $\omega\tau < 5$. As reported in Ref. [20], the momentum spectrum for the multisheeted Gaussian shows oscillations over the smooth profile due to the quantum mechanical interference of the reflected quasi particle waves from bumpy time-dependent potential. These oscillation are suppressed in the case of Sauter pulse. The onset of oscillation takes place at $\omega\tau = 6$ for the Sauter pulse compared to $\omega\tau = 4$ for the Gaussian pulse. Furthermore, for the same value of $\omega\tau$ the amplitude of oscillation is smaller for the Sauter pulse. In fact, it is due to this interference effect that the peak height of the momentum spectrum for the Gaussian pulse takes over that for the Sauter pulse for $\omega\tau \geq 5$. The sensitivity of the momentum spectrum to the temporal pulse forms is explained by analyzing the shape of potential causing over barrier reflections and also the turning point structure in complex time plane for the two pulse forms.

The differences in the asymptotic time spectrum of the two pulses get much more prominent on increasing the linear frequency chirp in these pulses and also on varying the CEP. Furthermore, the profile and the location of the spectrum is vastly different for the two pulses. Although it may appear somewhat far fetched, measuring momentum spectrum of the pairs may provide a possible method for the determination of the temporal profile for ultrashort pulses.

We have also studied the evolution of the modulus and the phase of the complex order parameter associated with the field induced phase transition of the vacuum state interacting with the time dependent multi-sheeted Sauter pulse with frequency chirping up to the quadratic order. We analyse the different evolution stages of the order parameter e.g., quasi electron positron plasma stage, transient stage, and residual electron-positron plasma stage in the presence of the frequency chirping. We have shown that the onset of the transient stage in the evolution of the modulus of order parameter is governed by the abrupt and large change in the value of phase of the order parameter. We have used our understanding of the evolution of the complex order parameter to the issue of irreversibility and the non monotonic growth of entropy in the context of pair production.

Outlook and future perspective

The main future outlook of the present study can be drawn in the field of ultrafast and ultrashort laser pulse near Schwinger field limit where nonlinear effects are self-sustained. The generation of ultrashort particle bunches with submicron spatial extension may be the next generation particle beams. On the other hand the momentum spectrum of the created pairs not only enable to get full particle dynamics after the production but also help to measure the ultrashort laser pulses in atto-second regimes.

The counter propagating configurations studied in this thesis show the existence of spiky spatiotemporal structure of invariant field. One can envisage a situation where the pairs created in one of the "spikes" interact with the other spikes of the field and there may be possibility of a QED cascade [84] in the presence of structured field patterns".

For the counter propagating configurations we have used the N-F model which is valid in the weak focussing limit. Extending some of these studies to other field models, such as tightly focussed model [11] and optimum e-dipole model would be quite interesting [17]. Furthermore, we have taken the spatio temporal pulse profile to be Gaussian. Some interesting profiles, e,g. the Bessel or higher order Gaussian should also be used in the similar studies.

The effect of back reaction force on the external electric field by the induced electric field generated in pair production process has not been considered in our studies of momentum distribution. Inclusion of collisional effects can also affect the features of field induced phase transition and the entropy production. We wish to take up some of these outstanding problems in future.

Appendix A

Fields of circularly polarized counterpropagating laser beams with parameter of asymmetry μ

A.1 Fields of circularly polarized counterpropagating laser beams with parameter of asymmetry $\mu = \mp 1$

In this Appendix A.1, we present a detailed calculation for the electric and magnetic fields for the right circularly polarized counterpropagating laser pulses made up of purely e-waves which are propagating in $+z$ (forward) and $-z$ (backward) directions as mentioned in **Chapter** 2. Following [10], we begin with the expressions for the complex e-wave electric and the magnetic fields of the focussed laser beams propagating in the forward and backward directions and having their focal region at $z = 0$. In the end we take real parts of the fields and these are used to calculate the invariants given in **Chapter** 2. Fields for the forward pulse are:

$$\mathbf{E}_f^e = iE_0 e^{-i\omega(t-z/c)} g \Big\{ F_1(\hat{\mathbf{e}}_x + i\hat{\mathbf{e}}_y) - F_2 e^{2i\phi}(\hat{\mathbf{e}}_x - i\hat{\mathbf{e}}_y) \Big\}, \tag{A.1}$$

and

$$\mathbf{H}_f^e = E_0 e^{-i\omega(t-z/c)} g \Big\{ (1 - i\Delta^2 \frac{\partial}{\partial \chi}) \Big[F_1(\hat{\mathbf{e}}_x + i\hat{\mathbf{e}}_y) + F_2 e^{2i\phi}(\hat{\mathbf{e}}_x - i\hat{\mathbf{e}}_y) \Big] + 2i\Delta e^{i\phi} \frac{\partial F_1}{\partial \xi} \hat{\mathbf{e}}_z \Big\}. \tag{A.2}$$

Fields for the backward pulse are:

$$\mathbf{E}_b^e = iE_0 e^{-i\omega(t+z/c)} g\Big\{F_1^*(\hat{\mathbf{e}}_x + i\hat{\mathbf{e}}_y) - F_2^* e^{-2i\phi}(\hat{\mathbf{e}}_x - i\hat{\mathbf{e}}_y)\Big\}, \tag{A.3}$$

and

$$\mathbf{H}_b^e = -E_0 e^{-i\omega(t+z/c)} g\Big\{(1 + i\Delta^2 \frac{\partial}{\partial \chi})\Big[F_1^*(\hat{\mathbf{e}}_x + i\hat{\mathbf{e}}_y) + F_2^* e^{-2i\phi}(\hat{\mathbf{e}}_x - i\hat{\mathbf{e}}_y)\Big] + 2i\Delta e^{-i\phi}\frac{\partial F_1^*}{\partial \xi}\hat{\mathbf{e}}_z\Big\}. \tag{A.4}$$

Here F_1, F_2 are the Gaussian form functions for the focused laser beam [10] given as $F_1 = (1 + 2i\chi)^{-2}(1 - \xi^2/(1 + 2i\chi))\exp(-\xi^2/(1 + 2i\chi))$ and $F_2 = -\xi^2(1 + 2i\chi)^{-3}\exp(-\xi^2((1 + 2i\chi))$. $F_1^*$and, F_2^* are complex conjugates of the respective form functions. The other parameters are already defined in **Chapter** 2. The resultant electric and magnetic fields due to the superposition of forward and backward pulses are given by:

$$\mathbf{E}^e = \mathbf{E}_f^e + \mathbf{E}_b^e = 2iE_0 e^{-i\omega t} g\Big\{(\hat{\mathbf{e}}_x + i\hat{\mathbf{e}}_y)Re\Big[F_1 e^{i\omega z/c}\Big] - (\hat{\mathbf{e}}_x - i\hat{\mathbf{e}}_y)Re\Big[F_2 e^{2i\phi} e^{i\omega z/c}\Big]\Big\}. \tag{A.5}$$

$$\begin{aligned}\mathbf{H}^e = \mathbf{H}_f^e + \mathbf{H}_b^e = 2iE_0 e^{-i\omega t} g\Big\{&(\hat{\mathbf{e}}_x + i\hat{\mathbf{e}}_y)Im\Big[F_1 e^{i\omega z/c}\Big] + (\hat{\mathbf{e}}_x - i\hat{\mathbf{e}}_y)Im\Big[F_2 e^{2i\phi} e^{i\omega z/c}\Big] \\ &+2i\Delta Im\Big[e^{i\phi} e^{i\omega z/c}\frac{\partial F_1}{\partial \xi}\Big]\hat{\mathbf{e}}_z\Big\}.\end{aligned} \tag{A.6}$$

In Eq. A.6 we have neglected the term having Δ^2 as $\Delta << 1$ in the weak focusing limit. Using the expressions of F_1 and F_2 the complex electric and magnetic fields can be written as:

$$\begin{aligned}\mathbf{E}^e = 2iE_0 g e^{-i\omega t}\frac{e^{-\xi^2/1+4\chi^2}}{(1+4\chi^2)}\Big[&\Big\{\cos(\omega z/c - 2\psi + \frac{2\chi\xi^2}{1+4\chi^2}) - \frac{2\xi^2\sin\phi}{(1+4\chi^2)^{1/2}} \\ &\sin(\phi + \omega z/c - 3\psi + \frac{2\chi\xi^2}{1+4\chi^2})\Big\}\mathbf{e}_x + i\Big\{\cos(\omega z/c - 2\psi + \frac{2\chi\xi^2}{1+4\chi^2}) \\ &-\frac{2\xi^2\cos\phi}{(1+4\chi^2)^{1/2}}\cos(\phi + \omega z/c - 3\psi + \frac{2\chi\xi^2}{1+4\chi^2})\Big\}\mathbf{e}_y\Big],\end{aligned} \tag{A.7}$$

$$\begin{aligned}\mathbf{H}^e = 2iE_0 g e^{-i\omega t}\frac{e^{-\frac{\xi^2}{1+4\chi^2}}}{(1+4\chi^2)}\Big[&\Big\{\sin(\omega z/c - 2\psi) - \frac{2\xi^2\cos\phi}{(1+4\chi^2)^{1/2}}\sin(\phi + \omega z/c - 3\psi)\Big\}\mathbf{e}_x \\ &+i\Big\{\sin(\omega z/c - 2\psi) - \frac{2\xi^2\sin\phi}{(1+4\chi^2)^{1/2}}\cos(\phi + \omega z/c - 3\psi)\Big\}\mathbf{e}_y \\ &-\frac{8\Delta\xi}{(1+4\chi^2)^{1/2}}(1 - \frac{\xi^2}{2(1+4\chi^2)^{1/2}})\cos(\phi + \omega z/c)\mathbf{e}_z\Big].\end{aligned} \tag{A.8}$$

The above equations can be further simplified by neglecting the terms $2\chi\xi^2/(1 + 4\chi^2)$ and $\psi(= \arctan 2\chi)$ in comparison to the spatial frequency wz/c from the phase terms describing oscillations of the EM field along the propagation (z) direction. This approximation will be used henceforth. Finally, we have the expressions of the real electric and magnetic fields in explicit form as:

$$\begin{aligned}\mathbf{E}^e = 2E_0 g \frac{e^{-\frac{\xi^2}{1+4\chi^2}}}{(1+4\chi^2)}\Big[& \sin\omega t\Big\{\cos\omega z/c - \frac{2\xi^2\sin\phi}{(1+4\chi^2)^{1/2}}\sin(\phi+\omega z/c)\Big\}\hat{\mathbf{e}}_x \\ & - \cos\omega t\Big\{\cos\omega z/c - \frac{2\xi^2\cos\phi}{(1+4\chi^2)^{1/2}}\cos(\phi+\omega z/c)\Big\}\hat{\mathbf{e}}_y\Big],\end{aligned} \tag{A.9}$$

and

$$\begin{aligned}\mathbf{H}^e \approx 2E_0 g \frac{e^{-\frac{\xi^2}{1+4\chi^2}}}{(1+4\chi^2)}\Big[& \sin\omega t\Big\{\sin\omega z/c - \frac{2\xi^2\cos\phi}{(1+4\chi^2)^{1/2}}\sin(\phi+\omega z/c)\Big\}\hat{\mathbf{e}}_x \\ & - \cos\omega t\Big\{\sin\omega z/c - \frac{2\xi^2\sin\phi}{(1+4\chi^2)^{1/2}}\cos(\phi+\omega z/c)\Big\}\hat{\mathbf{e}}_y \\ & - \frac{8\Delta\xi}{(1+4\chi^2)^{1/2}}(1-\frac{\xi^2}{2(1+4\chi^2)^{1/2}})\cos(\phi+\omega z/c)\cos\omega t\hat{\mathbf{e}}_z\Big].\end{aligned} \tag{A.10}$$

Using Eqs. (A.9 - A.10) the magnitude of the fields in the focal region can be written as:

$$\begin{aligned}|\mathbf{E}^e| \approx \frac{2E_0 g e^{-\frac{\xi^2}{1+4\chi^2}}}{(1+4\chi^2)}|\cos\omega z/c|\Big[& 1 - \frac{\xi^2}{\cos\omega z/c(1+4\chi^2)^{1/2}}\Big\{\cos\omega z/c \\ & + \cos 2\omega t\cos(\omega z/c + 2\phi)\Big\} + O(\xi^4)\Big],\end{aligned} \tag{A.11}$$

and

$$\begin{aligned}|\mathbf{H}^e| \approx \frac{2E_0 g e^{-\frac{\xi^2}{1+4\chi^2}}}{(1+4\chi^2)}|\sin\omega z/c|\Big[& 1 - \frac{\xi^2}{\sin\omega z/c(1+4\chi^2)^{1/2}}\Big\{\sin\omega z/c \\ & - \cos 2\omega t\sin(\omega z/c + 2\phi)\Big\} + O(\xi^4)\Big].\end{aligned} \tag{A.12}$$

Eqs. (A.11 - A.12) are used to get the expression for $\mathcal{F}^e$ while Eqs. (A.9 - A.10) are used to get the expression for $\mathcal{G}^e$ and hence the expressions of ϵ^e and η^e given in **Chapter** 2. The expressions of the EM fields, invariants, and invariant EM fields for $\mu = 1$ can be written as the dual transform of those for the $\mu = -1$ case. For the complex EM fields $\mathbf{E}^h = i\mathbf{H}^e$, and $\mathbf{H}^h = -i\mathbf{E}^e$ [10] which implies $\mathcal{F}^h = -\mathcal{F}^e$, $\mathcal{G}^h = \mathcal{G}^e$., $\epsilon^h = \eta^e$ and $\eta^h = \epsilon^e$.

A.2 Fields for circularly polarized counterpropagating laser pulses with $\mu = 0$

As done in Appendix A.1 we begin with the complex fields which allow us to write the electric and the magnetic fields for the counterpropagating laser pulses made up of equal mixture of e- and h- waves ($\mu = 0$) as $\mathbf{E}^{e+h} = (\mathbf{E}^e + \mathbf{E}^h)/2 = (\mathbf{E}^e + i\mathbf{H}^e)/2$, and $\mathbf{H}^{e+h} = (\mathbf{H}^e + \mathbf{H}^h)/2 = (\mathbf{H}^e - i\mathbf{E}^e)/2$. Using the expressions of $\mathbf{E}^e$ and $\mathbf{H}^e$ from Eqs. (A.7,A.8) we have the explicit expression of $\mathbf{E}^{e+h}$ as:

$$\begin{aligned}\mathbf{E}^{e+h} = iE_0 e^{-i\omega t} g \frac{e^{-\frac{\xi^2}{1+4\chi^2}}}{1+4\chi^2}\Big\{\Big[\exp(i(\omega z/c - 2\psi)) - \frac{2i\xi^2}{(1+4\chi^2)^{1/2}} e^{-i\phi}\sin(\omega z/c + \phi - 2\psi)\Big]\hat{\mathbf{e}}_x \\ + i\Big[\exp(i(\omega z/c - 2\psi)) - \frac{2i\xi^2}{(1+4\chi^2)^{1/2}} e^{-i\phi}\cos(\omega z/c + \phi - 2\psi)\Big]\hat{\mathbf{e}}_y - \frac{8\Delta\xi}{(1+4\chi^2)^{1/2}}(1- \\ \frac{\xi^2}{2(1+4\chi^2)1/2})\cos(\phi + \omega z/c)\hat{\mathbf{e}}_z\Big\},\end{aligned} \tag{A.13}$$

and $\mathbf{H}^{e+h} = -i\mathbf{E}^{e+h}$. The physical fields are given by taking the real parts of the above equations:

$$\begin{aligned}\mathbf{E}^{e+h} \approx E_0 g \frac{e^{-\frac{\xi^2}{1+4\chi^2}}}{(1+4\chi^2)}\Big[\hat{\mathbf{e}}_x\Big\{\sin(\omega t - \omega z/c + 2\psi) + \frac{2\xi^2\cos(\omega t + \phi)}{(1+4\chi^2)^{1/2}}\sin(\omega z/c + \phi - 3\psi)\Big\} \\ -\hat{\mathbf{e}}_y\Big\{\cos(\omega t - \omega z/c + 2\psi) - \frac{2\xi^2\cos(\omega t + \phi)}{(1+4\chi^2)^{1/2}}\cos(\omega z/c + \phi - 3\psi)\Big\} + \frac{8\Delta\xi}{(1+4\chi^2)^{1/2}} \\ \times\cos\omega t\cos(\phi + \omega z/c)\hat{\mathbf{e}}_z\Big],\end{aligned} \tag{A.14}$$

and

$$\begin{aligned}\mathbf{H}^{e+h} \approx E_0 g \frac{e^{-\frac{\xi^2}{1+4\chi^2}}}{(1+4\chi^2)}\Big[\hat{\mathbf{e}}_x\Big\{\cos(\omega t - \omega z/c + 2\psi) - \frac{2\xi^2\sin(\omega t + \phi)}{(1+4\chi^2)^{1/2}}\sin(\omega z/c + \phi - 3\psi)\Big\} \\ +\hat{\mathbf{e}}_y\Big\{\sin(\omega t - \omega z/c + 2\psi) - \frac{2\xi^2\sin(\omega t + \phi)}{(1+4\chi^2)^{1/2}}\cos(\omega z/c + \phi - 3\psi)\Big\} - \frac{8\Delta\xi}{(1+4\chi^2)^{1/2}} \\ \times\sin\omega t\cos(\phi + \omega z/c)\hat{\mathbf{e}}_z\Big].\end{aligned} \tag{A.15}$$

We calculate the magnitude of the real part of the electric and magnetic fields:

$$|\mathbf{E}^{e+h}| \approx E_0 g \frac{e^{-\frac{\xi^2}{1+4\chi^2}}}{1+4\chi^2}\Big[1 - \frac{2\xi^2}{(1+4\chi^2)^{1/2}}\cos(\omega t+\phi)\cos(\omega t+\phi-\psi) + \frac{2\xi^4}{(1+4\chi^2)}\cos^2(\omega t+\phi) + \frac{32\Delta^2\xi^2}{(1+4\chi^2)^3}\cos\omega t\cos^2(\phi+\omega z/c)\Big]. \tag{A.16}$$

$$|\mathbf{H}^{e+h}| \approx E_0 g \frac{e^{-\frac{\xi^2}{1+4\chi^2}}}{1+4\chi^2}\Big[1 - \frac{2\xi^2}{(1+4\chi^2)^{1/2}}\sin(\omega t+\phi)\sin(\omega t+\phi-\psi) + \frac{2\xi^4}{(1+4\chi^2)}\sin^2(\omega t+\phi) + \frac{32\Delta^2\xi^2}{(1+4\chi^2)^3}\sin\omega t\cos^2(\phi+\omega z/c)\Big]. \tag{A.17}$$

Eqs. (A.16 - A.17) are used to get the expression for $\mathcal{F}^{e+h}$ while Eqs. (A.14 - A.15) are used to get the expression for $\mathcal{G}^{e+h}$ and hence the expressions of ϵ^{e+h} and η^{e+h} given in **Chapter** 2.

Appendix B

Electromagnetic fields with CEP dependence for linear and circular polarizations

B.1 Linear polarization counterpropagating laser pulses and the CEP dependence

For the linearly e-polarized focused EM fields, the expressions of the electric field in both forward (in z direction) and backward (in $-z$ direction) propagations can be written as [15]

$$\mathbf{E}_f^e = iE_0 e^{-i\omega(t-z/c)-i\tilde{\varphi}} g\Big[\hat{\mathbf{e}}_x(F_1 - F_2\cos 2\phi) - \hat{\mathbf{e}}_y F_2 \sin 2\phi\Big], \tag{B.1}$$

and

$$\mathbf{E}_b^e = iE_0 e^{-i\omega(t+z/c)-i\tilde{\varphi}} g\Big[\hat{\mathbf{e}}_x(F_1^* - F_2^*\cos 2\phi) - \hat{\mathbf{e}}_y F_2^* \sin 2\phi\Big]. \tag{B.2}$$

Here $F_1,\ F_2$ are the complex Gaussian form functions for the focused laser beam [10] given as

$$F_1 = (1+2i\chi)^{-2}(1-\frac{\xi^2}{1+2i\chi})\exp(-\frac{\xi^2}{1+2i\chi}), \text{ and } F_2 = -\xi^2(1+2i\chi)^{-3}\exp(-\frac{\xi^2}{1+2i\chi}). \tag{B.3}$$

$F_1^*,\ \ F_2^*$ are the complex conjugate of them. All the symbols have already been defined in Sec. 3.1.1. Similarly one can have the expressions magnetic field in forward and backward directions as [15]

$$\mathbf{H}_f^e = iE_0 e^{-i\omega(t-z/c)-i\tilde{\varphi}} g\Big[(1 - i\Delta^2 \frac{\partial}{\partial \chi})\Big\{\hat{\mathbf{e}}_x F_2 \sin 2\phi - \hat{\mathbf{e}}_y (F_1 - F_2 \cos 2\phi)\Big\} + 2i\Delta \sin\phi \frac{\partial F_1}{\partial \xi}\Big], \quad \text{(B.4)}$$

and

$$\mathbf{H}_b^e = -iE_0 e^{-i\omega(t+z/c)-i\tilde{\varphi}} g\Big[(1 + i\Delta^2 \frac{\partial}{\partial \chi})\Big\{\hat{\mathbf{e}}_x F_2^* \sin 2\phi - \hat{\mathbf{e}}_y (F_1^* - F_2^* \cos 2\phi)\Big\} + 2i\Delta \sin\phi \frac{\partial F_1^*}{\partial \xi}\Big]. \quad \text{(B.5)}$$

Now if we allow them to superimpose in the focal region, the expressions of the electric and magnetic fields are given by

$$\mathbf{E}^e = \mathbf{E}_f^e + \mathbf{E}_b^e = 2iE_0 e^{-i(\omega t+\tilde{\varphi})} g\Big[\hat{\mathbf{e}}_x Re\Big[(F_1 - F_2 \cos 2\phi) e^{i\omega z/c}\Big] - \hat{\mathbf{e}}_y Re\Big[F_2 e^{i\omega z/c} \sin 2\phi\Big]\Big], \quad \text{(B.6)}$$

and

$$\begin{aligned}\mathbf{H}^e = \mathbf{H}_f^e + \mathbf{H}_b^e = -2E_0 e^{-i(\omega t+\tilde{\varphi})} g\Big[&\hat{\mathbf{e}}_x Im\Big[F_2 e^{i\omega z/c} \sin 2\phi\Big] + \hat{\mathbf{e}}_y Im\Big[(F_1 - F_2 \cos 2\phi) e^{i\omega z/c}\Big] \\ &+ 2i\Delta \sin\phi\, Im\Big[e^{i\omega z/c} \frac{\partial F_1}{\partial \xi}\Big]\Big].\end{aligned} \quad \text{(B.7)}$$

But the physical electric and magnetic fields are real part of Eqs. (B.6,B.7) which are given as

$$\begin{aligned}Re\mathbf{E}^e &= 2E_0 \sin(\omega t + \tilde{\varphi}) g\Big[\hat{\mathbf{e}}_x Re\Big[(F_1 - F_2 \cos 2\phi) e^{i\omega z/c}\Big] - \hat{\mathbf{e}}_y Re\Big[F_2 e^{i\omega z/c} \sin 2\phi\Big]\Big] = 2E_0 g \frac{e^{-\xi^2/(1+4\chi^2)}}{1+4\chi^2} \sin(\omega t + \tilde{\varphi}) \\ &\times\Big[\hat{\mathbf{e}}_x \Big\{\cos(\omega z/c - 2\psi) - \frac{2\xi^2}{(1+4\chi^2)^{1/2}} \sin^2\phi \cos(\omega z/c - 3\psi)\Big\} + \hat{\mathbf{e}}_y \frac{\xi^2}{(1+4\chi^2)^{1/2}} \sin 2\phi \cos(\omega z/c - 3\psi)\Big],\end{aligned} \quad \text{(B.8)}$$

and

$$\begin{aligned}Re\mathbf{H}^e &= -2E_0 g\Big[\cos(\omega t + \tilde{\varphi})\Big\{\hat{\mathbf{e}}_x Im\Big[F_2 e^{i\omega z/c} \sin 2\phi\Big] + \hat{\mathbf{e}}_y Im\Big[(F_1 - F_2 \cos 2\phi) e^{i\omega z/c}\Big]\Big\} + 2\Delta \sin\phi \sin(\omega t + \tilde{\varphi}) \\ &\times\Big[e^{i\omega z/c} \frac{\partial F_1}{\partial \xi}\Big]\Big] \approx -2E_0 g \frac{e^{-\xi^2/(1+4\chi^2)}}{1+4\chi^2}\Big[\cos(\omega t + \tilde{\varphi})\Big(\hat{\mathbf{e}}_x \frac{\xi^2}{(1+4\chi^2)^{1/2}} \sin 2\phi \sin(\omega z/c - 3\psi) - \hat{\mathbf{e}}_y \Big\{\sin(\omega z/c - 2\psi) \\ &- \frac{2\xi^2}{(1+4\chi^2)^{1/2}} \sin^2\phi \sin(\omega z/c - 3\psi)\Big\}\Big) + 4\xi\Delta \frac{\sin(\omega t + \tilde{\varphi})}{(1+4\chi^2)^{1/2}} \sin\phi \sin(\omega z/c - 3\psi) \hat{\mathbf{e}}_z\Big].\end{aligned} \quad \text{(B.9)}$$

To derive the approximate Eqs. (B.8,B.9) we have used the expressions of F_1, F_2 from the Eq. 4.5 in the small χ, ξ limit. It shows that resultant fields are oscillating in longitudinal coordinate and time also. It also shows the CEP dependence in the leading order term.

B.2 Circular polarization counterpropagating laser pulses and the CEP dependence

Here we discuss the CEP dependence on the structure of the EM fields due to the superposition of two counterpropagating laser pulses made up of circularly e-polarized focused Gaussian pulses propagating in $+z$ and $-z$ direction. To start with, the expression of the electric and magnetic fields for the forward propagating circularly e-polarized focused Gaussian laser pulse are given as

$$\mathbf{E}^e_f = iE_0 e^{-i\omega(t-z/c)-i\tilde{\varphi}} g\Big\{F_1(\hat{\mathbf{e}}_x \pm i\hat{\mathbf{e}}_y) - F_2 e^{\pm 2i\phi}(\hat{\mathbf{e}}_x \mp i\hat{\mathbf{e}}_y)\Big\}, \tag{B.10}$$

and

$$\mathbf{H}^e_f = \pm E_0 e^{-i\omega(t-z/c)-i\tilde{\varphi}} g\Big\{(1 - i\Delta^2\frac{\partial}{\partial\chi})\Big[F_1(\hat{\mathbf{e}}_x \pm i\hat{\mathbf{e}}_y) + F_2 e^{\pm 2i\phi}(\hat{\mathbf{e}}_x \mp i\hat{\mathbf{e}}_y)\Big] + 2i\Delta e^{\pm i\phi}\frac{\partial F_1}{\partial\xi}\hat{\mathbf{e}}_z\Big\}. \tag{B.11}$$

Here F_1, F_2 are the complex Gaussian beam functions for the focused laser EM field which have already been defined in **Appendix** B.1 and other EM field dependent terms have been defined in Sec. 3.1.1. The $\pm$ signs denote the right and left circularly polarized pulses correspondingly in their polarization vector rotation. Similar expression of the EM field in the backward direction (in $-z$ direction) can be written as

$$\mathbf{E}^e_b = iE_0 e^{-i\omega(t+z/c)-i\tilde{\varphi}} g\Big\{F_1^*(\hat{\mathbf{e}}_x \pm i\hat{\mathbf{e}}_y) - F_2^* e^{\mp 2i\phi}(\hat{\mathbf{e}}_x \mp i\hat{\mathbf{e}}_y)\Big\}, \tag{B.12}$$

and

$$\mathbf{H}^e_b = \mp E_0 e^{-i\omega(t+z/c)-i\tilde{\varphi}} g\Big\{(1 + i\Delta^2\frac{\partial}{\partial\chi})\Big[F_1^*(\hat{\mathbf{e}}_x \pm i\hat{\mathbf{e}}_y) + F_2^* e^{\mp 2i\phi}(\hat{\mathbf{e}}_x \mp i\hat{\mathbf{e}}_y)\Big] + 2i\Delta e^{\mp i\phi}\frac{\partial F_1^*}{\partial\xi}\hat{\mathbf{e}}_z\Big\}. \tag{B.13}$$

Due to the superposition of forward and backward propagating laser EM fields, we have the resultant electric and magnetic fields as

$$\begin{aligned}\mathbf{E}^e = \mathbf{E}^e_f + \mathbf{E}^e_b = iE_0 e^{-i\omega t - i\tilde{\varphi}} g\Big\{ & e^{i\omega z/c}\Big[F_1(\hat{\mathbf{e}}_x \pm i\hat{\mathbf{e}}_y) - F_2 e^{\pm 2i\phi}(\hat{\mathbf{e}}_x \mp i\hat{\mathbf{e}}_y)\Big] \\ & + e^{-i\omega z/c}\Big[F_1^*(\hat{\mathbf{e}}_x \pm i\hat{\mathbf{e}}_y) - F_2^* e^{\mp 2i\phi}(\hat{\mathbf{e}}_x \mp i\hat{\mathbf{e}}_y)\Big]\Big\},\end{aligned} \tag{B.14}$$

and

$$\mathbf{H}^e = \mathbf{H}^e_f + \mathbf{H}^e_b = \pm E_0 e^{-i\omega t - i\tilde{\varphi}} g \Big\{ e^{i\omega z/c}\Big((1 - i\Delta^2 \frac{\partial}{\partial \chi})\Big[F_1(\hat{\mathbf{e}}_x \pm i\hat{\mathbf{e}}_y) + F_2 e^{\pm 2i\phi}(\hat{\mathbf{e}}_x \mp i\hat{\mathbf{e}}_y)\Big]$$
$$+2i\Delta e^{\pm i\phi}\frac{\partial F_1}{\partial \xi}\hat{\mathbf{e}}_z\Big) \mp e^{-i\omega z/c}\Big((1 + i\Delta^2 \frac{\partial}{\partial \chi})\Big[F_1^*(\hat{\mathbf{e}}_x \pm i\hat{\mathbf{e}}_y) + F_2^* e^{\mp 2i\phi}(\hat{\mathbf{e}}_x \mp i\hat{\mathbf{e}}_y)\Big] + 2i\Delta e^{\mp i\phi}\frac{\partial F_1^*}{\partial \xi}\hat{\mathbf{e}}_z\Big)\Big\}. \tag{B.15}$$

Eqs. (B.14,B.15) give the expression of the electric and magnetic fields due the superposition of two counterpropagating circularly polarized laser pulses for both right and left circularly polarized pulses. Here we explicitly derive the expressions of the electric and magnetic fields for the combinations of right-right and right-left for the forward and backward propagating laser pulses.

B.2.1 Circularly polarized beams are right -right combinations in their polarization vectors rotation

When both the pulses are right circularly polarized the expression for electric and magnetic fields from the Eqs. (B.14,B.15) is given as

$$\mathbf{E}^e = \mathbf{E}^e_f + \mathbf{E}^e_b = 2iE_0 e^{-i(\omega t + \tilde{\varphi})} g \Big\{ (\hat{\mathbf{e}}_x + i\hat{\mathbf{e}}_y) Re\Big[F_1 e^{i\omega z/c}\Big] - (\hat{\mathbf{e}}_x - i\hat{\mathbf{e}}_y) Re\Big[F_2 e^{2i\phi} e^{i\omega z/c}\Big]\Big\}, \tag{B.16}$$

and

$$\mathbf{H}^e = \mathbf{H}^e_f + \mathbf{H}^e_b = 2iE_0 e^{-i(\omega t + \tilde{\varphi})} g \Big\{ (\hat{\mathbf{e}}_x + i\hat{\mathbf{e}}_y) Im\Big[F_1 e^{i\omega z/c}\Big] + (\hat{\mathbf{e}}_x - i\hat{\mathbf{e}}_y) Im\Big[F_2 e^{2i\phi} e^{i\omega z/c}\Big]$$
$$+2i\Delta Im\Big[e^{i\phi} e^{i\omega z/c}\frac{\partial F_1}{\partial \xi}\Big]\hat{\mathbf{e}}_z\Big\}. \tag{B.17}$$

The physical electric and magnetic fields are real part of the Eqs. (B.16,B.17) which are given as

$$Re\mathbf{E}^e = 2E_0 g\Big[\sin(\omega t + \tilde{\varphi}) Re\Big[(F_1 - F_2 e^{2i\phi}) e^{i\omega z/c}\Big]\hat{\mathbf{e}}_x - \cos(\omega t + \tilde{\varphi}) Re\Big[(F_1 + F_2 e^{2i\phi}) e^{i\omega z/c}\Big]\hat{\mathbf{e}}_y\Big], \tag{B.18}$$

and

$$ReH^e = 2E_0g\Big[\sin(\omega t+\tilde{\varphi})Im\Big[(F_1+F_2e^{2i\phi})e^{i\omega z/c}\Big]\hat{\mathbf{e}}_x - \cos(\omega t+\tilde{\varphi})Im\Big[(F_1-F_2e^{2i\phi})e^{i\omega z/c}\Big]\hat{\mathbf{e}}_y \\ -2\Delta\cos(\omega t+\tilde{\varphi})Im\Big[e^{i\phi}e^{i\omega z/c}\frac{\partial F_1}{\partial\xi}\Big]\hat{\mathbf{e}}_z\Big]. \tag{B.19}$$

Now using the expressions of F_1 and F_2 from Eq. 4.5, we have the expression of the electric and magnetic fields as

$$ReE^e = 2E_0g\frac{e^{-\xi^2/1+4\chi^2}}{(1+4\chi^2)}\Big[\sin(\omega t+\tilde{\varphi})\Big\{\cos(\omega z/c-2\psi)-\frac{2\xi^2\sin\phi}{(1+4\chi^2)^{1/2}}\sin(\phi+\omega z/c-3\psi)\Big\}\hat{\mathbf{e}}_x \\ -\cos(\omega t+\tilde{\varphi})\Big\{\cos(\omega z/c-2\psi)-\frac{2\xi^2\cos\phi}{(1+4\chi^2)^{1/2}}\cos(\phi+\omega z/c-3\psi)\Big\}\hat{\mathbf{e}}_y\Big], \tag{B.20}$$

and

$$ReH^e = 2E_0g\frac{e^{-\xi^2/1+4\chi^2}}{(1+4\chi^2)}\Big[\sin(\omega t+\tilde{\varphi})\Big\{\sin(\omega z/c-2\psi)-\frac{2\xi^2\cos\phi}{(1+4\chi^2)^{1/2}}\sin(\phi+\omega z/c-3\psi)\Big\}\hat{\mathbf{e}}_x \\ -\cos(\omega t+\tilde{\varphi})\Big\{\sin(\omega z/c-2\psi)-\frac{2\xi^2\sin\phi}{(1+4\chi^2)^{1/2}}\cos(\phi+\omega z/c-3\psi)\Big\}\hat{\mathbf{e}}_y \\ -\frac{8\Delta\xi}{(1+4\chi^2)^{1/2}}(1-\frac{\xi^2}{2(1+4\chi^2)^{1/2}})\cos(\phi+\omega z/c)\cos(\omega t+\tilde{\varphi})\hat{\mathbf{e}}_z\Big]. \tag{B.21}$$

The corresponding magnitude of the electric and magnetic fields is given by

$$|ReE^e| \approx \frac{2E_0ge^{-\xi^2/1+4\chi^2}}{(1+4\chi^2)}|\cos(\omega z/c-2\psi)|\Big[1-\frac{\xi^2}{\cos(\omega z/c-2\psi)(1+4\chi^2)^{1/2}}\Big\{\cos(\omega z/c-3\psi) \\ +\cos 2(\omega t+\tilde{\varphi})\cos(3\psi-\omega z/c-2\phi)\Big\}+O(\xi^4)\Big], \tag{B.22}$$

and

$$|ReH^e| \approx \frac{2E_0ge^{-\xi^2/1+4\chi^2}}{(1+4\chi^2)}|\sin(\omega z/c-2\psi)|\Big[1-\frac{\xi^2}{\sin(\omega z/c-2\psi)(1+4\chi^2)^{1/2}}\Big\{\sin(\omega z/c-3\psi) \\ +\cos 2(\omega t+\tilde{\varphi})\sin(3\psi-\omega z/c-2\phi)\Big\}+O(\xi^4)\Big]. \tag{B.23}$$

B.2.2 Circularly polarized beams are right-left combinations in their polarization vectors rotation

Here we derive the expression of the electric and magnetic fields due to the superposition of right circularly forward propagating pulse with the left circularly backward propagating pulse. Form the Eqs. (B.14,B.15) the expression of the real part of the electric and magnetic fields can be written as

$$Re\mathbf{E}^e = 2E_0 g\Big\{\Big(\sin(\omega t+\tilde{\varphi})Re[F_1 e^{i\omega z/c}] - \sin(\omega t+\tilde{\varphi}-2\phi)Re[F_2 e^{i\omega z/c}]\Big)\hat{\mathbf{e}}_x - \Big(\sin(\omega t+\tilde{\varphi})Im[F_1 e^{i\omega z/c}] + \sin(\omega t+\tilde{\varphi}-2\phi)Im[F_2 e^{i\omega z/c}]\Big)\hat{\mathbf{e}}_y\Big\} \tag{B.24}$$

and

$$Re\mathbf{H}^e = 2E_0 g\Big\{\Big(\cos(\omega t+\tilde{\varphi})Re[F_1 e^{i\omega z/c}] + \cos(\omega t+\tilde{\varphi}-2\phi)Re[F_2 e^{i\omega z/c}]\Big)\hat{\mathbf{e}}_x - \Big(\cos(\omega t+\tilde{\varphi})Im[F_1 e^{i\omega z/c}] - \cos(\omega t+\tilde{\varphi}-2\phi)Im[F_2 e^{i\omega z/c}]\Big)\hat{\mathbf{e}}_y + 2\Delta\sin(\omega t+\tilde{\varphi}-\phi)Re[e^{i\omega z/c}\frac{\partial F_1}{\partial \xi}]\hat{\mathbf{e}}_z\Big\}. \tag{B.25}$$

Using the explicit expression of F_1 and F_2 from Eq. (B.3) we derive the simplified form of the Eqs. (B.24,B.25) in normalized spatial coordinates as follows:

$$Re\mathbf{E}^e = 2E_0 g\frac{e^{-\xi^2/1+4\chi^2}}{(1+4\chi^2)}\Big[\Big\{\sin(\omega t+\tilde{\varphi})\Big(\cos(\omega z/c-2\psi) - \frac{\xi^2}{(1+4\chi^2)^{1/2}}\cos(\omega z/c-3\psi)\Big) + \sin(\omega t+\tilde{\varphi}-2\phi) \times\frac{\xi^2}{(1+4\chi^2)^{1/2}}\cos(\omega z/c-3\psi)\Big\}\hat{\mathbf{e}}_x - \Big\{\sin(\omega t+\tilde{\varphi})\Big(\sin(\omega z/c-2\psi) - \frac{\xi^2}{(1+4\chi^2)^{1/2}}\sin(\omega z/c-3\psi)\Big) - \sin(\omega t+\tilde{\varphi}-2\phi)\frac{\xi^2}{(1+4\chi^2)^{1/2}}\sin(\omega z/c-3\psi)\Big\}\hat{\mathbf{e}}_y\Big], \tag{B.26}$$

and

$$Re\mathbf{H}^e = 2E_0 g\frac{e^{-\xi^2/1+4\chi^2}}{(1+4\chi^2)}\Bigg[\Big\{\cos(\omega t+\tilde{\varphi})\Big(\cos(\omega z/c-2\psi)-\frac{\xi^2}{(1+4\chi^2)^{1/2}}\cos(\omega z/c-3\psi)\Big)-\cos(\omega t+\tilde{\varphi}-2\phi)$$
$$\times\frac{\xi^2}{(1+4\chi^2)^{1/2}}\cos(\omega z/c-3\psi)\Big\}\hat{\mathbf{e}}_x-\Big\{\cos(\omega t+\tilde{\varphi})\Big(\sin(\omega z/c-2\psi)-\frac{\xi^2}{(1+4\chi^2)^{1/2}}\sin(\omega z/c-3\psi)\Big)$$
$$+\cos(\omega t+\tilde{\varphi}-2\phi)\frac{\xi^2}{(1+4\chi^2)^{1/2}}\sin(\omega z/c-3\psi)\Big\}\hat{\mathbf{e}}_y-\frac{8\Delta\xi}{(1+4\chi^2)^{1/2}}\sin(\omega t+\tilde{\varphi}-\phi)\cos(\omega z/c+3\psi)\hat{\mathbf{e}}_z\Bigg]. \tag{B.27}$$

Therefore the magnitude of the electric and magnetic fields is

$$|Re\mathbf{E}^e| = 2E_0 g\frac{e^{-\xi^2/1+4\chi^2}}{(1+4\chi^2)}\Bigg[\sin^2(\omega t+\tilde{\varphi})\Big(1-\frac{\xi^2}{(1+4\chi^2)^{1/2}}\cos\psi\Big)+\frac{2\xi^2}{(1+4\chi^2)^{1/2}}\sin(\omega t+\tilde{\varphi})$$
$$\times\sin(\omega t+\tilde{\varphi}-2\phi)\cos(2\omega z/c-5\psi)+O(\xi^4)\Bigg]^{1/2}, \tag{B.28}$$

and

$$|Re\mathbf{H}^e| = 2E_0 g\frac{e^{-\xi^2/1+4\chi^2}}{(1+4\chi^2)}\Bigg[\cos^2(\omega t+\tilde{\varphi})-\frac{2\xi^2}{(1+4\chi^2)^{1/2}}\Big\{\cos(\omega t+\tilde{\varphi})\Big(\cos(\omega t+\tilde{\varphi})\cos\psi$$
$$+\cos(\omega t+\tilde{\varphi}-2\phi)\cos(2\omega z/c-5\psi)\Big)-\frac{32\xi^2\Delta^2}{(1+4\chi^2)^{1/2}}\cos^2(\omega z/c+3\psi)\sin^2(\omega t+\tilde{\varphi}-\phi)\Big\}\Bigg]^{1/2}. \tag{B.29}$$

Eqs. (B.28,B.29) show that in the leading order the field strength is oscillating and it contains the CEP dependence.

Appendix C

Temporal envelope function for the counterpropagating beams valid at the focus

As shown in Ref. [10], finite pulse duration can be incorporated into a focused pulse model roughly by introducing an individual envelope factor $g(\varphi)$ for each pulse [such that $g(0) = 1$ and $g(\varphi)$ vanishes for $|\varphi| \gtrsim \omega\tau$, where τ is pulse duration]. Let us show that inside a focal region of counterpropagating pulses one can with high accuracy rather use a single common envelope instead. Consider their total (for definiteness, electric) field

$$\mathbf{E}_{tot} = g_1\mathbf{E}_f + g_2\mathbf{E}_b, \tag{C.1}$$

where $\mathbf{E}_{f,b}$ are the fields of forward and backward propagating pulses [see Eqs. (4.3), (4.4)], $g_1 = g_1(\varphi/\omega\tau) = g_1((t - z/c)/\tau)$ and $g_2 = g_2(\varphi'/\omega\tau) = g_2((t + z/c)/\tau)$ – their individual envelopes. For the sake of simplicity, we assume $g_1(\varphi) = g_2(\varphi) = \exp(-4\varphi^2/\tau^2)$, as used throughout the paper. By rewriting

$$\mathbf{E}_{tot} = \sqrt{g_1 g_2}\Big(\sqrt{g_1/g_2}\mathbf{E}_f + \sqrt{g_2/g_1}\mathbf{E}_b\Big), \tag{C.2}$$

we define $g = \sqrt{g_1 g_2} = \exp(-4t^2/\tau^2 - 4z^2/c^2\tau^2)$, then the weight factors $g_f = \sqrt{g_1/g_2}$ and $g_b = \sqrt{g_2/g_1}$ read $g_{f,b} = \exp(\pm 8zt/c\tau^2) = \exp(\pm 8\chi t' L/c\tau)$, where $\chi = z/L$ and $t' = t/\tau$ are the dimensionless longitudinal coordinate and time normalized by laser duration. Even though for the parameters used here ($\tau = 10fs, \lambda = 1\mu m, \Delta = 0.1$) we have $L/c\tau = 5.3$, pair creation is localized in a tiny region $|\chi| \lesssim 0.02$ and $|t'| \lesssim 0.15$ (see Figs. 4.4-4.7), where both weight factors $g_{f,b}$ are close to unity. Hence one can optionally use for the total field a modified common envelope function $g = \sqrt{g_1 g_2}$, which is extremely useful to explain the results in a qualitative way. The numerical results are in good agreement in both cases of using either g_1 and g_2 or the approximate common envelope g.

Appendix D

Derivation of quantum kinetic equation in mean field approximation

In this Appendix we present the technical details of the quantum kinetic equation using quasi-particle representation. We follow the steps in Ref. [32, 63, 78]

D.1 Dynamics of Pair Creation

For the description of electron-positron pair production in an electric field we start from the QED Langrangian density for the fermionic matter field ψ with the gauge field A_μ which is given by.

$$\begin{aligned}\mathcal{L} &= \bar{\psi} i\gamma^\mu(\partial_\mu + ieA_\mu)\psi - m\psi\bar{\psi} - \frac{1}{4}F_{\mu\nu}F^{\mu\nu} \\ &= \bar{\psi} i\gamma^\mu\partial_\mu\psi - e\bar{\psi}\gamma^\mu A_\mu\psi - m\bar{\psi}\psi - \frac{1}{4}F_{\mu\nu}F^{\mu\nu}.\end{aligned} \tag{D.1}$$

From this Lagrangian density, the equation of motion for the Dirac field ψ can be obtained by using the field-theoretic Euler-Lagrange equation

$$\partial_\mu\left(\frac{\partial\mathcal{L}}{\partial(\partial_\mu\bar{\psi})}\right) - \frac{\partial\mathcal{L}}{\partial\bar{\psi}} = 0. \tag{D.2}$$

which gives the Dirac equation for fermionic field ψ

$$(i\gamma^\mu\partial_\mu - e\gamma^\mu A_\mu - m)\psi(x) = 0. \tag{D.3}$$

Here A_μ denotes the vector potential in temporal gauge $A_\mu = (0, 0, 0, A(t))$ and the resulting electric and magnetic fields are $\mathbf{E}(t) = -\dot{\mathbf{A}}(t) = \frac{d\mathbf{A}(t)}{dt}$ and $\mathbf{B} = \nabla \times \mathbf{A}(t) = 0$. We want the solution of the Dirac equation where the eigenstates are of the form

$$\psi^{(\pm)} = [i\gamma^0\partial_0 + \gamma^k p_k - e\gamma^3 A(t) + m]\,\chi^{(\pm)}(\mathbf{r}, t)R_r e^{i\bar{p}.r}. \tag{D.4}$$

The index $k = 1, 2, 3$ and the $(\pm)$ sign in the superscript denotes eigenstates with positive and negative modes which can be realized at $t \to \mp\infty$.

The spinor part is given $R_1 = \begin{pmatrix} 0 \\ 1 \\ 0 \\ -1 \end{pmatrix}$ $R_2 = \begin{pmatrix} 0 \\ 1 \\ 0 \\ -1 \end{pmatrix}$ which are the eigenvectors of the matrix $\gamma^0\gamma^3$ with the orthonormality condition $R_r^\dagger R_s = 2\delta_{rs}$. Therefore we have

$$(i\gamma^\mu\partial_\mu - e\gamma^\mu A_\mu - m)(i\gamma^0\partial_0 + \gamma^k\, p_k - e\gamma^3 A(t) + m)\chi^{\pm}(\, r, t)R_r e^{i\bar{p}.r} = 0. \tag{D.5}$$

By the standard relation of the inner product of 4-vectors we have γ^μ with $\gamma^\mu = \{\gamma^0, \gamma^k\}$
$\partial_\mu = \{\partial_0, -\partial_k\}, \gamma^\mu A_\mu = \gamma^3 A(t)$
$\gamma^\mu\partial_\mu = \gamma^0\partial_0 - \gamma^k\partial_k$
$i\gamma^\mu\partial_\mu = i\gamma^0\partial_0 - i\gamma^k\partial_k = i\gamma^0\partial_0 + \gamma^k p_k$. Therefore we have

$$(-(\gamma^0)^2(\partial_0)^2 - ie\gamma^0\gamma^3\partial_0 A(t) + (\gamma^k)^2(p_k)^2 - ie\gamma^3 A_3\gamma^0\partial_0 + e^2(\gamma^3)^2A^2(t) - m^2)\chi^{(\pm)}(r, t)R_r e^{i\bar{p}.r} = 0 \tag{D.6}$$

$$(-\partial_0^2 - ie\dot{A}(t) - \mathbf{p}_k^2 - m^2 - e^2A^2(t) + 2eA(t)p_3 - m^2)\chi^{(\pm)}(r, t)R_r e^{i\bar{p}.r} = 0 \tag{D.7}$$

$$(-\partial_0^2 - ie\dot{A}(t) - p_k^2 - m^2 - (p_3^2 - 2ep_3A(t) + e^2A^2(t))\chi^{\pm}(r, t)R_r e^{i\bar{p}.r} = 0 \tag{D.8}$$

$$(\partial_0^2 + ie\dot{A}(t)_+\omega^2(\bar{p}, t))\chi^{\pm}(\bar{p}, t) = 0 \tag{D.9}$$

$$\Longrightarrow \ddot{\chi}^{\pm}(\bar{p}, t) = -\Big(\omega^2(\bar{p}, t) + ie\dot{A}(t)\Big)\chi^{\pm}(\bar{p}, t) = 0 \tag{D.10}$$

where $\gamma^k p_k\gamma^3 A(t) = \gamma^k\gamma^3 p_k A(t)$ and $-eA(t)\Big[\gamma^k p_k\gamma^3 + \gamma^3\gamma^k p_k\Big] = -eA(t)\Big[\gamma^k\gamma^3 p_k + \gamma^3\gamma^k p_k\Big]$ $= -eA(t)\Big[\gamma^k\gamma^3 + \gamma^3\gamma^k\Big] = -eA(t)2g_{k3}p_k = 2eA(t)p_3$. Here $\omega(\bar{p}, t) = \sqrt{m^2 + p_\perp^2 + (p_3 - eA(t))^2}$. Now we decompose the quantized matter field with the spinor functions which are complete and orthonormalized. The decomposition of $\Psi(x)$

$$\Psi(x) = \sum_{r,\bar{p}} \Big[\psi^-_{\bar{p},r}(x)b_{\bar{p},r}(t_0) + \psi^+_{\bar{p},r}(x)d^\dagger_{\bar{p},r}\Big] \tag{D.11}$$

where $b_{\bar{p}r}(t_0), b^{\dagger}_{\bar{p}r}(t_0), d_{\bar{p}r}(t_0), d^{\dagger}_{\bar{p}r}(t_0)$ are annihilation and creation operators of electrons and positrons which act on the vacuum in state $|O_{in}\rangle$ at the initial time $t = t_0$ and obey the anti-commutation relations

$$\{b_{\bar{p}r}(t_0), b^{\dagger}_{\bar{p}`r`}(t_0)\} = \{d^{\dagger}_{\bar{p}r}(t_0), d_{\bar{p}'\bar{r}'}(t_0)\} = \delta_{rr'}\delta_{\bar{p}\bar{p}'}. \tag{D.12}$$

For relativistic system, the evolution process mixes the states with negative $\psi^{-}(x)$ and positive $\psi^{+}(x)$ energies. Non-diagonal term appears in the Hamiltonian which is responsible for pair creation. The diagonalization is achieved by a time dependent Bogoliubov transformation from time independent to time dependent basis

$$\begin{aligned} b_{\bar{p},r}(t) &= \alpha_{-\bar{p}}(t)b_{\bar{p}r}(t_0) + \beta_{\bar{p}}(t)d^{\dagger}_{\bar{p}r}(t_0) \\ d_{\bar{p},r}(t) &= \alpha_{-\bar{p}}(t)d_{\bar{p}r}(t_0) + \beta_{-\bar{p}}(t)b^{\dagger}_{-\bar{p}r}(t_0) \end{aligned} \tag{D.13}$$

with the normalization condition $|\alpha_{\bar{p}}(t)|^2 + |\beta_{\bar{p}}(t)|^2 = 1$. The time dependent creation and annihilation operators satisfy the anticommutation relation

$$\{b_{\bar{p}r}(t), b^{\dagger}_{\bar{p}'r'}(t)\} = \{d^{\dagger}_{\bar{p}r}(t), d_{\bar{p}'\bar{r}'}(t)\} = \delta_{rr'}\delta_{\bar{p}\bar{p}'} \tag{D.14}$$

$b_{\bar{p},r}(t)$ and $d_{\bar{p},r}(t)$ describe the quasiparticles at the time t with an instantaneous vacuum $|0_t\rangle$.
$b(t_0),\ b^{\dagger}(t_0):\ d(t_0),\ d^{\dagger}(t_0)$ are the unitary non-equivalent to the system $b(t),\ b^{\dagger}(t):\ d(t),\ d^{\dagger}(t)$
Therefore the Bogoluibov transformation gives the new representation of the field operators

$$\begin{aligned} \psi(x) &= \sum_{r,\bar{p}} \left[\Psi^{-}_{\bar{p},r}(x)b_{\bar{p},r}(t) + \Psi^{+}_{\bar{p},r}(x)d^{\dagger}_{\bar{p},r}(t)\right] \\ &= \sum_{r,\bar{p}} \left[\Psi^{-}_{\bar{p},r}(x)\big(\alpha_{\bar{p}}(t)b_{\bar{p},r}(t) + \beta_{\bar{p}}(t)d^{\dagger}_{-\bar{p}r}(t_0)\big) + \Psi^{+}_{\bar{p},r}(x)\big(\alpha^{*}_{\bar{p}}(t)d^{\dagger}_{\bar{p},r}(t_0) - \beta^{*}_{\bar{p}}(t)b_{-\bar{p}r}(t_0)\big)\right] \\ &= \sum_{r,\bar{p}} \left[b_{\bar{p},r}(t_0)(\Psi^{-}_{\bar{p},r}(x)\alpha_{\bar{p}}(t) - \Psi^{+}_{\bar{p},r}(x)\beta^{*}(t)) + d^{\dagger}_{-\bar{p},r}(t_0)(\Psi^{-}_{\bar{p}r}(x)\beta_{\bar{p}}(t)) + \Psi^{+}_{\bar{p}r}(x)\alpha^{*}_{\bar{p}}(t))\right] \\ &= \sum_{r,\bar{p}} \left[\Psi^{-}_{\bar{p}r}(x)b_{\bar{p}r}(t_0) + \Psi^{+}_{\bar{p},r}(x)d^{\dagger}_{-\bar{p}r}(t_0)\right] \end{aligned} \tag{D.15}$$

where the correspondence are $\psi^{-}_{\bar{p},r}(x) = \Psi^{-}_{\bar{p},r}(x)\alpha_{p}(t) - \Psi^{+}_{\bar{p},r}(x)\beta^{*}_{\bar{p}}(t)$
$\psi^{+}_{\bar{p},r}(x) = \Psi^{-}_{\bar{p},r}(x)\beta_{\bar{p}}(t) + \Psi^{+}_{\bar{p},r}(x)\alpha^{*}_{\bar{p}}(t) = \alpha^{*}(t)\Psi^{+}_{\bar{p},r}(x) + \beta_{\bar{p}}(t)\Psi^{-}(x)$
Therefore it is justified to assume that the function $\Psi^{\pm}_{\bar{p},r}$ have a spin structure similar to that of

$\psi^{\pm}_{\bar{p},r}$,

$$\Psi^{\pm}_{\bar{p},r}(x) = \left[i\gamma^0\partial_0 + \gamma^k\bar{p}_k - e\gamma^3 A(t) + m\right]\phi^{\pm}_{\bar{p}}(x)R_r e^{\pm i\Theta(t)}e^{\bar{p}\bar{x}} \tag{D.16}$$

where the dynamical phase is defined as

$$\Theta(\bar{p},t) = \int_{t_0}^{t} dt'\omega(\bar{p},t') \tag{D.17}$$

and $\phi^{\pm}_{\bar{p}}$ are yet unknown function. Here one can define the adiabatic particle number basis by absorbing the fast oscillating term which is given as

$$B_{\bar{p},r}(t) = b_{\bar{p},r}(t)e^{-i\Theta(\bar{p},t)} \tag{D.18}$$

The Heisenberg equation of motion for the creation and annihilation operators in adiabatic basis is given as

$$\frac{dB_{\bar{p},r}(t)}{dt} = \frac{-e\mathbf{E}(t)\epsilon_{\perp}}{2\omega^2}D^{\dagger}_{-\bar{p},r}(t) + i[H(t), B_{\bar{p},r}(t)], \tag{D.19}$$

and

$$\frac{dD_{\bar{p},r}(t)}{dt} = \frac{-e\mathbf{E}(t)\epsilon_{\perp}}{2\omega^2}B^{\dagger}_{-\bar{p},r}(t) + i[H(t), D_{\bar{p},r}(t)] \tag{D.20}$$

which is a unitary non-equivalence representation of in-vacuum and quasiparticle states. Single particle distribution function or the average occupation number for electron in the quasiparticle representation is given by

$$f_r = \left\langle\, 0_{in}|b^{\dagger}_{\bar{p},r}(t)b_{\bar{p},r}(t)|0_{in}\right\rangle = \left\langle\, 0_{in}|B^{\dagger}_{\bar{p},r}(t)B_{\bar{p},r}(t)|0_{in}\right\rangle, \tag{D.21}$$

and for positrons

$$\bar{f}_r(\bar{p},t) = \left\langle\, 0_{in}|d^{\dagger}_{\bar{p},r}(t)d_{\bar{p},r}(t)|0_{in}\right\rangle = \left\langle\, 0_{in}|D^{\dagger}_{\bar{p},r}(t)D_{\bar{p},r}(t)|0_{in}\right\rangle. \tag{D.22}$$

This will give rise to time dependent averaged particle number $\sum_{r,\bar{p}}\bar{f}_r(\bar{p},t) = \sum_{r,\bar{p}} f_r(\bar{p},t) = N(t)$. Now the evolution equation of the single particle distribution function is given as

$$\frac{df_r}{dt} = \left\langle\, 0_{in}|\frac{dB^{\dagger}_{\bar{p},r}}{dt}(t)B_{\bar{p},r}(t)|0_{in}\right\rangle + \left\langle\, 0_{in}|B^{\dagger}_{\bar{p},r}(t)\frac{dB_{\bar{p},r}(t)}{dt}|0_{in}\right\rangle \tag{D.23}$$

where

$$\frac{dB^{\dagger}_{\bar{p},r}(t)}{dt} = \frac{-e\mathbf{E}(t)\epsilon_{\perp}}{2\omega^2}D_{-\bar{p},r}(t) - i[\hat{H}(t), B_{\bar{p},r}(t)] \tag{D.24}$$

so

$$\begin{aligned}\frac{df_r(\bar{p},t)}{dt} &= \frac{-e\mathbf{E}(t)\epsilon_\perp}{2\omega^2}\Big[\Big\langle 0_{in}|D_{-\bar{p},r}(t)B_{\bar{p},r}(t)|0_{in}\Big\rangle + \Big\langle 0_{in}|B^\dagger_{\bar{p},r}(t)D^\dagger_{-\bar{p},r}(t)|0_{in}\Big\rangle\Big] \\ &= \frac{-e\mathbf{E}(t)\epsilon_\perp}{\omega^2}\mathbf{Re}\Big[\Big\langle 0_{in}|D_{-\bar{p},r}(t)B_{\bar{p},r}(t)|0_{in}\Big\rangle\Big].\end{aligned} \tag{D.25}$$

Here $\Big\langle 0_{in}|D_{-\bar{p},r}(t)B_{\bar{p},r}(t)|0_{in}\Big\rangle = \Phi_r(\bar{p},t)$ the particle antiparticle correlation function. Now the evolution equation for the correlation function is given by

$$\frac{d\Phi_r(\bar{p},t}{dt} = \frac{e\mathbf{E}(t)\epsilon_\perp}{2\omega^2(\bar{p},t)}\Big[2f_r(\bar{p},t)-1\Big] - 2i\omega(\bar{p},t)\Phi_r(\bar{p},t), \tag{D.26}$$

which basically couples the slow and fast varying time scales. Again we integrate Eq. D.26 with time we get

$$\Phi_r(\bar{p},t) = \frac{\epsilon_\perp}{2}\int_{t_0}^{t} dt' \frac{e\mathbf{E}(t')}{\omega^2(\bar{p},t)}\Big[2f_r(\bar{p},t)-1\Big]e^{2i\left[\Theta(\bar{p},t')-\Theta(\bar{p},t)\right]}, \tag{D.27}$$

with the boundary condition $\Phi_r(\bar{p},t)\Big|_{t=t_0}$ vanishes. Therefore the full expansion of $\frac{df_r(\bar{p},t)}{dt}$ is given by

$$\frac{df_r(\bar{p},t)}{dt} = \frac{e\mathbf{E}(t)\epsilon_\perp}{2\omega^2(\bar{p},t)}\int_{t_0}^{t} dt' \frac{e\mathbf{E}(t')}{\omega^2(\bar{p},t}\Big[2f_r(\bar{p},t)-1\Big]\cos\Big(2\Big[\Theta(\bar{p},t)-\Theta(\bar{p},t')\Big]\Big) \tag{D.28}$$

which is required quantum kinetic equation for the single particle distribution function in quasi-particle representation.

D.2 Onset of oscillations in the momentum spectrum of multi sheeted Sauter and Gaussian pulses

Here we use Eq. 5.16 to determine the onset of oscillations for multi sheeted Sauter and Gaussian pulses. We first evaluate the integrals $K^{(p)}_{\mathbf{p}} = \left|\int\limits_{t_p^*}^{t_p} dt\ \omega(\mathbf{p},t)\right|$, $\Theta^{(p,p')}_{\mathbf{p}} = \int\limits_{Re(t_p)}^{Re(t_p')} dt\ \omega(\mathbf{p},t)$ and hence $f_{\mathbf{p}}(\infty)$ for $\omega\tau = 4$ and 6 for both pulses. We take three pairs of turning points (the central one and the adjacent ones on either side of the central pair), t_{p1}, t_{p2}, and t_{p3} and their complex conjugates. So we have from Eq. 5.16 for the three pairs of turning points

$$f_{\mathbf{p}}(\infty) \approx e^{-2K_{\mathbf{p}}^{(p1)}} + e^{-2K_{\mathbf{p}}^{(p2)}} + e^{-2K_{\mathbf{p}}^{(p3)}} - 2\cos\left(2\Theta_{\mathbf{p}}^{(p1,p2)}\right) e^{-K_{\mathbf{p}}^{(p1)}-K_{\mathbf{p}}^{(p2)}} - 2\cos\left(2\Theta_{\mathbf{p}}^{(p2,p3)}\right) e^{-K_{\mathbf{p}}^{(p2)}-K_{\mathbf{p}}^{(p3)}} + 2\cos\left(2\Theta_{\mathbf{p}}^{(p1,p3)}\right) e^{-K_{\mathbf{p}}^{(p1)}-K_{\mathbf{p}}^{(p3)}}, \tag{D.29}$$

where the three pairs of turning points are taken from left to right. In Fig. 5.7 the values of turning points for $\omega\tau = 4$ are $t_{p1} = -83.1 + 13.7068i$, $t_{p2} = 0 + 9.7359i$, $t_{p3} = 83.1 + 13.7068i$ for the Gaussian pulse, whereas for the Sauter pulse the values of turning points are $t_{p1} = -87.056 + 19.5236i$, $t_{p2} = 0 + 9.721i$, $t_{p3} = 87.056 + 19.5236i$. The values of the integrals for the Sauter pulse are $K_{\mathbf{p}}^{(p1)} = \left|\int_{t_{p1}^*}^{t_{p1}} dt\ \omega(\mathbf{p}, t)\right| = 32.3513$, $K_{\mathbf{p}}^{(p2)} = \left|\int_{t_{p2}^*}^{t_{p2}} dt\ \omega(\mathbf{p}, t)\right| = 15.3754$, and $K_{\mathbf{p}}^{(p3)} = \left|\int_{t_{p3}^*}^{t_{p3}} dt\ \omega(\mathbf{p}, t)\right| = 32.3513$. Therefore, in Eq. D.29 the value of the exponentials are $e^{-2K_{\mathbf{p}}^{(p1)}} = 7.9438 \times 10^{-29}$, $e^{-2K_{\mathbf{p}}^{(p2)}} = 4.4165 \times 10^{-14}$, $e^{-2K_{\mathbf{p}}^{(p3)}} = 7.9438 \times 10^{-29}$, $e^{-K_{\mathbf{p}}^{(p1)}-K_{\mathbf{p}}^{(p2)}} = 1.87309 \times 10^{-21}$, $e^{-K_{\mathbf{p}}^{(p2)}-K_{\mathbf{p}}^{(p3)}} = 1.87309 \times 10^{-21}$, and $e^{-K_{\mathbf{p}}^{(p1)}-K_{\mathbf{p}}^{(p3)}} = 7.9438 \times 10^{-29}$. The orders of the exponentials show that the main contribution to $f_{\mathbf{p}}$ comes from only one turning point pair, t_{p2} and its conjugate, which lie at the centre. The momentum spectrum, therefore, is unimodal with no interference effect due to reflections from other turning points, for $\omega\tau = 4$ for the Sauter pulse. Similar calculation for the Gaussian pulse gives: $K_{\mathbf{p}}^{(p1)} = 21.8979$, $K_{\mathbf{p}}^{(p2)} = 15.3933$, and $K_{\mathbf{p}}^{(p3)} = 21.8979$ and the value of the exponentials are $e^{-2K_{\mathbf{p}}^{(p1)}} = 9.5448 \times 10^{-20}$, $e^{-2K_{\mathbf{p}}^{(p2)}} = 4.26148 \times 10^{-14}$, $e^{-2K_{\mathbf{p}}^{(p3)}} = 9.5448 \times 10^{-20}$, $e^{-K_{\mathbf{p}}^{(p1)}-K_{\mathbf{p}}^{(p2)}} = 6.37731 \times 10^{-17}$, $e^{-K_{\mathbf{p}}^{(p2)}-K_{\mathbf{p}}^{(p3)}} = 6.37731 \times 10^{-17}$, and $e^{-K_{\mathbf{p}}^{(p1)}-K_{\mathbf{p}}^{(p3)}} = 9.5448 \times 10^{-20}$. In this case the main contribution to the reflection coefficient is from the central turning point. Hence the shape of the momentum spectrum is unimodal. However, the interference between the central and the adjacent turning points also appears with relative strength of about 1.5×10^{-3}. So for the Gaussian pulse case the onset of oscillation takes place for the first time for $\omega\tau = 4$ and the momentum spectrum showing small amplitude oscillations over the unimodal profile.

Now we calculate $f_{\mathbf{p}}(\infty)$ for $\omega\tau = 6$ for the Sauter pulse which shows for the first time the onset of oscillation in the momentum spectrum as seen in the left panel of Fig. 5.5. Here the values of the turning points for $p_3 = 0$ are $t_{p1} = -54.31278 + 12.2396i$, $t_{p2} = 0 + 9.453768i$, $t_{p3} = 54.31278 + 12.2396i$ and their complex conjugates. The values of the integrals are $K_{\mathbf{p}}^{(p1)} = 19.7175$, $K_{\mathbf{p}}^{(p2)} = 15.0493$, and $K_{\mathbf{p}}^{(p3)} = 19.7175$. The value of the exponential are $e^{-2K_{\mathbf{p}}^{(p1)}} = 7.47409 \times 10^{-18}$, $e^{-2K_{\mathbf{p}}^{(p2)}} = 8.47864 \times 10^{-14}$, $e^{-2K_{\mathbf{p}}^{(p3)}} = 7.47409 \times 10^{-18}$, $e^{-K_{\mathbf{p}}^{(p1)}-K_{\mathbf{p}}^{(p2)}} = 7.96105 \times 10^{-16}$, $e^{-K_{\mathbf{p}}^{(p2)}-K_{\mathbf{p}}^{(p3)}} = 7.96105 \times 10^{-16}$, and $e^{-K_{\mathbf{p}}^{(p1)}-K_{\mathbf{p}}^{(p3)}} = 7.47409 \times 10^{-18}$. So the value of the phase integrals for the dominant terms are $\Theta_{\mathbf{p}}^{(p1,p2)} = \int\limits_{Re(t_{p1})}^{Re(t_{p2})} dt\ \omega(\mathbf{p},t) = -81.5475$, $\Theta_{\mathbf{p}}^{(p2,p1)} = \int\limits_{Re(t_{p2})}^{Re(t_{p3})} dt\ \omega(\mathbf{p},t) = 81.5475$ and $\cos\left(2\Theta_{\mathbf{p}}^{(p1,p2)}\right) = \cos\left(2\Theta_{\mathbf{p}}^{(p2,p3)}\right) = 0.9643$. Therefore the interference term $2\cos\left(2\Theta_{\mathbf{p}}^{(p1,p2)}\right)e^{-K_{\mathbf{p}}^{(p1)}-K_{\mathbf{p}}^{(p2)}} + 2\cos\left(2\Theta_{\mathbf{p}}^{(p2,p3)}\right)e^{-K_{\mathbf{p}}^{(p2)}-K_{\mathbf{p}}^{(p3)}} = 3.0708 \times 10^{-15}$ becomes comparable to the term $e^{-2K_{\mathbf{p}}^{(p2)}} = 8.47864 \times 10^{-14}$, representing the reflection from the central turning point. Here the modulation over the unimodal profile appears with the relative strength of 3.6×10^{-2}. The peak value of the distribution $f_{\mathbf{p}=0}(\infty) \approx 8.17154 \times 10^{-14}$.

Appendix E

Derivation of evolution equation for phase and modulus of the order parameter

To study the evolution of order parameter $\Phi(\mathbf{p},t) = 2 < 0_{in}|a^\dagger_{\mathbf{p}}(t)b^\dagger_{-\mathbf{p}}(t)|0_{in} >= |\Phi(\mathbf{p},t)|\exp(i\psi(\mathbf{p},t))$ we solve numerically QKE expressed in the form of 3-coupled ordinary differential equations [32, 63, 81]:

$$\begin{aligned}\frac{df(\mathbf{p},t)}{dt} &= \frac{eE(t)\epsilon_\perp}{2\omega^2(\mathbf{p},t)}u(\mathbf{p},t),\\ \frac{du(\mathbf{p},t)}{dt} &= \frac{eE(t)\epsilon_\perp}{\omega^2(\mathbf{p},t)}[1-2f(\mathbf{p},t)] - 2\omega(\mathbf{p},t)v(\mathbf{p},t),\\ \frac{dv(\mathbf{p},t)}{dt} &= 2\omega(\mathbf{p},t)u(\mathbf{p},t).\end{aligned} \tag{E.1}$$

Here $f(\mathbf{p},t) =< 0_{in}|a^\dagger_{\mathbf{p}}(t)a_{\mathbf{p}}(t)|0_{in} >=< 0_{in}|b^\dagger_{-\mathbf{p}}(t)b_{-\mathbf{p}}(t)|0_{in} >$ is the single particle distribution function, $u(\mathbf{p},t)$ and $v(\mathbf{p},t)$ are the real and imaginary parts of $\Phi(\mathbf{p},t)$. $u(\mathbf{p},t)$ and $v(\mathbf{p},t)$ govern the vacuum polarization and the counter process of pair production i.e., pair annihilation, respectively. The terms $\omega(\mathbf{p},t) = \sqrt{m^2 + p_\perp^2 + P_3^2(t)}$ and $P_3(t) = p_3 - eA(t)$ are the quasi-energy and the longitudinal quasi-momentum respectively of the quasi-particle. The particle acceleration is governed by $dP_3(t)/dt = eE(t)$ in the presence of the time dependent electric field $E(t)$; e is the electronic charge; $\epsilon_\perp = \sqrt{m^2 + \mathbf{p}_\perp^2}$ is the transverse energy of the created particle and $\Theta(\mathbf{p};t_1,t_2) = \int_{t_1}^{t_2} dt'\omega(\mathbf{p},t')$ is the dynamical phases accumulated between initial to final state. It is noted that $f(\mathbf{p},t)$, $u(\mathbf{p},t)$ and $v(\mathbf{p},t)$ satisfy the first integral of motion $(1-2f(\mathbf{p},t))^2+u^2(\mathbf{p},t)+v^2(\mathbf{p},t) = 1$ with initial conditions $f_{in}(\mathbf{p},t_{in}) = u_{in}(\mathbf{p},t_{in}) = v_{in}(\mathbf{p},t_{in}) = 0$ [49]. This first integral of motion can also be expressed in terms of $f(\mathbf{p},t)$ and $|\Phi(\mathbf{p},t)|$ by the relation $(1-2f(\mathbf{p},t))^2 + |\Phi(\mathbf{p},t)|^2 = 1$. Using the Eq. 5.13 we get the evolution equation for the complex order parameter $\Phi(\mathbf{p},t)$ which is given by

$$\frac{d\Phi(\mathbf{p},t)}{dt} = \frac{eE(t)\epsilon_\perp}{\omega^2(\mathbf{p},t)}[1-2f(\mathbf{p},t)] + 2i\omega(\mathbf{p},t)\Phi(\mathbf{p},t). \tag{E.2}$$

Now we decompose the complex order parameter $\Phi(\mathbf{p},t) = |\Phi(\mathbf{p},t)|\exp(i\psi(\mathbf{p},t))$ and use the relation $(1-2f(\mathbf{p},t))^2 + |\Phi(\mathbf{p},t)|^2 = 1$ we get the evolution equations for $|\Phi(\mathbf{p},t)|$ and $\psi(\mathbf{p},t)$ which are given as

$$\begin{aligned} \frac{d|\Phi(\mathbf{p},t)|}{dt} &= \frac{eE(t)\epsilon_\perp}{\omega^2(\mathbf{p},t)}\cos\psi(\mathbf{p},t)\sqrt{1-|\Phi(\mathbf{p},t)|^2}, \\ \frac{d\psi(\mathbf{p},t)}{dt} &= 2\omega(\mathbf{p},t) - \frac{eE(t)\epsilon_\perp}{\omega^2(\mathbf{p},t)}\sin\psi(\mathbf{p},t)\frac{\sqrt{1-|\Phi(\mathbf{p},t)|^2}}{|\Phi(\mathbf{p},t)|}. \end{aligned} \tag{E.3}$$

Bibliography

[1] J. Schwinger, Phys. Rev. **82**, 664 (1951).

[2] P. A. Dirac, in *Proceedings of the Royal Society of London A: Mathematical, Physical and Engineering Sciences* (The Royal Society, 1930), vol. 126, pp. 360–365.

[3] A. Nikishov, Sov. Phys. JETP **30**, 660 (1970).

[4] L. Landau and E. Lifshitz, *The Classical Theory of Fields (Fourth Edition)*, vol. 2 of *Course of Theoretical Physics* (Pergamon, Amsterdam, 1975).

[5] F. Sauter, Z. Phys. **69**, 742 (1931).

[6] W. Heisenberg and H. Euler, Z. Phys. **98**, 714 (1936).

[7] D. Volkov, Z. Phys. **94**, 250 (1935), ISSN 0044-3328, URL http://dx.doi.org/10.1007/BF01331022.

[8] A. Nikishov, Nucl. Phys. B **21**, 346 (1970), ISSN 0550-3213.

[9] E. Brezin and C. Itzykson, Phys. Rev. D **2**, 1191 (1970).

[10] N. Narozhny and M. Fofanov, JETP **90**, 753 (2000).

[11] Laser Phys. **19** (2009), ISSN 1054-660X.

[12] Y. I. Salamin, G. R. Mocken, and C. H. Keitel, Phys. Rev. ST Accel. Beams **5**, 101301 (2002).

[13] I. Gonoskov, A. Aiello, S. Heugel, and G. Leuchs, Phys. Rev. A **86**, 053836 (2012).

[14] A. Gonoskov, I. Gonoskov, C. Harvey, A. Ilderton, A. Kim, M. Marklund, G. Mourou, and A. Sergeev, Phys. Rev. Lett. **111**, 060404 (2013).

[15] S. Bulanov, N. Narozhny, V. Mur, and V. Popov, JETP **102**, 9 (2006).

[16] S. S. Bulanov, V. D. Mur, N. B. Narozhny, J. Nees, and V. S. Popov, Phys. Rev. Lett. **104**, 220404 (2010).

[17] W. Su, M. Jiang, Z. Q. Lv, Y. J. Li, Z. M. Sheng, R. Grobe, and Q. Su, Phys. Rev. A **86**, 013422 (2012).

[18] Q. Su, W. Su, Q. Z. Lv, M. Jiang, X. Lu, Z. M. Sheng, and R. Grobe, Phys. Rev. Lett. **109**, 253202 (2012).

[19] N. Abdukerim, Z.-L. Li, and B.-S. Xie, Phys. Lett. B **726**, 820 (2013), ISSN 0370-2693, URL http://www.sciencedirect.com/science/article/pii/S0370269313007314.

[20] F. Hebenstreit, R. Alkofer, and H. Gies, Phys. Rev. D **82**, 105026 (2010).

[21] C. Kohlfürst, M. Mitter, G. von Winckel, F. Hebenstreit, and R. Alkofer, Phys. Rev. D **88**, 045028 (2013).

[22] M. Ruf, G. R. Mocken, C. Müller, K. Z. Hatsagortsyan, and C. H. Keitel, Phys. Rev. Lett. **102**, 080402 (2009).

[23] E. N. Nerush, I. Y. Kostyukov, A. M. Fedotov, N. B. Narozhny, N. V. Elkina, and H. Ruhl, Phys. Rev. Lett. **106**, 035001 (2011).

[24] A. Di Piazza, E. Lötstedt, A. I. Milstein, and C. H. Keitel, Phys. Rev. Lett. **103**, 170403 (2009), URL https://link.aps.org/doi/10.1103/PhysRevLett.103.170403.

[25] A. Wöllert, H. Bauke, and C. H. Keitel, Phys. Rev. D **91**, 125026 (2015).

[26] A. M. Fedotov, N. B. Narozhny, G. Mourou, and G. Korn, Phys. Rev. Lett. **105**, 080402 (2010).

[27] A. Di Piazza, C. Müller, K. Z. Hatsagortsyan, and C. H. Keitel, Rev. Mod. Phys. **84**, 1177 (2012).

[28] H. Kleinert, R. Ruffini, and S.-S. Xue, Phys. Rev. D **78**, 025011 (2008), URL https://link.aps.org/doi/10.1103/PhysRevD.78.025011.

[29] G. V. Dunne and C. Schubert, Phys. Rev. D **72**, 105004 (2005), URL https://link.aps.org/doi/10.1103/PhysRevD.72.105004.

[30] V. L. Pokrovsky, Physics-Uspekhi **53**, 309 (2010).

[31] C. K. Dumlu, Phys. Rev. D **82**, 045007 (2010), URL http://link.aps.org/doi/10.1103/PhysRevD.82.045007.

[32] S. Schmidt, D. Blaschke, G. Röpke, A. V. Prozorkevich, S. A. Smolyansky, and V. D. Toneev, Phys. Rev. D **59**, 094005 (1999), URL https://link.aps.org/doi/10.1103/PhysRevD.59.094005.

[33] H.-T. Elze and U. Heinz, Phys. Rep. **183**, 81 (1989), ISSN 0370-1573, URL http://www.sciencedirect.com/science/article/pii/0370157389900598.

[34] G. A. Mourou, T. Tajima, and S. V. Bulanov, Rev. Mod. Phys. **78**, 309 (2006), URL https://link.aps.org/doi/10.1103/RevModPhys.78.309.

[35] T. Tajima and G. Mourou, Phys. Rev. ST Accel. Beams **5**, 031301 (2002).

[36] T. Heinzl and A. Ilderton, Eur. Phys. J. D **55**, 359 (2009), ISSN 1434-6079, URL https://doi.org/10.1140/epjd/e2009-00113-x.

[37] G. V. Dunne, Eur. Phys. J. D **55**, 327 (2009), ISSN 1434-6079, URL https://doi.org/10.1140/epjd/e2009-00022-0.

[38] J. Andruszkow, B. Aune, V. Ayvazyan, N. Baboi, R. Bakker, V. Balakin, D. Barni, A. Bazhan, M. Bernard, A. Bosotti, et al., Phys. Rev. Lett. **85**, 3825 (2000), URL https://link.aps.org/doi/10.1103/PhysRevLett.85.3825.

[39] C. Bula, K. T. McDonald, E. J. Prebys, C. Bamber, S. Boege, T. Kotseroglou, A. C. Melissinos, D. D. Meyerhofer, W. Ragg, D. L. Burke, et al., Phys. Rev. Lett. **76**, 3116 (1996).

[40] D. L. Burke, R. C. Field, G. Horton-Smith, J. E. Spencer, D. Walz, S. C. Berridge, W. M. Bugg, K. Shmakov, A. W. Weidemann, C. Bula, et al., Phys. Rev. Lett. **79**, 1626 (1997).

[41] A. Fedotov, Laser Phys. **19**, 214 (2009).

[42] F. Mackenroth, A. Di Piazza, and C. H. Keitel, Phys. Rev. Lett. **105**, 063903 (2010), URL http://link.aps.org/doi/10.1103/PhysRevLett.105.063903.

[43] T. Brabec and F. Krausz, Rev. Mod. Phys. **72**, 545 (2000), URL http://link.aps.org/doi/10.1103/RevModPhys.72.545.

[44] F. Krausz and M. Ivanov, Rev. Mod. Phys. **81**, 163 (2009), URL http://link.aps.org/doi/10.1103/RevModPhys.81.163.

[45] S. P. Kim and D. N. Page, Phys. Rev. D **65**, 105002 (2002), URL https://link.aps.org/doi/10.1103/PhysRevD.65.105002.

[46] S. P. Kim and H. K. Lee, Phys. Rev. D **76**, 125002 (2007), URL https://link.aps.org/doi/10.1103/PhysRevD.76.125002.

[47] S. P. Kim, H. K. Lee, and Y. Yoon, Phys. Rev. D **78**, 105013 (2008), URL https://link.aps.org/doi/10.1103/PhysRevD.78.105013.

[48] W.-Y. P. Hwang and S. P. Kim, Phys. Rev. D **80**, 065004 (2009), URL https://link.aps.org/doi/10.1103/PhysRevD.80.065004.

[49] D. B. Blaschke, A. V. Prozorkevich, G. Röpke, C. D. Roberts, S. M. Schmidt, D. S. Shkirmanov, and S. A. Smolyansky, Eur. Phys. J. D **55**, 341 (2009), ISSN 1434-6060.

[50] F. Hebenstreit and F. Fillion-Gourdeau, Phys. Lett. B **739**, 189 (2014), ISSN 0370-2693.

[51] S. P. Kim and D. N. Page, Phys. Rev. D **73**, 065020 (2006), URL https://link.aps.org/doi/10.1103/PhysRevD.73.065020.

[52] C. K. Dumlu and G. V. Dunne, Phys. Rev. Lett. **104**, 250402 (2010), URL https://link.aps.org/doi/10.1103/PhysRevLett.104.250402.

[53] B. S. Xie, Z. L. Li, and S. Tang, Matter and Radiation at Extremes **2**, 225 (2017), ISSN 2468-080X, URL http://www.sciencedirect.com/science/article/pii/S2468080X17300183.

[54] A. Benedetti, R. Ruffini, and G. Vereshchagin, Phys. Lett. A **377**, 206 (2013), ISSN 0375-9601, URL http://www.sciencedirect.com/science/article/pii/S0375960112011814.

[55] A. V. Filatov, A. V. Prozorkevich, S. A. Smolyansky, and V. D. Toneev, Phys. Part. Nucl. **39**, 886 (2008), ISSN 1531-8559, URL https://doi.org/10.1134/S1063779608060026.

[56] Y. Kluger, J. M. Eisenberg, B. Svetitsky, F. Cooper, and E. Mottola, Phys. Rev. Lett. **67**, 2427 (1991), URL https://link.aps.org/doi/10.1103/PhysRevLett.67.2427.

[57] J. Rau, Phys. Rev. D **50**, 6911 (1994), URL https://link.aps.org/doi/10.1103/PhysRevD.50.6911.

[58] S. A. Smolyansky, A. D. Panferov, A. V. Prozorkevich, and M. Bonitz, P-Adic Numbers, Ultrametric Analysis, and Applications **4**, 319 (2012), ISSN 2070-0474, URL https://doi.org/10.1134/S207004661204005X.

[59] S. A. Smolyansky, A. D. Panferov, D. B. Blaschke, L. Juchnowski, B. Kämpfer, and A. Otto, Russ. Phys. J. **59**, 1731 (2017), ISSN 1573-9228, URL https://doi.org/10.1007/s11182-017-0970-5.

[60] D. B. Blaschke, B. Kämpfer, A. D. Panferov, A. V. Prozorkevich, and S. A. Smolyansky, Contrib. Plasma Phys. **53**, 165 (2013), https://onlinelibrary.wiley.com/doi/pdf/10.1002/ctpp.201310029, URL https://onlinelibrary.wiley.com/doi/abs/10.1002/ctpp.201310029.

[61] C. K. Dumlu and G. V. Dunne, Phys. Rev. D **83**, 065028 (2011), URL https://link.aps.org/doi/10.1103/PhysRevD.83.065028.

[62] F. Hebenstreit, Phys. Lett. B **753**, 336 (2016), ISSN 0370-2693, URL http://www.sciencedirect.com/science/article/pii/S0370269315009971.

[63] Y. Kluger, E. Mottola, and J. M. Eisenberg, Phys. Rev. D **58**, 125015 (1998), URL https://link.aps.org/doi/10.1103/PhysRevD.58.125015.

[64] N. Narozhny, Laser Phys. **15**, 1458 (2005).

[65] C. Banerjee and M. P. Singh, JETP **125**, 12 (2017), ISSN 1090-6509, URL https://doi.org/10.1134/S1063776117060097.

[66] C. Banerjee and M. P. Singh, Eur. Phys. J. D **72**, 4 (2018), URL https://doi.org/10.1140/epjd/e2017-80399-7.

[67] C. Banerjee, M. P. Singh, and A. M. Fedotov (2018), arXiv:1806.07088.

[68] V. Berestetskii, L. Pitaevskii, and E. Lifshitz, *Quantum Electrodynamics*, Vol. 4 (Elsevier Science, 2012).

[69] D. J. Griffiths, *Introduction to Electrodynamics, 3rd ed.* (Prentice Hall, 1999).

[70] F. Hebenstreit, R. Alkofer, G. V. Dunne, and H. Gies, Phys. Rev. Lett. **102**, 150404 (2009), URL http://link.aps.org/doi/10.1103/PhysRevLett.102.150404.

[71] V. F. Bashmakov, E. N. Nerush, I. Y. Kostyukov, A. M. Fedotov, and N. B. Narozhny, Phys. Plasmas **21**, 013105 (2014).

[72] S. S. Bulanov, V. D. Mur, N. B. Narozhny, J. Nees, and V. S. Popov, Phys. Rev. Lett. **104**, 220404 (2010), URL http://link.aps.org/doi/10.1103/PhysRevLett.104.220404.

[73] S. S. Bulanov, A. M. Fedotov, and F. Pegoraro, Phys. Rev. E **71**, 016404 (2005).

[74] S. S. Bulanov, Phys. Rev. E **69**, 036408 (2004).

[75] G. R. Mocken, M. Ruf, C. Müller, and C. H. Keitel, Phys. Rev. A **81**, 022122 (2010), URL https://link.aps.org/doi/10.1103/PhysRevA.81.022122.

[76] E. Akkermans and G. V. Dunne, Phys. Rev. Lett. **108**, 030401 (2012), URL https://link.aps.org/doi/10.1103/PhysRevLett.108.030401.

[77] F. Hebenstreit, R. Alkofer, G. V. Dunne, and H. Gies, Phys. Rev. Lett. **102**, 150404 (2009), URL https://link.aps.org/doi/10.1103/PhysRevLett.102.150404.

[78] S. M. Schmidt, D. Blaschke, G. Röpke, S. A. Smolyansky, A. V. Prozorkevich, and V. D. Toneev, Int. J. Mod. Phys. E **07**, 709 (1998).

[79] A. Huet, S. P. Kim, and C. Schubert, Phys. Rev. D **90**, 125033 (2014), URL https://link.aps.org/doi/10.1103/PhysRevD.90.125033.

[80] S. Coleman, J. Math. Phys. **7**, 787 (1966).

[81] A. M. Fedotov, E. G. Gelfer, K. Y. Korolev, and S. A. Smolyansky, Phys. Rev. D **83**, 025011 (2011), URL https://link.aps.org/doi/10.1103/PhysRevD.83.025011.

[82] A. Białas and W. Czyż, Phys. Rev. D **30**, 2371 (1984), URL https://link.aps.org/doi/10.1103/PhysRevD.30.2371.

[83] Y. Kluger, J. M. Eisenberg, B. Svetitsky, F. Cooper, and E. Mottola, Phys. Rev. D **45**, 4659 (1992), URL https://link.aps.org/doi/10.1103/PhysRevD.45.4659.

[84] N. V. Elkina, A. M. Fedotov, I. Y. Kostyukov, M. V. Legkov, N. B. Narozhny, E. N. Nerush, and H. Ruhl, Phys. Rev. ST Accel. Beams **14**, 054401 (2011), URL https://link.aps.org/doi/10.1103/PhysRevSTAB.14.054401.